Molecular Dynamics Simulations of Charged Nanodroplets

(Spine title: Molecular Dynamics Simulations of
Charged Nanodroplets)

(Thesis format: Integrated-Article)

by

Elias Ahadi

Graduate Program in Chemistry

A thesis submitted in partial fulfillment
of the requirements for the degree of
Doctor of Philosophy

The School of Graduate and Postdoctoral Studies
The University of Western Ontario
London, Ontario, Canada

THE UNIVERSITY OF WESTERN ONTARIO
SCHOOL OF GRADUATE AND POSTDOCTORAL STUDIES

CERTIFICATE OF EXAMINATION

Supervisor	Examiners
Dr. Lars Konermann	Dr. Yang Song
	Dr. Ken Yeung
	Dr. Colin Denniston
	Dr. Igor A. Kaltashov

The thesis by

Elias Ahadi

entitled:

Molecular Dynamics Simulations of Charged Nanodroplets

is accepted in partial fulfillment of the
requirements for the degree of
Doctor of Philosophy

Date____________________________

____
Chair of the Thesis Examination Board

Abstract

Charged nanodroplets represent a fascinating research area due to their unique dynamics and physical properties. These nanodroplets play a key role in electrospray mass spectrometry (ESI-MS), which is a method for analyzing organic/inorganic molecules as well as proteins and other biomolecular species. The mechanism whereby these analytes are transferred into the gas phase as intact ions remains incompletely understood. Two competing models have been proposed to explain the process, the charged residue model (CRM) and the ion evaporation model (IEM). Under the CRM, evaporation of the droplet proceeds until dryness, at which point the analyte ion is left behind. Under the IEM model, analyte ions are released from the droplet surface by overcoming an activation energy barrier.

In this work, molecular dynamics (MD) simulations were used with the goal of characterizing the nanodroplet behavior in more detail, and for gaining insights in the mechanism of gas phase ion formation during ESI. Three atom site models were used to represent water as well as methanol. The droplets contained 1000 – 1500 solvent molecules, providing radii of ~ 18 – 23 Å. Excess charge was accounted for by including protons, sodium and ammonium ions. A number of investigations were conducted by including a coarse-grained model protein in the droplet. Different protein conformations (unfolded and folded) were investigated with hydrophobic or hydrophilic side chain patterns.

As part of the findings of this work, it was discovered that ion location and charge location within the droplets do not coincide. Instead, water dipole orientation projects the charge from the interior to the droplet surface. The observed behavior helps resolve an apparent conundrum in the existing ESI literature. Small ions were shown to undergo ejection events that are consistent with an IEM type scenario. Unfolded hydrophobic protein chains also display a behavior reminiscent of the IEM, while folded and hydrophilic unfolded versions show CRM characteristics. Overall the results of this thesis contribute to a better understanding of the nanodroplet behavior by shedding light on the final stages of the ESI process.

Keywords: mass spectrometry, electrospray ionization, molecular dynamics, charged residue model, ion evaporation model, water, methanol, protein

Statement of Co-Authorship

The work in Chapters 2, 3 and 4 was published in the following articles, respectively;

> Elias Ahadi and Lars Konermann (2009). A ‘Hopping’ Proton Model for Molecular Dynamics Simulations of Charged Water Nanodroplet, J. Phys. Chem. B, 113, 7071-7080. Reprinted with permission. © 2009 American Chemical Society
>
> Elias Ahadi and Lars Konermann (2010). Surface Charge of Electrosprayed Water Nanodroplets: A Molecular Dynamics Study, J. Am. Chem. Soc., 132, 11270-11277. Reprinted with permission. © 2010 American Chemical Society
>
> Elias Ahadi and Lars Konermann (2011). Ejection of Solvated Ions from Electrosprayed Methanol/Water Nanodroplets Studied by Molecular Dynamics Simulations, J. Am. Chem. Soc., 133, 9354-9363. Reprinted with permission. © 2011 American Chemical Society

The work in Chapter 5 is being prepared for future publication.

> Elias Ahadi and Lars Konermann, Towards a Mechanistic Understanding of Macromolecular Electrospray Ionization: A Molecular Dynamics Simulation Study

The original draft for each of the above articles was prepared by the author (E.A.). Subsequent revisions were made by the author and Dr. Lars Konermann. All computer code (main molecular dynamics program and other small programs used to analyze data) were written in C++ by the author. Subsequently, plots from the analyzed data were generated by the author as well.

Acknowledgments

I would like to thank Dr. Lars Konermann immensely for his guidance, encouragement and generosity throughout the years of my study in his lab. I would also like to thank past and present fellow students and researchers for their support, Dr. Kengo Ichiki, Dr. Maxim Paliy, Dr. Jingxi Pan, Dr. Yuhong Liu, Dr. Peter Ferguson, Brian Boys, Bradley Stocks, Mahasilu Amunugama, Jenna Liu, Lucy Pan, Siavash Vahidi, Kirkland Mainer, Tomasz Czarny and Stephen Sciuto.

I would like to thank the people who maintain the SHARCNET (www.sharcnet.ca) facility. Without the computing resources and technical support, none of this work would have been possible in a reasonable time frame. I would also like to thank Dr. S. R. Valluri for sponsoring the SHARCNET account.

Finally, I would like to thank my family members my wife and son, parents, sisters and nieces for their love, support and patience throughout the years.

Table of Contents

List of Tables

Chapter 1

Chapter 5

List of Figures

Chapter 1

Chapter 2

Chapter 3

Chapter 4

Chapter 5

List of Symbols and Abbreviations

COM – Center of Mass

CRM – Charge Residue Model

CG – Coarse-Grain

D – Diffusion Coefficient

DFT – Density Functional Theory

ε_0 – Permittivity of Vacuum

ε – Minimum Energy Depth in LJ Potential Function

e – Elementary Charge

$\vec{E}$ – Electric Field

EE – Electronegativity Equalization

$E_{\text{potential}}$ – Potential Energy

E_{kinetic} – Kinetic Energy

EI – Electron Ionization

ESI – Electrospray Ionization

$\vec{F}$ – Force Vector

FDM – Finite Difference Method

FWHM – Full Width at Half Maximum

g – Total Number of Degrees of Freedom

ΔG – Free Energy

ΔG^* – Activation Energy

h – Planck’s Constant

HB – Hydrogen Bonding

HF – Hartree-Fock

IEM – Ion Evaporation Model

IR – Infrared

K – Kinetic Energy

k – Rate Constant

k_B – Boltzmann Constant

k_s – Spring Constant

l – Length

$\vec{L}(t)$ – Angular Momentum

LJ – Lennard-Jones

m – Mass

MALDI – Matrix-Assisted Laser Desorption/Ionization

MC – Monte Carlo

MD – Molecular Dynamics

MM – Molecular Mechanics

MS – Mass Spectrometry

MSD – Mean Square Displacement

m/z – Mass-to-Charge Ratio

N – Number of Atoms

N_c – Number of Constraints

$\vec{p}$ – Momentum Vector

Q_N – Nose Factor

P(r) – Radial Distribution

q – Charge

r_0 – Equilibrium Bond Distance

$\vec{r}$ – Position Vector

$\vec{r}(t + \Delta t)$ – New Position of Particle

$\vec{r}(t - \Delta t)$ – Previous Position of Particle

$\vec{r}(t)$ – Current Position of Particle

R – Droplet Radius

RDF – Radial Distribution Function

σ – Intermolecular Distance between 2 Particles at which LJ Potential is equal to Zero

S – Surface Energy

SHARCNET – Shared Hierarchical Computer Network

SHG – Second Harmonic Generation

SPC – Single Point Charge Water Model

SPC/E – Single Point Charge Extended Water Model

SPC/F – Single Point Charge Flexible Water Model

SPCP – Single Point Charge Polarizable Water Model

SE – Semi-empirical

t – Time

Δt – Difference in Time

T – Temperature

T_{Set} – Set Temperature

ξ – Thermodynamic Friction Coefficient

TOF – Time-of-Flight

ΔU – Change in Potential Energy

$\vec{\mu}$ – Dipole Moment Vector

$\vec{v}$ – Velocity Vector

VMD – Visual Molecular Dynamics Software

VSFS – Vibrational Sum-Frequency Spectroscopy

γ – Surface Tension

z_R – Number of Elementary Charges for the Rayleigh Equation

Chapter 1 – Introduction

1.1 Charged Droplets

Charged droplets are ubiquitous and can be found in numerous environmental and technological applications. Examples of such applications could include; ink-jet printing, pesticide spraying on crops, and cloud seeding. We will briefly mention two of these applications in more detail and observe the role of charged droplets in the specific technology. Zhao and co-workers [1] used a numerical simulation approach to study the trajectories of charged pesticide droplets towards a plant target by varying such parameters as charge-to mass ratios, nozzle-to-target distances and droplet size. By varying such parameters, it was found that smaller charged droplets increase the deposition rate, thereby reducing pesticide loss due to off target trajectories. This agricultural application will have a positive environmental impact in the long run. In another example, Khain and co-workers [2] aimed to increase rain in arid regions and to reduce fog for roads and runways. The method used to achieve this goal is to inject charged droplets into clouds which in turn increases the collision efficiency of charge-neutral and charge-charge droplets over gravity-induced collisions. This process increases the rate of raindrop formation by a seeding mechanism and at the same time reduces the concentration of small droplets which are responsible for fog formation.

Dole and co-workers [3] observed related phenomena in spray painting of cars. Ultimately, this research area gave rise to the development of electrospray ionization (ESI) [4-6] which today plays a key role in the biological mass spectrometry (MS). Currently this field provides a wealth of information regarding the physical behavior of charged droplets. In ESI-MS, as the size of the charged droplets decrease into the nanometer regime, charge and surface tension effects dominate the droplet behavior, while gravitational effects become less important.

1.2 Mass Spectrometry

MS is a versatile analytical tool found in many laboratories where it is used for measuring the mass-to-charge ratio (*m/z*) of ions in the gas phase. Based on these measurements, structural information can be deduced for large biological and organic molecules, either as intact species or as fragments. A block diagram of a typical mass spectrometer is shown in Figure 1.1. It consists of the following components: a vacuum chamber, vacuum pumps, an ion source, a mass analyzer and a detector. The ion source produces gas phase ions from analyte molecules. These ions then pass through the vacuum chamber. The pressure inside this vacuum is typically on the order of 10^{-6} – 10^{-9} Torr, and it is maintained by vacuum pumps. This low pressure is necessary to prevent the ions from extensively colliding with background gas that would otherwise be present under normal atmospheric conditions and therefore result in a small mean free path (~ 1 μm). In the vacuum environment, the mean free path is much longer (~ 1 m), allowing the ions to reach the detector where their relative abundance is quantified [7, 8].

The heart of each mass spectrometer is the mass analyzer which separates the ions based on their *m/z*. In general, the mass analyzer can consist of electric and magnetic fields that guide the ions, while at the same time sorting them by their *m/z* ratios. The mass analyzer can be described as operating in either pulsed or continuous mode. Continuous mode analyzers, such as quadrupoles and magnetic sectors, allow the transmission of a single *m/z* to the detector, whereby a mass spectrum is obtained by scanning the analyzer so a wide *m/z* ratio range can be monitored. While this technique is quite selective, it is also inefficient in that any *m/z* ion not captured by the specific

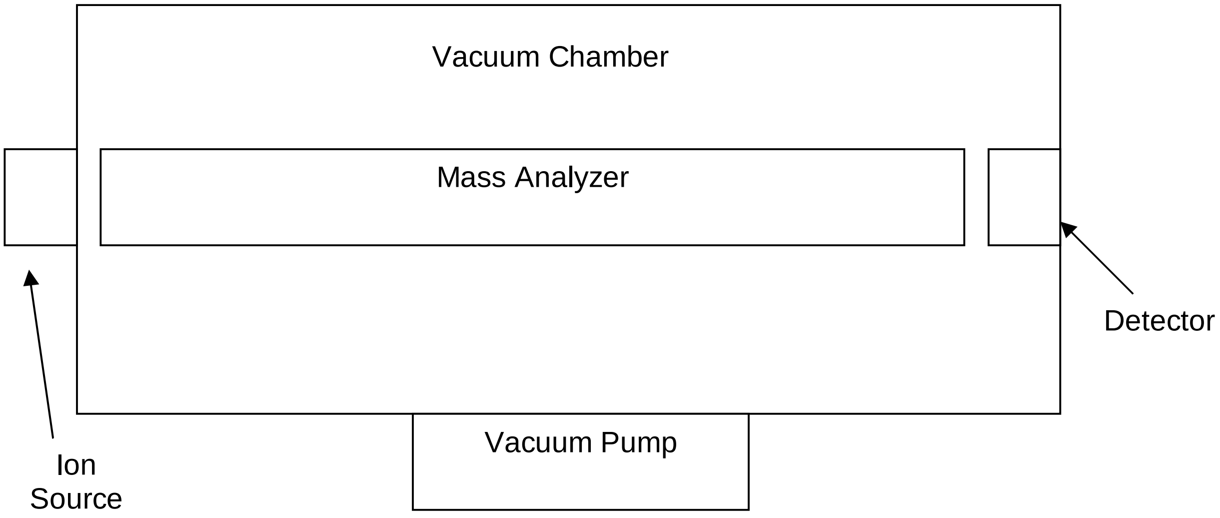

Figure 1.1 Basic components of a mass spectrometer.

choice of parameters is lost in the process. On the other hand, pulsed mode analyzers, such as time-of-flight (TOF) instruments, scan an entire mass spectrum from a single pulse of ions.

In the TOF analyzer, a voltage pulse gives all the ions of equal charge an equal potential energy which is then transferred to kinetic energy according to

$$E_{Potential} = E_{Kinetic} \tag{1.1}$$

which can be written as

$$\Delta Uez = \frac{1}{2}mv^2 \tag{1.2}$$

where ΔU is the potential energy, e is the elementary charge, z is the number of charges, m is the mass of the ion and v is the velocity of the ion. Equation (1.2) can be rearranged so that the velocity is

$$v = \sqrt{\frac{2ze\Delta U}{m}} \tag{1.3}$$

Ions with different m/z have different velocities and since the distance from the ion source to the detector is l, the time t it takes to reach the detector is

$$t = \frac{l}{v} = \frac{l}{\sqrt{\frac{2ze\Delta U}{m}}} = \frac{l}{\sqrt{2\Delta Ue}}\sqrt{\frac{m}{z}} \tag{1.4}$$

where ions with larger *m/z* are detected at a later time than the smaller *m/z*. Hence, the ions are sorted according to their *m/z* values and a spectrum can be generated.

Ionization of the analyte in MS occurs at the ion source (Figure 1.1), often (but not always) under atmospheric conditions. Protonation, deprotonation, electron ejection, and addition of small ions such as Na^+ or NH_4^+ are possible methods that can be used. The most common method used in the early decades of the invention of MS was electron ionization (EI). Under EI conditions the sample is converted into the gas phase via heating and then bombarded with electrons from a heated filament. The fast moving electrons induce the ejection of an electron from the analyte molecule, thereby turning the analyte into a radical cation. Due to the high energy of the electrons from the source subsequent electrons from the analyte can produce extensive fragmentation which is not suitable for large biomolecules. However, even though fragmentation can complicate a typical spectrum, at the same time it can also provide useful information for identifying unknown molecules. For large biomolecular analytes, ESI and matrix-assisted laser desorption/ionization (MALDI) are better choices, since the ionization does not produce extensive fragmentation such that fully intact macromolecules can be ionized [4, 9-11].

Proteins can become ionized by either being deprotonated at acidic sites ($-COOH \rightarrow -COO^- + H^+$) or protonated at basic sites (e.g. $-NH_2 + H^+ \rightarrow NH_3^+$) [12]. The composition of the ions resulting from deprotonation and protonation can be denoted as $[M - nH]^{n-}$ or $[M + nH]^{n+}$, respectively, where M is the mass of the neutral protein.

1.3 Electrospray Ionization

ESI has become a standard ionization method for analyzing proteins and other biological macromolecules, but also for low molecular weight species. In a typical ESI process, the first step is to spray a solution composed of an analyte, a solvent and ions such as Na^+, NH_4^+, H^+ through a metal capillary tube where a high electric voltage of ~ 2-3 kV is applied as shown in Figure 1.2. The electric field leads to electrophoretic charge separation in the solution at the tip of the capillary tube. The liquid emanating from the tip of the Taylor cone eventually emits micrometer-sized positively charged droplets. A period of solvent evaporation ensues and the charge density increases on the ever shrinking droplet surface. Eventually, the cohesive surface tension forces and the Coulombic repulsive forces reach a critical point. At this so called Rayleigh limit [13], the number of charges, z_R, can be determined according to

$$z_R e = 8\pi\sqrt{\varepsilon_0 \gamma R^3} \tag{1.5}$$

where e is the elementary charge, ε_0 is the permittivity of the vacuum, γ is the surface tension of the solvent and R is the radius of the droplet. At Rayleigh limit, the droplet becomes unstable, eventually leading to a Coulombic fission event where several much smaller daughter droplets and a residual parent droplet are formed (Figure 1.3). After the Coulombic fission, the charge on the residual parent droplet falls below the Rayleigh limit and the droplet becomes stable once more [14]. Through another period of evaporation the charge density on the droplet reaches the Rayleigh limit which again

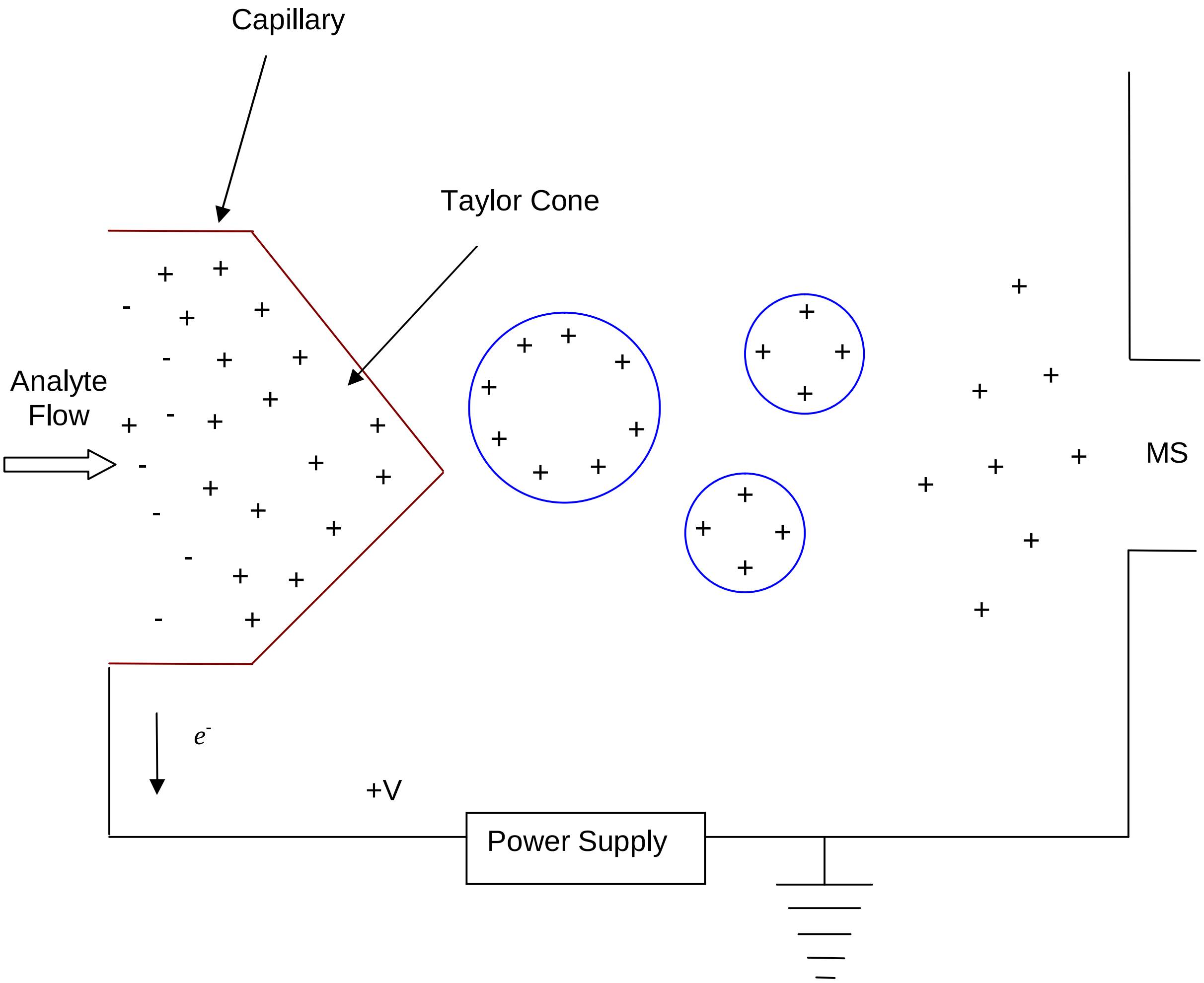

Figure 1.2. Schematic diagram of the ESI process.

results in another Coulombic fission event, releasing more daughter droplets, carrying with them more charge. Throughout this process analyte ions are released from small daughter droplets [15-17]. This evaporation/fission scenario can repeat itself over several generations (Figure 1.3).

A study by Storozhev and co-workers [18], used a mathematical model to examine the Coulombic fission process of a charged liquid droplet in an external electrostatic field. The authors concluded that the potential barrier for the fission process decreases in height with a decrease in the radius of droplet. For nanometer sized droplets, daughter droplets possess 5% of the mass and 15% of the initial charge of the parent droplet. The theoretical model is consistent with observations from Gomez and others [14, 16, 19, 20] which showed that ~ 20 daughter droplets carried off 2% of the mass and 15% of the charge.

Notably, Rayleigh's framework represents a macroscopic theory. It holds for droplets in the micrometer range, but it might not necessarily apply in the nanometer range. As the size of the droplets becomes smaller, certain molecular variables become more significant in droplet disintegration. Such variables can include ion location within the droplet and ion-solvent interactions [14, 21, 22].

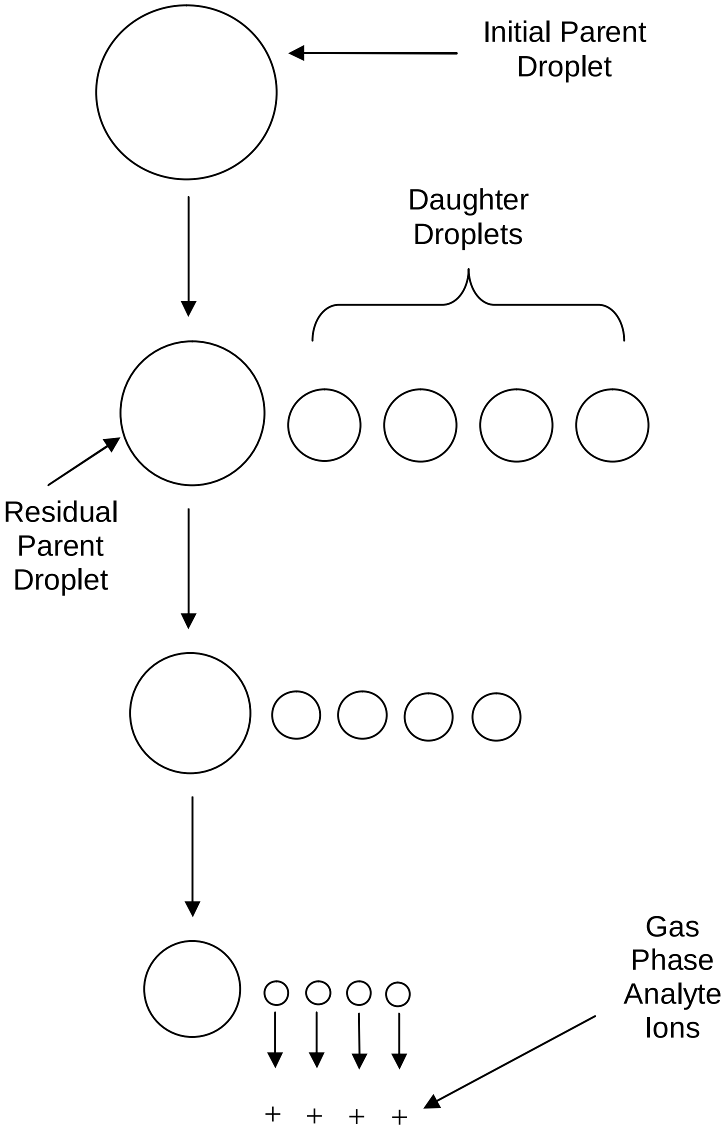

Figure 1.3. Schematic diagram depicting droplet evaporation and fission over time.

1.4 Ionization Mechanisms: CRM and IEM

Much information about the droplet disintegration mechanism comes from ESI-MS studies. Based on theoretical and experimental investigations, two competing models have been proposed. The two frameworks are referred to as the ion evaporation model (IEM) [23, 24] and charge residue model (CRM) [3, 25]. Figure 1.4 shows a simplified diagram of the IEM and CRM process. The initial droplet in Figure 1.4 essentially represents one of the daughter droplets in the last “generation” of Figure 1.3. The initial solvent evaporation and Coulombic fission events (discussed above, Figure 1.3) are the same for the IEM and CRM. Eventually, however, the two mechanisms diverge into distinct pathways. In the IEM branch, an analyte ion (red) is released from the droplet surface by overcoming an activation energy barrier leaving behind a charged droplet. In the CRM branch, the evaporation of the droplet continues until dryness, thereby releasing the analyte ion into the gas phase with some of the droplet charge.

The most significant evidence [26] that multiply charged native proteins are produced by the CRM process has been provided by de la Mora [25]. For natively folded proteins, the observations of protonation states are close in value with the z_R (equation 1.5) for protein sized water droplets. From the works of de la Mora and others [27-31] the CRM model has been accepted for native proteins by most researchers. However, diverging opinions still exist [32]. Also, the question of how unfolded proteins become ionized and by what charging mechanism remains unanswered.

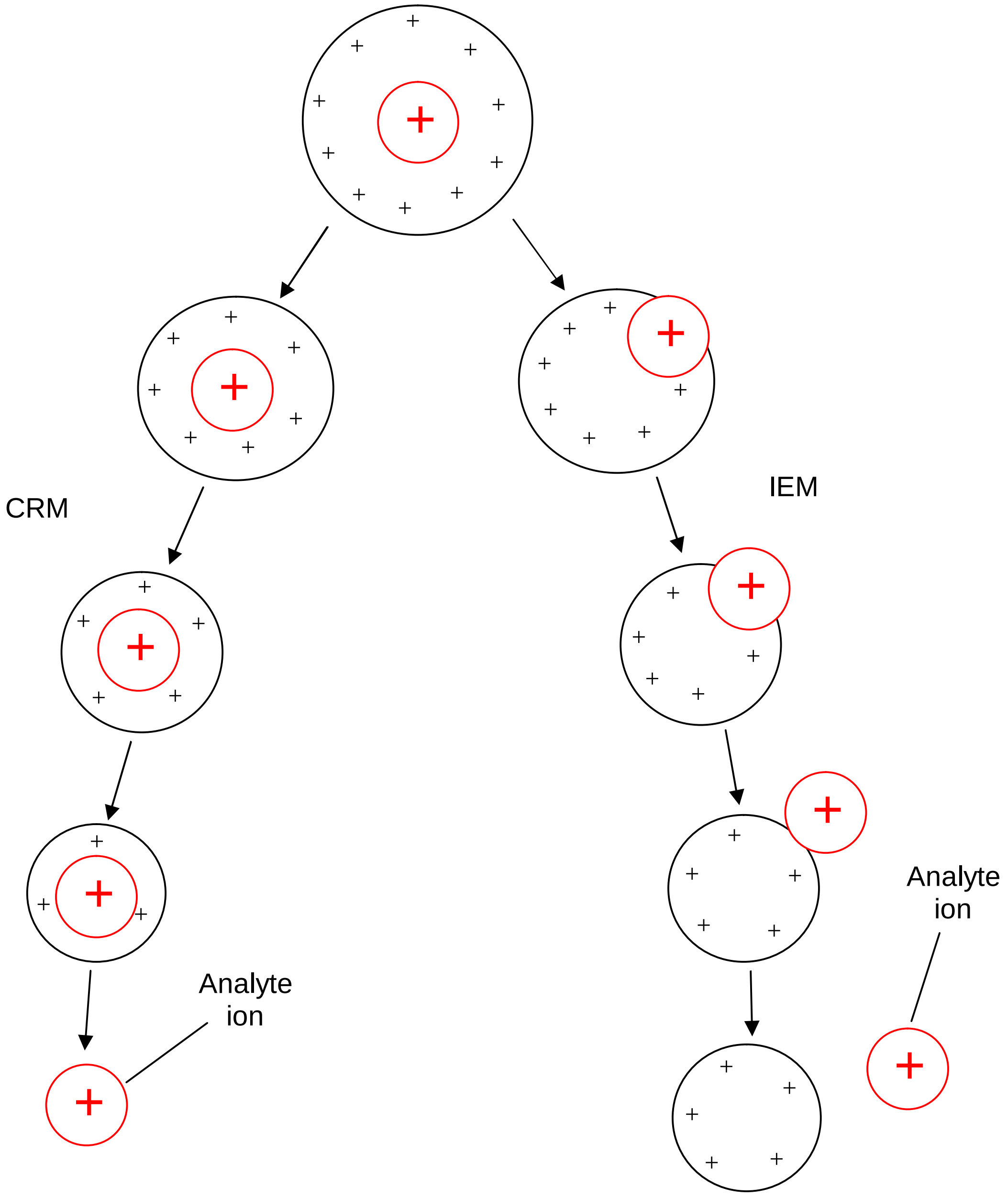

Figure 1.4. Schematic diagram of the CRM and IEM models.

According to the IEM [23, 24] model, through successive Coulombic fission events and evaporation, an ion emission can occur [15]. Small analytes [15, 33, 34] (especially preformed ions such as NH_4^+, CH_3COO^-) are thought to go through this process when the electric field at the surface approaches the Rayleigh limit. In order to reduce the instability of the droplet, solvated analytes and/or electrolyte ions are ejected. The model describes the detachment of a solvated analyte ion from the parent droplet as an activated process. A schematic free energy profile that corresponds to this process is shown in Figure 1.5. The free energy minimum of the profile corresponds to an initial configuration where the analyte ion (red) resides within the droplet. The maximum is identified as the transition state (TS), corresponding to a disconnected state between the parent droplet and the detached solvated analyte ion. A transition state energy barrier is overcome when the ion is approximately a distant *x* from the surface of the droplet as shown in Figure 1.5. The free energy barrier, arises from two competing electrostatic factors, the attractive force can be interpreted arising from an image charge effect [35] of the detached analyte ion. The repulsive force arises between the detached analyte ion and like charges on the droplet surface. One of the assumptions of the IEM model is that the transition state resembles the final detached state more than the initial configuration. This form of the transition state is called a 'late' transition state [23]. The assumption of a late transition state facilitates the estimate of the free energy barrier by using closed electrostatic expressions. The estimate of the free energy barrier is based on Born's model that provides the free energy to move a solvated ion from a bulk neutral solvent to a distance of infinity. This estimate is an approximate, and later improvements were added

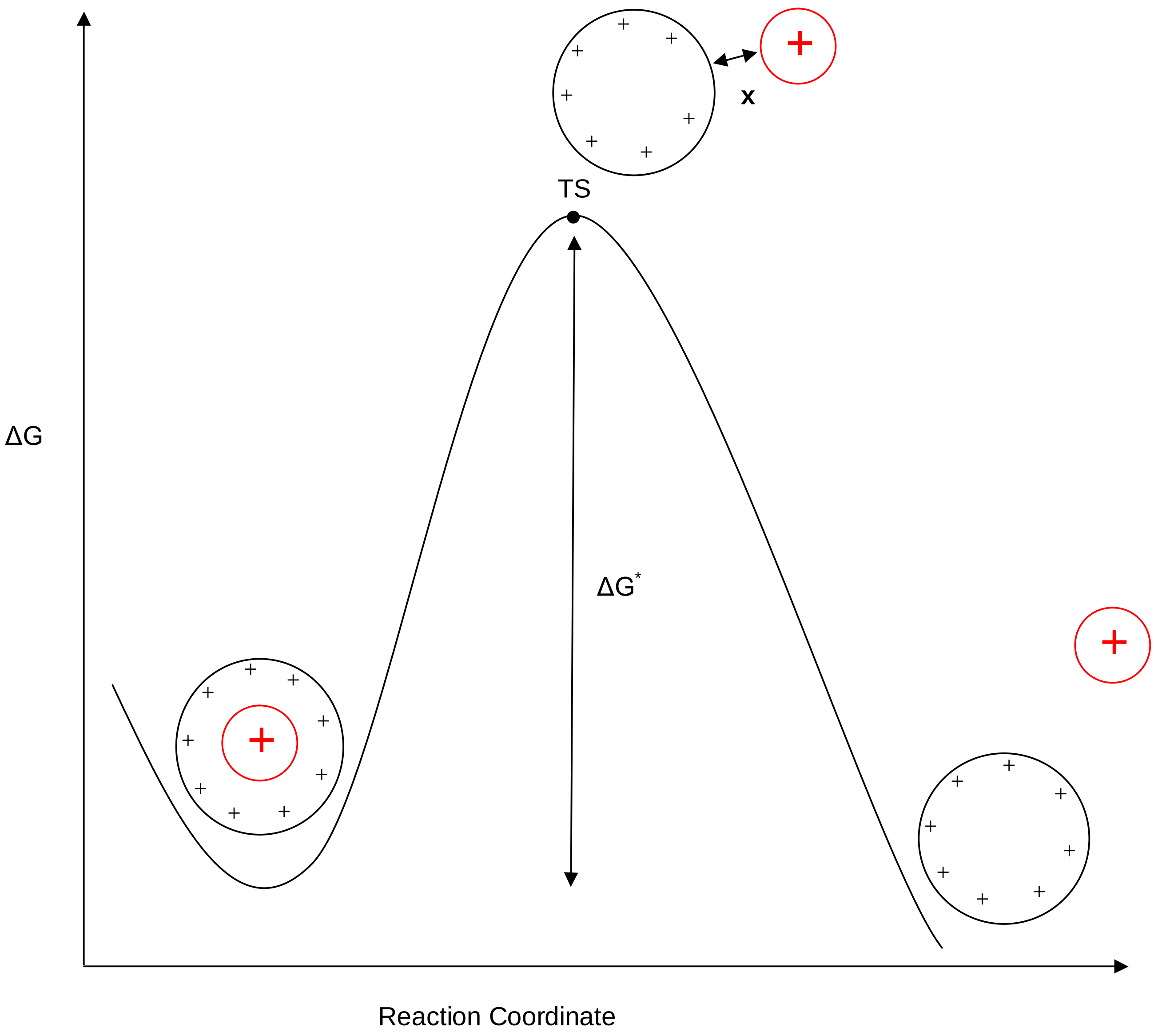

Figure 1.5. Schematic diagram of the IEM mechanism. TS, transition state; ΔG*, activation energy barrier.

that included curvature effects [34, 36] of the droplet surface, surface tension, as well as solvent polarization [37, 38].

Estimates of the activation free energy (ΔG^*) allows determining the rate constant of charge detachment by the transition state theory expression [23, 33, 39]

$$k = \frac{k_B T}{h} \exp\left(\frac{-\Delta G^*}{k_B T} \right) \tag{1.6}$$

where k_B is the Boltzmann constant, h is Planck's constant, and T is the temperature.

The IEM model does not provide justification that the 'late' transition state energy barrier is the rate determining barrier. An 'earlier' energy barrier may be responsible for the transition step while the solvated analyte ion breaks the surface of the droplet. This ambiguity is one of the weaknesses of the IEM model [17]. Another assumption made by the IEM model is that the lowering of the energy barrier for ion evaporation to occur is a result of the electric field penetration into the surface of the charged droplet and thereby neglecting the strong screening of the electric field by the polarized solvent molecules. Hence, it maybe unlikely that the electric field strength for the ion evaporation becomes smaller than the critical field strength for the disintegration of charged droplets given by the Rayleigh limit. Overall, the preceding discussion highlights the fact that the mechanism(s) of the ESI process are far from being understood.

1.5 Molecular Simulations

With the invention of microcomputers in the 1970s [40], molecular simulations have become highly relevant as an alternative method of verifying experimental calculations and theoretical predictions. This is in part since computers became affordable thereby giving scientists easier access to such resources with ever increasing faster processors.

1.5.1 Ab inito Methods

Ab initio methods are derived from first principles with no input from experimental data. This method still does not generate exact solutions to the quantum mechanical equations but instead predicts approximate answers. Hartree-Fock (HF) is the most common *ab initio* method used and it uses molecular orbital theory. This method is highly computational intensive since it involves the calculation of electronic ground states for each atom [41, 42].

1.5.2 Density Functional Theory

Density functional theory (DFT) is also considered an *ab initio* method that calculates the molecular electronic structure. It uses functionals where the electron density is a function of the wavefunction. [41-44].

1.5.3 Semi-empirical Methods

Semi-empirical (SE) methods are based on HF methods but employ approximations that are derived from experimental results. This approach can calculate electronic states as well. It is less computational demanding than *ab initio* methods [41, 42].

1.5.4 Molecular Mechanics

Molecular mechanics (MM) methods can be used to model larger systems by avoiding quantum mechanical calculations all together. MM uses Newtonian mechanics to model the systems with the use of force fields which includes a set of parameters and functions which are derived from experimental data or *ab initio* calculations. In MM, potentials have been developed to account for covalent and non-covalent interactions. Harmonic potentials are used to model covalent interactions such as bond bending, stretching and rotation. Non-covalent interactions which include electrostatic and van der Waals, can be modeled through a Coulomb potential and a Lennard-Jones (LJ) potential, respectively. This method can be used to model molecules as large as large proteins and nucleic acids. MM is mainly used as an energy minimization tool for then large biomolecules. The bond distances and angles are moved slightly and the potential energy is calculated iteratively until a local or global minimum potential is reached [41, 42].

1.5.5 Molecular Dynamics Simulations

Molecular dynamics (MD) methods use Newtonian mechanics to examine the time-dependent motion of atoms and molecules. This approach uses similar potential functions that account for covalent and non-covalent interactions as MM. However, additional algorithms are used to integrate Newton's equation of motion, and to move each particle from one point to another in space and time. The advantage of MD is that since it is time based it can provide dynamic transport properties of the system under investigation. MD can be used as a tool for energy minimization much like MM, however, large sampling of configurations over time is required [41, 42, 44-47].

1.5.6 Monte Carlo Simulations

Monte Carlo (MC) methods use the classical potential functions of MD and MM but, the displacement of each atom is determined by random selection and direction. This method is more efficient in sampling space and ideal for simulating real or ideal polymers. Unfortunately, no correlation between space and time is possible [44, 45].

1.5.7 Coarse-grained Models

Coarse-grained (CG) methods use approximations whereby groups of atoms are designated as singular entities. Average parameter sets are applied to describe the behaviour of these entities. CG methods are mainly applied to large biomolecules such as lipids and membrane structures where fine details of individual atoms are not crucial and too computationally expensive [44, 45].

1.6 A Closer Look at Molecular Dynamics Simulations

MD simulations represent a widely used deterministic method for observing the motion of atoms over time [44]. Each atom is regarded as a classical particle and the forces on such particles are modeled using Newtonian mechanics. The positions $\vec{r}$, and the resulting forces of the classical particle can then be determined using Newton's second Law of Motion [48]

$$\vec{F}_i = m_i \frac{\Delta^2 \vec{r}_i}{\Delta t^2} = -\frac{\partial U(\vec{r}_i \ldots \vec{r}_N)}{\partial \vec{r}_i} \tag{1.7}$$

where i is the particle index, t is time, m is the mass of the particle and U the potential energy function [47]. Newton’s First (inertia) and Third (action-reaction) Laws of Motion [48] are also accounted for in MD simulations. Thus, a particle moving without any external force will continue its uniform trajectory, and for every particle interaction there is an equal and opposite reaction.

Since an MD simulation models a system of particles at the molecular level, a trajectory of all particles will generate a series of microscopic states. These microscopic states can be used to calculate macroscopic properties such as structure, thermodynamic (temperature, pressure, density) and other properties (thermal conductivity, diffusion) by applying statistical mechanics [44, 49]. Statistical mechanics provides several tools that can be used to extract useful information from a MD simulation. Such tools include ensemble averaging which represents bulk properties that describe the average effect on a system from all the particles acting together. Fluctuations can describe how the fixed average properties can vary from the average at any instant in time under equilibrium conditions. Distribution functions describe how the properties of the bulk system are shared among the component atoms.

The concept of ensemble is a key concept in statistical mechanics. For a given molecular system, an ensemble is replicated many times so that all the copies possess the same attributes such as temperature, density, number of particles. The replicas will generally have different positions and velocities. The microscopic state generated as a result differs slightly but at the same time each replica possesses the same attributes. The individual replicas, bulk properties can vary at any instantaneous moment, however, the real bulk property value is calculated as an average of all the replicas. The fluctuations provide an instantaneous value about the mean ensemble average. When performing an MD simulation, a new arrangement (configuration) of atoms as a function of time is produced and new instantaneous values of bulk properties are generated. To calculate a thermodynamic quantity, an ensemble average needs to be made which can be produced from successive configurations from the simulation. The Ergodic Hypothesis [49] states that the ensemble average (replicas of system) from a simulation is equal to an average over time of a single system (one replica) provided enough configurations from a simulation are sampled and averaged.

Under a microcanonical ensemble, [44, 45] the replicas of the system possess a constant number of particles N, a constant volume V, and a constant energy E, hence denoted as NVE. This ensemble corresponds to an isolated system. Under a canonical ensemble, the replicas of the system possess a constant number of particles N, a constant volume V, and a constant temperature T, hence denoted as NVT. The NVT ensemble corresponds to a system that is in thermal equilibrium with its surrounding environment.

1.6.1 Integration Algorithms

In MD simulations, a discritisation of time and space coordinates [50] is implemented in order to follow the trajectories of atoms in time. One widely used algorithm for determining these trajectories is the Verlet scheme [51]. It is based on a finite difference method (FDM) for approximating the solution to Newton's equation of motion. It is derived from a forward and backward Taylor series expansion of $\vec{r}(t+\Delta t)$ and $\vec{r}(t-\Delta t)$ around $\vec{r}(t)$, thus resulting in the following equation.

$$\vec{r}(t+\Delta t) = 2\vec{r}(t) - \vec{r}(t-\Delta t) + (\Delta t)^2 \left[\frac{\vec{F}(t)}{m}\right] + O(\Delta t)^4 \qquad (1.8)$$

The Verlet equation can be truncated after the second order term since the $O(\Delta t)^4$ term is negligible for sufficiently small values of Δt. This algorithm is stable and time reversible for simulations in the nanosecond time range. As a result of these important properties, long-term energy drift is minimized. This becomes important in simulations involving constant energy simulations.

Since the Verlet scheme is based on a finite difference method, it inherently introduces two types of errors, truncation error and round off error [45, 52]. The truncation error refers to the accuracy with which the FDM approaches the real solution of the differential equation. The round-off error encompasses all errors from implementing the FDM algorithm such as how many significant figures are kept at each stage of calculation and certain approximations used in calculating square roots, exponential and powers. The accumulation of these type of errors in each time step can be concerning for the accuracy of the overall numerical result. The accumulation of these errors over the length of a simulation can have drastic consequences. By reducing the time step to an appropriate value and writing more efficient code, one can reduce these forms of errors and hence gain better simulation results. The appropriate time step chosen [50] should be below the period of the fastest vibrational frequency of molecules in the system that use a harmonic potential.

1.6.2 Thermalization Schemes

At the molecular level, temperature [44, 45] is defined through the average kinetic energy for all the particles in a system. In order to study certain properties of a system, its temperature must be in equilibrium with the surrounding environment. Since the average kinetic energy is dependent on the velocity of the particles, the thermalization methods developed in MD simulations rescale the velocities to achieve thermal equilibrium at a specified temperature. One simple method is the stochastic [52] thermalization scheme where at random a particle or a collection of particles is selected and its velocity is rescaled to a bell-shaped Gaussian distribution. One common method of transforming a uniform distribution of random numbers to a Gaussian distribution is by using the Box-Muller transformation using the following equations,

$$Z_1 = \sqrt{-2\ln U_1}\cos\left(2\pi U_2\right) \tag{1.9}$$

$$Z_2 = \sqrt{-2\ln U_1}\sin\left(2\pi U_2\right) \tag{1.10}$$

where U_1 and U_2 are uniform random numbers and Z_1 and Z_2 are numbers transformed into a Gaussian distribution. The Nose-Hoover scheme [53, 54] is another widely used method to perform a constant temperature MD simulation whereby the average kinetic energy of the particles is held constant by scaling the velocities at each time step. This is achieved by introducing an additional term into the Verlet algorithm which behaves like an external system simulating a heat reservoir that is in thermal contact with the physical system. The additional term (ξ), multiplied by the current velocity of the particles is akin to a thermodynamic friction or drag force responsible for simulating the heat reservoir. The Nose-Hoover thermostat incorporating the frictional term has the following form

$$\vec{r}(t+\Delta t) = 2\vec{r}(t) - \vec{r}(t-\Delta t) + (\Delta t)^2\left[\frac{\vec{F}(t)}{m} - \xi(t+\Delta t)\cdot\vec{v}(t)\right] \tag{1.11}$$

$$\xi(t+\Delta t) = \xi(t) + \left[\sum_i^N m_i v_i^2(t) - gT_{set}\right]\frac{\Delta t}{2Q_N} \tag{1.12}$$

where $\vec{F}(t)$ is the force, m is the mass, $\vec{v}(t)$ is the velocity, $g = 3N - N_c$ where N is the number atoms, N_c is number of constraints per molecule (i.e. bonds, angle), g is the total number of degrees of freedom of the molecule, T_{set} is the preset temperature of the heat reservoir, Q_N is the Nose factor that controls the amount of thermal energy fluctuations.

1.6.3 Modelling Covalent Bonds

In MD simulations, methods have been developed to constrain covalent bond lengths without the introduction of harmonic potentials. Harmonic potentials are widely used to represent covalent bonds between atoms in molecules such as H_2O, where the atom is represented as a bead and the bond as a spring connecting the two beads. The potential energy is

$$U(r) = \frac{1}{2} k_s (r - r_0)^2 \qquad (1.13)$$

where k_s is the spring constant, r_0 is the equilibrium bond distance and M is the mass of the molecule. The vibrational frequency of the spring can be determined according to

$$f = \frac{1}{2\pi} \sqrt{\frac{k_s}{M}} \qquad (1.14)$$

In MD simulations, the time step is typically set below the fastest vibrational frequency [50] in the system.

Another technique developed to use larger time steps is to introduce constraint algorithms into the simulation. The constraint algorithms could replace the use of harmonic potentials representing covalent bonds. By increasing the size of the time step, longer simulation times and better ensemble averages could be generated. One such algorithm, SHAKE [44, 55], uses the method of undetermined multipliers to represent forces directed at covalent bonds to be constrained. This iterative procedure constrains the bond lengths to a certain set value and is applied to all the bonds for each molecule in the simulation.

1.6.4 Other Computed Quantities

During the development and testing stage of an MD simulation, many quantities [44, 45] are normally computed as a means of verifying the conservation of energy and momentum laws. The velocity $\vec{v}(t)$ of each atom can be calculated from taking the difference between the new $\vec{r}(t+\Delta t)$ and old $\vec{r}(t-\Delta t)$ positions of atoms according to

$$\vec{v}(t) = \frac{\vec{r}(t+\Delta t) - \vec{r}(t-\Delta t)}{2\Delta t} \tag{1.15}$$

The instantaneous temperature of the system is monitored according to

$$T(t) = \frac{\sum_{i}^{N} m_i \vec{v}_i^{\,2}(t)}{(3N - N_c)k_B} \tag{1.16}$$

where the numerator term is twice the kinetic energy of the system, where N is the number of atoms, N_c is number of constraints per molecule (i.e. bonds, angle), and k_B is the Boltzmann constant. From the velocities and current positions of the particles, the linear momentum $\vec{p}(t)$ for the system of particles is also monitored to verify the absence of linear drift

$$\vec{p}(t) = \sum_{i}^{N} m_i \vec{v}_i(t) \qquad (1.17)$$

Similarly, the angular momentum $\vec{L}(t)$ of the system of particles is easily calculated to monitor the torque on the particles according to

$$\vec{L}(t) = \sum_{i}^{N} m_i \vec{v}_i(t) \times \vec{r}_i(t) \qquad (1.18)$$

1.6.5 A Typical MD Simulation

Figure 1.6 describes a flow chart of a typical constant energy (NVE) MD simulation [50]. Initially, the parameters controlling all aspects of the simulation run (temperature, time step, parameters for the particles, number of particles, etc.) are read from an external file or from a subroutine within the program. Next, the initial coordinates of all the atoms in the simulation are read into the memory of the program. The initial configuration of the atoms of the system can be either in an artificial structure such as in a simple cubic lattice or can be from a pre–thermalized state from a previous simulation run. Once all the coordinates of the atoms are read into the program, the forces are calculated between all the atoms in pairs. The force equations are analytically derived from the potential functions (equation 1.7) and they are written in code. Subsequently, the newly calculated forces are used to determine the new positions of the atoms using an integration algorithm such as Verlet. If the system being studied contains molecules where the bonds and angles are to be constrained, then a SHAKE algorithm is applied to make adjustments to the positions of the atoms for each molecule. Once the positions are corrected using the SHAKE algorithm, other quantities such as velocities, from which kinetic energy and temperature, linear and angular momentum can be computed. During the initial development and testing stage of the code for an MD simulation, computing and monitoring such quantities provides a wealth of information on the performance and presence of potential errors in the code. Once testing and debugging are complete, a production run, is started without computing the extra quantities used in the testing stage. The last steps in the flow diagram are for writing the current positions of the atoms to an external file for future analysis as well as resetting the positions so that the next time step can be computed. At this point, a conditional statement checks if the time limit of the simulation has been reached. If yes, then the simulation terminates and if no, it continues.

In the computer code for such simulations, scaled or reduced units are used for the following reason. In the time scale and dimensions of molecular system, SI units can be either too large or too small on the respective order of 10^{10} or 10^{-10} [50]. When performing numerical operations with such large or small quantities, the resulting values can generate overflow in the buffer range for the variable type (such as double or float). By performing the calculation in reduced units, one can avoid these computational buffer limits and at the same time provide an extra means of debugging numerical errors when large or small numbers are generated. When it is time to write the results to an output file, the proper conversion factors are used to convert unit less quantities to real world values for positions (*Ångstroms*), velocity (*Ångstroms per picoseconds*), energy (*KJ* mol^{-1}), temperature (*Kelvin*), etc.

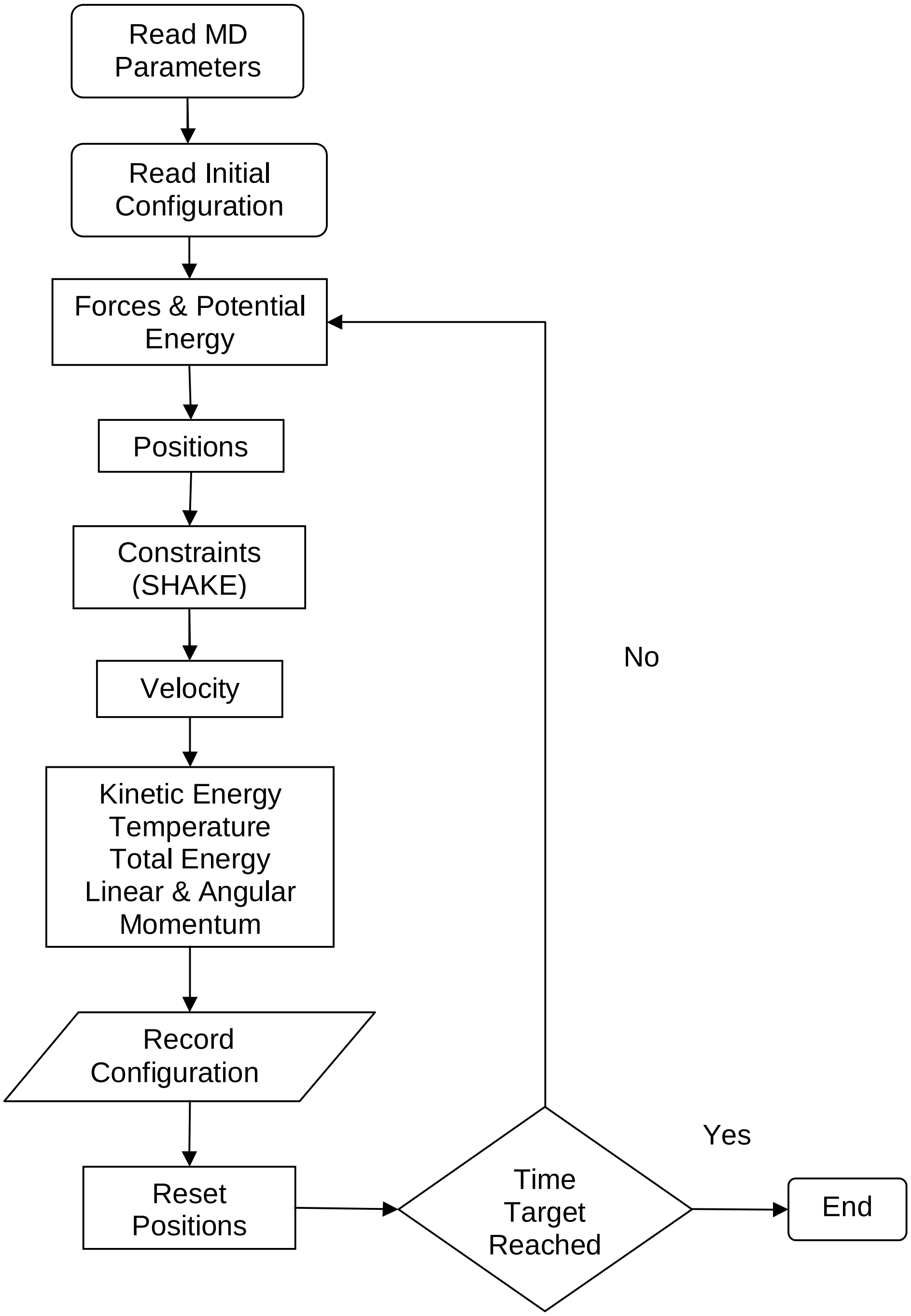

Figure 1.6. A typical constant energy MD simulation flow chart.

The code for the MD simulation for all the different projects in this thesis was written by the author in C++. The program is structured using object oriented design where each subroutine acts on the data. Separate subroutines were developed for performing specific tasks and calculations. The writing, small scale testing and debugging of each MD program as well as the programs written to analyze the data generated from the MD simulations was done on a desktop computer. Production runs of the MD simulations were performed on various computer cluster systems of the SHARCNET (www. sharcnet.ca) facilities over a period of weeks.

1.7 Water Models

Choosing a proper water model for computer simulations of charged droplets plays a significant role in the final results. The literature serves as a vast repository of various water models designed over the course of 40 years [56]. The water models can be classified based on several factors, the number of atomic sites (real and dummy atoms), incorporation of polarization effects and description as flexible or rigid structure. Rigid (constrained) models are the simplest and rely on non-covalent interactions for modeling electrostatics and van der Waals interactions with the use of a Coulomb and Lennard-Jones potentials, respectively. In addition to the non-covalent interactions, flexible models have to include covalent bonded interactions such as torsion bending and bond stretching using a harmonic potential. Each model is designed to fit to certain criteria based on physical parameters derived from experimental results. Such properties could include X-ray or neutron diffraction data, diffusion coefficients for transport effects and density. Although there exists ~ 40 water models, we will briefly compare in detail only a few of the models geometries and some of their important physical attributes.

The major difference between the non-polarizable and polarizable water models is the model's ability to be transferable to different phases (solid, liquid. gas) without re-parameterization. Currently, the non-polarizable models are designed to fit a particular phase. Fixed charge models cannot respond to electric fields and therefore do not account for electronic polarization effects which may be important in the condensed phase. Currently there are three different methods of accommodating polarization effects in water models, inducible dipole method, fluctuating charge method and Drude oscillator method.

The inducible dipole method [57] uses fixed charges on the atomic sites of the water model with an extra added atomic site coincident with the center of mass of the molecule representing a polarizable point. Then the contributions from the charge-charge, charge-dipole, dipole-dipole and self polarization of the molecule is calculated between all of the water molecules in the simulation.

The central idea behind the fluctuating charges method [58] is based on the electronegativities of atoms by treating charges as dynamical variables. This arises from considering atomic electrons as an electron gas. The electron gas can redistribute itself so that the electrochemical potential is equivalent at all atomic sites, this is known as electronegativity equalization (EE). Under this method, when an atomic site moves from one point to another, its electrostatic potential will also vary and as a result the charge on the site will vary accordingly. Hence, the charges on the molecule will respond to its environment. The conservation of charge is implemented by allowing charge transfers between atomic sites within a given molecule until electronegativities are equalized within the molecule.

The simplest method is the Drude oscillator model [59] where a dummy mass-less atomic site called the Drude particle is set at a distance from an oxygen atom attached by a harmonic oscillator and with a fixed charge. The extent to which the Drude particle responds to the electrostatic field is dependent on the spring constant and the partial charges on the atomic sites of the water molecule.

Even though the current polarizable models are unable to simultaneously describe the thermodynamic properties and structure of real water either, it is still an ongoing process to build better models to capture these properties.

1.7.1 TIP Water Models

The TIP3P [60], TIP4P [60] and TIP5P [61] are all rigid non-polarizable models. The TIP3P has three atomic sites corresponding to two hydrogens (H) and one oxygen (O). The TIP4P has four atomic sites and has been re-parameterized slightly by including a dummy site (D) a distance d_{OD} from the oxygen atom while at the same time shifting the charge from the oxygen site to the dummy site. The TIP5P, five atomic site model has been further re-parameterized by having two dummy sites where the charge from the oxygen atom is distributed between them. With the inclusion of the two dummy sites in this model, it resembles a tetrahedral geometry. Parameters for the TIP models are tabulated in Table 1.1 for comparison.

For comparing some of the relevant physical properties of the water models, the density, diffusion coefficient and radial distribution function (RDF) is also tabulated for the TIP models in Table 1.2. The water models density values can be compared with the density of water at ambient conditions, 298 K and 1 bar is 0.997 g cm^{-3}. The self diffusion coefficient for water measures the mobility of the waters but can also be seen as an indicator of the influence of hydrogen bonding on the molecular motions. The self diffusion coefficient for water at ambient conditions is 2.35×10^{-5} cm^2 s^{-1}. The RDF data provides a comparison of the microscopic structure of the models which can be used to judge the model’s ability to correlate with X-ray and neutron diffraction data. A comparison of individual peaks of the O-O, O-H and H-H radial distribution plots can be complicated so instead it is much easier to use an overall matching scale for the fit to the experimental results. A score of “acceptable” shows some secondary peaks not fully

	TIP3P	**TIP4P**	**TIP5P**
σ_{OO} (Å)	3.15061	3.15365	3.12
ε_{OO} (kJ mol^{-1})	0.6364	0.648	0.6694
d_{OH} (Å)	0.9572	0.9572	0.9572
d_{OD} (Å)		0.15	0.7
q_H (e)	+0.415	+0.52	+0.241
q_O (e)	-0.830	-1.04	
q_D (e)			-0.241
θ_{HOH} (°)	104.52	104.52	104.52
φ_{DOD} (°)			109.47

Table 1.1. Parameters of TIP water models.

	TIP3P	TIP4P	TIP5P
Density (g cm^{-3})	0.997	0.999	0.999
Diffusion ×10^{-5} (cm^2 s^{-1})	4.0	3.4	2.6
RDF match	Acceptable	Better	Excellent

Table 1.2. Physical properties of TIP water models.

matched while “better” provides a better match for those secondary peaks while “excellent” signals a perfect match of all the peaks.

1.7.2 Single Point Charge (SPC) Water Models

The SPC [62] and SPC/E [62] are rigid non-polarizable models while SPC/F [63] is a flexible non-polarizable model, and the SPCP [57] is a polarizable model. The SPC is a three atomic site model. The SPC/E is also a three atomic site model similar to the SPC model but with slight different charge values for the oxygen and hydrogens. The SPC/F is a three atomic site flexible model where a harmonic potential governs the HH bond distance. The bond stretching constant is 4431.53 kJ mol^{-1} $Å^{-2}$ and the equilibrium bond length is 1.012 Å [64]. The SPCP model is a four atomic site polarizable model with an extra site (M) bisecting the HOH angle. The parameters for the SPC models are tabulated in Table 1.3 and the physical properties in Table 1.4.

As can be seen from only a sampling of 7 models (Tables 1.2 and 1.4), there is no perfect water model to capture every single physical feature of the real substance. We chose the SPC/E model because it correlates with the density and diffusion coefficient data very well as well as the RDF data. None of the other three atomic site models (TIP3P and SPC) capture the density and diffusion coefficient well enough. The main drawback with the four and five atomic site TIP models is the extra calculations needed to account for the extra atomic sites. The same drawback would apply for the SPC/F model with an extra harmonic potential calculation. The polarizable model requires even more calculations since it uses the inducible dipole method discussed

	SPC	**SPC/E**	**SPC/F**	**SPCP**
σ_{OO} (Å)	3.166	3.166	3.166	3.166
ε_{OO} (kJ mol^{-1})	0.65	0.65	0.65	0.65
d_{OH} (Å)	1.0	1.0		1.0
d_{OD} (Å)				0.2
q_H (e)	+0.41	+0.4238	+0.41	
q_O (e)	-0.82	-0.8476	-0.82	
θ_{HOH} (°)	109.47	109.47		109.47

Table 1.3. Parameters of SPC water models. SPC/E was used throughout the following chapters.

	SPC	**SPC/E**	**SPC/F**	**SPCP**
Density (g cm^{-3})	0.97	1.0	0.998	0.95
Diffusion ×10^{-5} (cm^{2} s^{-1})	4.3	2.3	2.5	1.9
RDF match	Acceptable	Better	Better	Acceptable

Table 1.4. Physical properties of SPC water models.

earlier in section 1.7. Hence, the SPC/E model was chosen not only for its correlation with the physical parameters but also for it’s efficient calculation implementation.

1.8 Water and Ions

There are a great number of experimental and computational studies of water [65, 66] and ions of various types in the literature. A large portion of these studies focus on neutral water slabs while only a small number deal with charged droplets. For example, Jungwirth and others, [67, 68], using polarizable ion models were able to show surface enhancement of halide ions (Cl^-, Br^-) using MD and *ab initio* calculations in slab geometries. Other studies using either non-polarizable water and ion models [69] or polarizable ion models [70] provided results that did not always agree with one another. The importance of these studies present some ideas for understanding what factors influence the position of the ions in charged droplets.

The behavior of ions and water was also investigated by spectroscopic techniques such as vibrational sum-frequency spectroscopy (VSFS) [71]. VSFS is unique in that it can probe the vibrational spectrum of molecules at the liquid/vapor interface [72, 73]. This is achieved by applying light pulses from a visible laser beam and a tunable infrared (IR) laser onto the interface. One laser beam is polarized in the parallel and the other in the perpendicular plane. Then, by scanning the photon energy of the tunable IR laser, a vibrational spectrum of interfacial molecules can be obtained by monitoring the generated sum frequency signal. VSFS is similar to second harmonic generation [74] (SHG) which involves the summation of two fixed frequency light beams.

While others [75-79] looked at hydrophobic interactions at the interface using VSFS methods, Raymond and associates [80] focused on the hydrogen bonding of water molecules on the surface region of water and sodium halide solutions. They used VSFS to probe the vibrational stretching mode of the OH from waters that straddle the surface region as defined by Gibbs surface. The Gibbs surface is a region where the concentration of solutes per unit volume is different than the bulk environment. In their study, they found that concentration of halides at the interface is lower than results reported from MD simulations. Other SHG studies also posed similar interfacial results for ions [77, 81-85].

The debate as to where the ions reside in aqueous systems is not conclusive since SHG and VSFS experiments do not coincide with MD simulations with polarizable ion and solvent models. In the most recent study by Caleman and co-workers [86], investigation using MD simulations concluded that bulk versus surface ion preferences are balanced between entropic and enthalpic driving forces. Polarizable Cl^-, Br^-, I^- ions are enthalpically driven to the surface by partially desolvated halide anions which allow for more water-water interactions. The group also found that F^- bulk preference is entropically driven while alkali cations are enthalpically driven to the bulk due to favorable ion-water interactions. They concluded that polarizable models can mask the energetics of ion solvation effects.

Most past studies focused on neutral aqueous solutions with ions instead of charged droplets. In one of the first MD simulations of aqueous charged droplets Znamenskiy and co-workers [87] attempted to determine by which pathway (IEM or CRM) analyte ions form in the ESI-MS process. They observed that ions such as hydronium and diglycine were distributed in concentric layers within the interior of the droplets as opposed to the lying on the surface as suggested by Rayleigh. The presence of the ions resulted in shape fluctuations and surface protrusions resulting in solvated ion ejection in agreement with the IEM model.

In another study, Consta et al [88] performed MD simulations of charged aqueous droplets to examine the droplet disintegration process containing ions such as Na^+, Ca^{+2}, Cl^- as charge carriers. With the use of a novel transfer reaction coordinate, the shape of entire droplet relative to the ions is captured and describe the fluctuations that pertain to the mechanism of droplet disintegration.

As for the stability of charged droplets, Marginean [89] and coworkers observed a reduction of charge on electrosprayed droplets through the formation of thin nanojets by use of MD simulations. They observed that moderately charged nanojets would reduce to spherical shapes whereas droplets closer to the Rayleigh limit preferred splitting into two droplets thereby reducing the charge on each droplet and hence being below the Rayleigh limit and thus more stable.

Caleman and coworkers [90] investigated the evaporation of singly charged water clusters with various ions (Na^+, Cl^-, NH_4^+). They concluded that presence of Na^+ and Cl^- reduced evaporation due to charge-dipole interactions between water and Na^+ and Cl^- . Also the study indicated water clusters with positive ions are more unstable than negative ions. This was attributed to a larger Cl^- - Cl^- ion repulsion than similar repulsion by Na^+ - Na^+ and NH_4^+ - NH_4^+. As a result, positively charged droplets had a higher tendency for disintegration than negative charged droplets. This can be attributed to the higher charged density for the positive ions in comparison to the negative ions.

1.9 Water and Proteins

Although studies on low molecular weight analytes have provided a wealth of knowledge on the behavior of charged droplets, in ESI-MS the focus of study is on protein and peptides. In a recent study, Consta [22] explored the structures of a charged droplet with a polyhistidine ion when it is beyond the Rayleigh limit. It was shown that changes in the structure of the droplet resulted in “spike” shapes along the surface. These sharp shapes prevent counter ions from solvating properly and being ejected which in turn would reduce the overall charge on the droplet to a stable point [91, 92].

In an attempt to answer some of the lingering questions as to how unfolded proteins become charged, Konermann [93], used a model protein chain with solvents and protons as LJ particles to simulate the final stages of the ESI-MS process. It was revealed from the protonation pattern, that residues with little surface area exposure was less likely to show protonation. At the same time, positive side chains naturally repel protons and prevent further protonation. One of the limitations of this study was that a one atomic site solvent model was used instead of one of the more established three or four site water models discussed earlier in section 1.7.

In another MD study by Patriksson and coworkers [94], five partially hydrated protein structures were simulated in a vacuum environment to investigate if the protein structure in the gas phase is similar to that in the solution phase. In the end, it was uncovered that the structures in the gas phase did not vary drastically from the solution phase structure.

1.10 Scope of Thesis

The starting point for the questions investigated in this thesis arose from many previous charged droplet studies as already discussed. The Konermann [93] work was one of those studies that provided a base to start from. Some of the questions that arose as a result of the past studies include the following: How do charged droplets disintegrate and by which mechanism? Is there a correlation between the size of the analyte ion and the mechanism? Where does the charge reside in a droplet, on the surface or the interior? Through the use of MD simulations, we will attempt to answer some of these questions.

Overall, this work demonstrates how MD simulations can be used to gain better understanding of the nature of charged droplets as evidenced in the ESI-MS field. For the first project (Chapter 2), a proton model was developed to understand how a highly mobile charge diffuses through a water droplet and could potentially serve as a framework for modelling protonation of side chains in a protein system. This first project gave rise to many new questions, e.g., where the charge on the water droplet resides. This led to another project where we used sodium ions and an equivalent anion to model the problem (Chapter 3). With a simple method of mapping out the charge on the water droplet, we were able to show that even though the ions remained solvated within the droplet, the charge had been transferred to the surface via dipole orientation of the waters. In a further study (Chapter 4), the evaporation rates, efficiency of ion ejection and overall composition of a droplet was studied with methanol/water mixtures. It was found that due to the methyl group, the hydrogen bonding network was weaker than that of waters and hence a level of microsegregation occurred with methanol molecules preferring the outer periphery as opposed to the well hydrogen bonded waters composing the interior of the droplet. In the final project (Chapter 5), the behaviour of a relatively large model protein was explored by varying its hydrophobicity and observing how it relates to the ionization mechanism(s).

1.11 References

1. Zhao, S., G.S.P. Castle, and K. Adamiak, *Factors affecting deposition in electrostatic pesticide spraying.* J. Electrostat., 2008. **66**: p. 594-601.

2. Khain, A., V. Arkhipov, M. Pinsky, Y. Feldman, and Y. Ryabov, *Rain enhancement and fog elimination by seding with charged droplets. Part I: Theory and numerical simulations.* J. Appl. Meteorol., 2004. **43**: p. 1513-1529.

3. Dole, M., L.L. Mack, R.L. Hines, R.C. Mobley, L.D. Ferguson, and M.B. Alice, *Molecular beams of macroions.* J. Chem. Phys., 1968. **49**: p. 2240-2249.

4. Fenn, J.B., *Electrospray Wings for Molecular Elephants (Nobel Lecture).* Angew. Chem. Int. Ed., 2003. **42**: p. 3871-3894.

5. Fenn, J.B., M. Mann, C.K. Meng, S.F. Wong, and C.M. Whitehouse, *Electrospray Ionization for Mass Spectrometry of Large Biomolecules.* Science, 1989. **246**: p. 64-71.

6. Fenn, J.B., M. Mann, C.K. Meng, S.F. Wong, and C.M. Whitehouse, *Electrospray ionization-principles and practice.* Mass Spectrom Rev., 1990. **9**: p. 37-70.

7. Atkins, P., *Physical Chemistry*. 6th ed. 1998, New York: W. H. Freeman & Co.

8. El-Aneed, A., A. Cohen, and J. Banoub, *Mass Spectrometry, Review of the Basics: Electrospray, MALDI, and Commonly Used Mass Analyzers.* Appl. Spectrosc. Rev., 2009. **44**: p. 210-230.

9. Tanaka, K., *The Origin of Macromolecule Ionization by Laser Irradiation (Nobel Lecture).* Angew. Chem. Int. Ed., 2003. **42**: p. 3861-3870.

10. Bruins, A.P., *Mechanistic aspects of electrospray ionization.* J. Chromatogr. A, 1998. **794**: p. 345-357.

11. Karas, M. and U. Bahr, *Matrix-Assisted Laser Desorption-Ionization (MALDI) Mass Spectrometry of Biological Molecules*, in *Mass Spectrometry in Biomolecular Sciences*, R.M. Caprioli, A. Malorni, and G. Sindona, Editors. 1996, Kluwer: Dordrecht, Boston, London. p. 33-49.

12. Iavarone, A.T., J.C. Jurchen, and E.R. Williams, *Supercharged Protein and Peptide Ions Formed by Electrospray Ionization.* Anal. Chem., 2001. **73**: p. 1455-1460.

13. Rayleigh, L., *On the Equilibrium of Liquid Conducting Masses charged with Electricity.* Phil. Mag., 1882. **14**: p. 184-186.

14. Konermann, L., *A Simple Model for the Disintegration of Highly Charged Solvent Droplets during Electrospray Ionization.* J. Am. Soc. Mass Spectrom., 2009. **20**: p. 496-506.

15. Kebarle, P., *A brief overview of the present status of the mechanisms involved in electrospray mass spectrometry.* J. Mass. Spectrom., 2000. **35**: p. 804-817.

16. Kebarle, P. and L. Tang, *From ions in solution to ions in the gas phase: The mechanism of electrospray mass spectrometry.* Anal. Chem., 1993. **65**: p. 972A-986A.

17. Tang, L. and P. Kebarle, *Dependence of ion intensity in electrospray mass spectrometry on the concentration of the analytes in the electrosprayed solution.* Anal. Chem., 1993. **65**: p. 3654-3668.

18. Storozhev, V.B. and E.N. Nikolaev, *Computer simulations of the fission process of charged nanometre droplets.* Phil. Mag., 2004. **84**: p. 157-171.

19. Gomez, A. and K. Tang, *Charge and fission of droplets in electrostatic sprays.* Phys. Fluids, 1994. **6**: p. 404-414.

20. Hogan, C.J. and P. Biswas, *Monte Carlo Simulation of Macromolecular Ionization by Nanoelectrospray.* J. Am. Soc. Mass Spectrom., 2008. **19**: p. 1098-1107.

21. Ichiki, K. and S. Consta, *Disintegration Mechanisms of Charged Aqueous Nanodroplets Studied by Simulations and Analytical Models.* J. Phys. Chem. B, 2006. **110**: p. 19168-19175.

22. Consta, S., *Manifestation of Rayleigh Instability in Droplets Containing Multiply Charged Macroions.* J. Phys. Chem. B, 2010. **114**: p. 5263–5268.

23. Iribarne, J.V. and B.A. Thomson, *On the evaporation of small ions from charged droplets.* J. Chem. Phys., 1976. **64**: p. 2287-2294.

24. Thomson, B.A. and J.V. Iribarne, *Field induced ion evaporation from liquid surfaces at atmospheric pressure.* J. Chem. Phys., 1979. **71**: p. 4451.

25. de la Mora, F.J., *Electrospray Ionization of large multiply charged species proceeds via Dole's charged residue mechanism.* Anal. Chim. Acta, 2000. **406**: p. 93-104.

26. Peschke, M., U.H. Verkerk, and P. Kebarle, *Features of the ESI Mechanism that Affect the Observation of Multiply Charged Noncovalent Protein Complexes and the Determination of the Association Constant by the Titration Method.* J. Am. Soc. Mass Spectrom., 2004. **15**: p. 1424-1434.

27. Felitsyn, N., M. Peschke, and P. Kebarle, *Origin and number of charges observed on multiply-protonated native proteins produced by ESI.* Int. J. Mass Spectrom. Ion Proc., 2002. **219**: p. 39-62.

28. Nesatyy, V.J. and M.J.-F. Suter, *On the conformation-dependent neutralization theory and charging of individual proteins and their non-covalent complexes in the gas phase.* J. Mass Spectrom., 2004. **39**: p. 93-97.

29. Heck, A.J.R. and R.H.H. Van den Heuvel, *Investigation of intact protein complexes by mass spectrometry.* Mass Spectrom. Rev., 2004. **23**: p. 368-389.

30. Iavarone, A.T. and E.R. Williams, *Mechanism of Charging and Supercharging Molecules in Electrospray Ionization.* J. Am. Chem. Soc., 2003. **125**: p. 2319-2327.

31. Kaltashov, I.A. and A. Mohimen, *Estimates of Protein Surface Area in Solution by Electrospray Ionization Mass Spectrometry.* Anal. Chem., 2005. **77**: p. 5370-5379.

32. Nguyen, S. and J.B. Fenn, *Gas-phase ions of solute species from charged droplets of solutions.* Proc. Natl. Acad. Sci. U.S.A., 2007. **104**: p. 1111-1117.

33. Kebarle, P. and M. Peschke, *On the Mechanisms by which the charged droplets produced by electrospray lead to gas phase ions.* Anal. Chim. Acta, 2000. **406**: p. 11-35.

34. Gamero-Castaño, M. and F. de la Mora, *Kinetics of small ion evaporation from the charge and mass distribution of multiply charged clusters in electrosprays.* J. Mass Spectrom., 2000. **35**: p. 790-803.

35. Onsager, L. and N.N.T. Samaras, *The Surface Tension of Debye-Hückel Electrolytes.* J. Chem. Phys., 1934. **2**: p. 528-536.

36. Labowsky, M., J.B. Fenn, and J. Fernandez de la Mora, *A continuum model for ion evaporation from a drop: effect of curvature and charge on ion solvation energy.* Anal. Chim. Acta, 2000. **406**: p. 105-118.

37. Gamero-Castaño, M. and F.J. de la Mora, *Mechanisms of electrospray ionization of singly and multiply charged salt clusters.* Anal. Chim. Acta, 2000. **406**: p. 67-91.

38. Loscertales, I.G. and J.F. de la Mora, *Experiments on the kinetics of field evaporation of small ions from droplets.* J. Chem. Phys., 1995. **103**: p. 5041-5060.

39. Kebarle, P. and U.H. Verkerk, *Electrospray: From Ions in Solutions to Ions in the Gas Phase, What We Know Now.* Mass Spectrom. Rev., 2009. **28**: p. 898-917.

40. Mazor, S., *The history of the microcomputer - Invention and evolution.* P. IEEE, 1995. **83**: p. 1601-1608.

41. Cramer, C.J., *Essentials of Computational Chemistry: Theory and Models*. 2nd ed. 2004: John Wiley & Sons, Ltd.

42. Jensen, F., *Introduction to Computational Chemistry*. 2nd ed. 2007: John Wiley & Sons, Ltd.

43. Car, R. and M. Parrinello, *Unified approach for molecular dynamics and density-functional theory.* Phys. Rev. Lett., 1985. **55**: p. 2471-2474.

44. Allen, M.P. and D.J. Tildesley, *Computer Simulation of Liquids*. 1987: Clarendon Press.

45. Haile, J.M., *Molecular Dynamics Simulations: Elementary Methods*. 1992: John Wiley & Sons Inc.

46. Klein, M.L. and W. Shinoda, *Large-Scale Molecular Dynamics Simulations of Self-Assembling Systems.* Science, 2008. **321**: p. 798-800.

47. Stone, A.J., *Intermolecular Potentials.* Science, 2008. **321**: p. 787-789.

48. Halliday, D., R. Resnick, and K.S. Krane, *Physics*. 4 ed. 1992, New York: Wiley.

49. Hill, T.L., *An Introduction to Statistical Thermodynamics*. 2nd ed. 1986: Dover Publications.

50. Rapaport, D.C., *The Art of Molecular Dynamics Simulations*. 2004: Cambridge University Press.

51. Verlet, L., *Computer "Experiments" on Classical Fluids. I. Thermodynamical Properties of Lennard-Jones Molecules.* Phys. Rev., 1967. **159**: p. 98-103.

52. Andersen, H.C., *Molecular dynamics simulations at constant pressure and/or temperature.* J. Chem. Phys., 1980. **72**: p. 2384-2393.

53. Nose, S., *A molecular dynamics method for simulations in the canonical ensemble.* Mol. Phys., 1984. **52**: p. 255-268.

54. Hoover, W.G., *Canonical dynamics: Equilibrium phase-space distributions.* Phys. Rev. A, 1985. **31**: p. 1695-1697.

55. Forester, T.R. and W. Smith, *SHAKE, Rattle and Roll: Efficient Constraint Algorithms for Linked Rigid Bodies.* J. Comput. Chem., 1998. **19**: p. 102-111.

56. Guillot, B., *A reappraisal of what we have learnt during three decades of computer simulations of water.* J. Mol. Liq., 2002. **101**: p. 219-260.

57. Chialvo, A.A. and P.T. Cummings, *Engineering a simple polarizable model for the molecular simulation of water applicable over wide ranges of state conditions.* J. Chem. Phys., 1996. **105**: p. 8274-8281.

58. Rick, S.W., S.J. Stuart, and B.J. Berne, *Dynamical fluctuating charge force fields: Application to liquid water.* J. Chem. Phys., 1994. **101**: p. 6141-6156.

59. Lamoureux, G., A.D. MacKerell, and B. Roux, *A simple polarizable model of water based on classical Drude oscillators.* J. Chem. Phys., 2003. **119**: p. 5185-5197.

60. Jorgensen, W.L. and C. Jensen, *Temperature dependence of TIP3P, SPC and TIP4P water from NPT Monte Carlo simulations: Seeking temperatures of maximum density.* J. Comput. Chem., 1998. **19**: p. 1179-1186.

61. Mahoney, M.W. and W.L. Jorgensen, *A five-site model for liquid water and the reproduction of the density anomaly by rigid, nonpolarizable potential functions.* J. Chem. Phys., 2000. **112**: p. 8910-8922.

62. Berendsen, H.J.C., J.R. Grigera, and T.P. Straatsma, *The missing term in effective pair potentials.* J. Phys. Chem., 1987. **91**: p. 6269-6271.

63. Toukan, K. and A. Rahman, *Molecular dynamics study of atomic motions in water.* Phys. Rev. B, 1985. **31**: p. 2643-2648.

64. Yuet, P.K. and D. Blankenschtein, *Molecular Dynamics Simulation Study of Water Surfaces: Comparison of Flexible Water Models.* J. Phys. Chem. B, 2010. **114**: p. 13786-13795.

65. Ball, P., *Water as an Active Constituent in Cell Biology.* Chem. Rev., 2008. **108**: p. 74-108.

66. Chaplin, M., *Do we underestimate the importance of water in cell biology?* Nat. Rev. Mol. Cell Bio., 2006. **7**: p. 861-866.

67. Jungwirth, P. and D.J. Tobias, *Molecular structure of salt solutions: A new view of the interface with implications for heterogeneous atmospheric chemistry.* J. Phys. Chem. B, 2001. **105**: p. 10468-10472.

68. Jungwirth, P. and D.J. Tobias, *Ions at the air/water interface.* J. Phys. Chem. B, 2002. **106**: p. 6361-6373.

69. Knipping, E.M., M.J. Lakin, K.L. Foster, P. Jungwirth, D.J. Tobias, R.B. Gerber, D. Dabdub, and B.J. Finlayson-Pitts, *Ion-enhanced interfacial chemistry on aqueous NaCl aerosols.* Science, 2000. **288**: p. 301-306.

70. Chang, T.-M. and L.X. Dang, *Recent advances in molecular simulations of ion solvation at liquid interfaces.* Chem. Rev., 2006. **106**: p. 1305-1322.

71. Richmond, G.L., *Molecular bonding and interactions at aqueous surfaces as probed by vibrational sum frequency spectroscopy.* Chem. Rev., 2002. **102**: p. 2693-2724.

72. Garrett, B.C., G.K. Schenter, and A. Morita, *Molecular simulations of the transport of molecules across the liquid/vapor interface of water.* Chem. Rev., 2006. **106**: p. 1355-1374.

73. Garrett, B.C., *Ions at the Air/Water Interface.* Science, 2004. **303**: p. 1146-1147.

74. Hayashi, M., Y.-J. Shiu, K.K. Liang, S.H. Lin, and Y.R. Shen, *Theory of time-resolved sum frequency generation and its applications to vibrational dynamics of water.* J. Phys. Chem. A, 2007. **111**: p. 9062-9069.

75. Chandler, D., *Oil in troubled waters.* Nature, 2007. **445**: p. 831-832.

76. Chandler, D., *Interfaces and the driving force of hydrophobic assembly.* Nature, 2005. **437**: p. 640-647.

77. Du, Q., E. Freysz, and Y.R. Shen, *Surface vibrational spectroscopic studies of hydrogen bonding and hydrophobicity.* Science, 1994. **264**: p. 826-828.

78. Trudeau, T.G., K.C. Jena, and D.K. Hore, *Water Structure at Solid Surfaces of Varying Hydrophobicity.* J. Phys. Chem. C, 2009. **113**: p. 20002-20008.

79. Moore, F.G. and G.L. Richmond, *Integration or Segregation: How do molecules behave at oil/water interfaces?* Acc. Chem. Res., 2008. **41**: p. 739-748.

80. Raymond, E.A. and G.L. Richmond, *Probing the Molecular Structure and Bonding of the Surface of Aqueous Salt Solutions.* J. Phys. Chem. B, 2004. **108**: p. 5051-5059.

81. Shultz, M.J., C. Schnitzer, D. Simonelli, and S. Baldelli, *Sum frequency generation spectroscopy of the aqueous interface: Ionic and soluble molecular solutions.* Int. Rev. Phys. Chem., 2000. **19**: p. 123-153.

82. Shultz, M.J., S. Baldelli, C. Schnitzer, and D. Simonelli, *Aqueous solution/air interfaces probed with sum frequency generation spectroscopy.* J. Phys. Chem. B, 2002. **106**: p. 5313-5324.

83. Ishiyama, T. and A. Morita, *Molecular dynamics analysis of interfacial structures and sum frequency generation spectra of aqueous hydrogen halide solutions.* J. Phys. Chem. A, 2007. **111**: p. 9277-9285.

84. Benjamin, I., *Vibrational spectrum of water at the liquid/vapor interface.* Phys. Rev. Lett., 1994. **73**: p. 2083-2086.

85. Brown, E.C., M. Mucha, P. Jungwirth, and D.J. Tobias, *Structure and vibrational spectroscopy of salt water/air interfaces: Predictions from classical molecular dynamics simulations.* J. Phys. Chem. B, 2005. **109**: p. 7934-7940.

86. Caleman, C., J.S. Hub, P.J. van Maaren, and D. van der Spoel, *Atomistic simulation of ion solvation in water explains surface preference of halides.* Proc. Nat. Acad. Sci., 2011. **108**: p. 6838-6842.

87. Znamenskiy, V., I. Marginean, and A. Vertes, *Solvated Ion Evaporation from Charged Water Droplets.* J. Phys. Chem. A, 2003. **107**: p. 7406-7412.

88. Consta, S., K.R. Mainer, and W. Novak, *Fragmentation mechanisms of aqueous clusters charged with ions.* J. Chem. Phys., 2003. **119**: p. 10125-10132.

89. Marginean, I., V. Znamenskiy, and A. Vertes, *Charge Reduction in Electrosprays: Slender Nanojets as Intermediates.* J. Phys. Chem. B, 2006. **110**: p. 6397-6404.

90. Caleman, C. and D. van der Spoel, *Evaporation from water clusters containing singly charged ions.* Phys. Chem. Chem. Phys., 2007. **9**: p. 5105-5111.

91. Hogan, C.J., J.A. Carroll, H.W. Rohrs, P. Biswas, and M.L. Gross, *Charge Carrier Field Emission Determines the Number of Charges on Native State Proteins in Electrospray Ionization.* J. Am. Chem. Soc., 2008. **130**: p. 6929-6927.

92. Hogan, C.J., J.A. Carroll, H.W. Rohrs, P. Biswas, and M.L. Gross, *Combined Charged Residue-Field Emission Model of Macromolecular Electrospray Ionization.* Anal. Chem., 2009. **81**: p. 369-377.

93. Konermann, L., *A Minimalist Model for Exploring Conformational Effects on the Electrospray Charge State Distribution of Proteins.* J. Phys. Chem. B, 2007. **111**: p. 6534-6543.

94. Patriksson, A., E. Marklund, and D. van der Spoel, *Protein Structures under Electrospray Conditions.* Biochemistry, 2007. **46**: p. 933-945.

Chapter 2 – Molecular Dynamics Simulations of Electrosprayed Water Nanodroplets: Internal Potential Gradients, Location of Excess Charge Centers, and 'Hopping' Protons

2.1 Introduction

Water is involved in countless (bio)chemical processes. Its distinctive structure and capability to form a fluctuating network of hydrogen bonds lead to a high dielectric constant and surface tension, hydrophobic solvation, and many other unique properties. Much remains to be learned about the behavior of this seemingly simple compound [1, 2]. Water clusters and nanodroplets represent a particularly interesting research area. Infrared spectroscopy can provide structural insights for small systems (up to dozens of H_2O molecules) [3, 4] but with increasing size this approach quickly becomes unfeasible. Computer simulations have been extensively used in this area, going back to the advent of molecular dynamics (MD) in the 1970s [5-7]. In recent years there has been renewed interest in the behavior of water clusters fuelled, in part, by advances in theoretical chemistry [8-13]. Another important aspect is the central role of nanodroplets in electrospray ionization (ESI) mass spectrometry (MS), which has become one of the most widely used analytical techniques [14-16].

ESI generates intact and multiply protonated gas phase ions from analytes in solution, thereby making them amenable to mass spectrometric analysis. Mixtures of water and methanol or acetonitrile may be used as solvent, but many applications employ a purely aqueous solvent. The analyte solution is passed through a metal capillary to which a high (usually positive) potential has been applied. Electrophoretic charge separation leads to the enrichment of positive charge at the capillary tip. As a result, the solution is distorted into a Taylor cone that emits micrometer-sized solvent droplets carrying excess positive charge [17]. The net charge on these droplets can be due to different species. Protons play an important role [18], partly because analyte solutions often contain formic or acetic acid [19]. Protons are also generated by water oxidation at the metal/liquid interface, i.e., $2\ H_2O \rightarrow 4\ H^+ + 4\ e^- + O_2$ [20, 21]. NH_4^+ ions represent another common charge carrier due to the widespread use of ammonium acetate as solvent additive, in addition to Na^+ and K^+ which are ubiquitous contaminants [22, 23]. Solvent evaporation increases the charge density to the point where the cohesive forces within the droplet are balanced by Coulombic repulsion. This so-called Rayleigh limit is characterized by the relationship [24, 25]

$$z_R e = 8\pi\sqrt{\varepsilon_0 \gamma R^3} \tag{2.1}$$

where z_R is the number of elementary charges e, ε_0 is the permittivity of the vacuum, γ is the surface tension, and R is the droplet radius. Jet fission at the Rayleigh limit leads to the formation of progeny droplets that carry away a small percentage of the parent droplet mass, but a disproportionately large amount of charge [26-31]. Repeated evaporation/fission cycles ultimately result in the formation of nanometer-sized droplets from which gas-phase analyte ions are liberated [24, 32].

The mechanism of ion formation from nanodroplets continues to be a matter of debate. According to the charged residue model (CRM), evaporation to dryness releases the analyte which retains some of the droplet's charge [33]. An alternative framework, the ion evaporation model (IEM) stipulates that analyte ions can be ejected from the droplet surface by field emission [34]. It has been suggested that large species such as proteins follow the CRM mechanism and that the IEM applies to smaller analytes [24, 35]. Evidence for CRM ionization in the case of natively folded proteins comes from the observation of protonation states that are close to z_R of protein-sized water droplets [18, 22, 36-38]. However, studies that have tested the predicted dependence on surface tension (Equation 2.1) yielded contradicting results [18, 39]. Rayleigh's model [25, 40] represents a theory that is based on continuum fluid and charge. Hence, it is not clear if this framework still applies to nanodroplets, and if the use of a macroscopic surface tension γ is adequate in this size regime [41-43]. As a result of this and other issues, the proposed distinction of CRM vs. IEM according to analyte size is not universally accepted [44, 45].

To develop a better understanding of ESI nanodroplets a few research groups have begun to study these systems through MD simulations. For example, Consta and coworkers [41, 46, 47] explored the disintegration of clusters consisting up to 1600 SPC/E waters that were charged with Na^+, Cl^-, or Ca^{2+}. Similarly, Vertes et al. [48, 49] simulated droplets of ~4500 TIP3P molecules that contained various charged species.

Models of proton-containing ESI droplets have to take into account the extremely high mobility of H^+. In bulk water the proton diffusion coefficient is 9.3×10^{-9} m^2 s^{-1}, roughly one order of magnitude larger than that of small metal cations [50-52]. This high mobility is attributed to a mechanism whereby a structural defect migrates through the hydrogen bonding network, as first proposed by Grotthus [1, 2, 53-55]. In contrast, "conventional" hydrated ions undergo relatively slow Stokes diffusion due to friction from their surroundings [56]. Despite notable recent progress [12, 43, 57], the high mobility of protons continues to be a challenge for MD studies on ESI droplets. For example, H_3O^+ was modeled as simple Stokes particle in the work of Znamenskiy et al. [48]. Our group has recently developed a minimalist MD framework to describe the formation of gas-phase protein ions during ESI. Protons were modeled as point charges that could hop between solvent molecules and on to the protein [58]. A shortcoming of that model is the description of solvent as a Lennard-Jones (LJ) fluid, neglecting hydrogen bonding and dielectric effects caused by the H_2O architecture.

The current work addresses some of the limitations of those earlier ESI studies. We develop a framework for carrying out nanodroplet MD simulations based on the SPC/E water model [59], but modified to include protons as classical particles that can diffuse by hopping between solvent molecules. The model parameters are chosen using a heuristic approach that is validated through a comparison of simulated and measured proton diffusion coefficients. We then proceed to use this framework for examining the behavior of nanodroplets close to the Rayleigh limit, specifically examining the implications of solvent ordering at the liquid/vacuum interface. Results for conventional Stokes ions are also included. This work provides the foundation for more realistic future simulations of the ESI process.

2.2 Methods

2.2.1 MD Simulations

Simulations and data analysis was carried out based on C++ code developed by the one of the authors (E.A.). The classical equations of motion were integrated using the Verlet algorithm [60, 61] with a time step of 2 fs. We studied nanodroplets ranging in size up to 1248 water molecules in a vacuum environment. These clusters were generated from an initial cubic lattice where the individual molecules were placed in a random orientation. Using constant energy MD aided by a center-symmetric external potential this lattice was coalesced into a droplet having approximately spherical geometry. The external potential was then removed and the system was thermalized using the Nose-Hoover scheme [62, 63] for 80 ps at 100 K. This was followed by thermalization at 320 K for 40 ps. The simulation was subsequently switched to constant energy MD (at $T \approx$ 320 K) for typically 1 ns, during which particle coordinates were extracted every 0.4 ps for analysis. LJ potentials were truncated at 7.5 Å but no cutoffs were used for Coulombic interactions.

2.2.2 Water Model

H_2O molecules were represented on the basis of the non-polarizable SPC/E model with an O-H bond distance of 1.0 Å and a H-O-H angle of 109.47° [59]. SPC/E was chosen here because it addresses limitations of earlier water models, while still maintaining a relatively low computational cost [1]. The interaction between two H_2O molecules (a) and (b) is given by a combination of LJ and Coulomb potentials [41]

$$U_{ab}^{water} = 4\varepsilon_{OO}\left[\left(\frac{\sigma_{OO}}{r_{OO}^{ab}}\right)^{12} - \left(\frac{\sigma_{OO}}{r_{OO}^{ab}}\right)^{6}\right] + \frac{1}{4\pi\varepsilon_0}\sum_{i=1}^{3}\sum_{j=1}^{3}\left(\frac{q_i^a q_j^b}{r_{ij}^{ab}}\right) \tag{2.2}$$

where i and j refer to the H, O, H atoms of water (a) and (b), respectively. LJ parameters are $\sigma_{OO} = 3.166$ Å and $\varepsilon_{OO} = 0.6502$ kJ mol^{-1}, with charges $q_O = -0.8476\,e$ and q_H = 0.4238 e. The bond angle and bond lengths of each water molecule were constrained using the SHAKE algorithm [64, 65].

2.2.3 Mobile Proton Model

Various methods have been developed for modeling proton solvation and transport [8, 56, 66]. These include quantum mechanical treatments [66-68], *ab initio* MD [9, 69, 70], and Car-Parrinello methods [12, 71]. Most of these high level approaches use density-functional theory for potential energy calculations "on the fly" while the simulation proceeds, a strategy that results in considerable computational cost [43, 53]. The multistate empirical valence bond technique [55, 72] represents an alternative method that has been successfully applied to relatively large systems, most recently to a cubic simulation box containing 256 water molecules and up to 16 HCl pairs under periodic boundary conditions [12].

For the current work we approximate H$^+$ behavior on the basis of a simple heuristic approach which describes protons as highly mobile classical point charges with a mass of 1 amu. The strategy is easy to implement and computationally inexpensive. A related model has previously been used for simulating proton hopping within LJ clusters

[58], but the combination with SPC/E water in this work is new. The pairwise repulsion between protons is given by the standard r^{-1} Coulomb potential. Proton-water interactions are modeled based on two potentials. The first is a *trapping potential* that allows proton binding to the oxygen site of an SPC/E water. The three "H" in such a H_3O^+ configuration are not equivalent. Instead, the added proton is treated as distinct entity that carries one elementary charge and fluctuates around the oxygen center. The other two hydrogens maintain their SPC/E charges, bond angles and lengths. The second contribution is a *modified Coulomb potential,* which accounts for electrostatic proton-water interactions. The two potentials are described in detail below.

2.2.4 Trapping Potential

The trapping potential assigned to every SPC/E oxygen has a Lorentzian shape according to

$$U^{trap}(r) = -\alpha\left(\frac{\left[{}^{fwhm}\!/_{2}\right]^2}{r^2+\left[{}^{fwhm}\!/_{2}\right]^2}\right) \tag{2.3}$$

where r is the proton-oxygen distance, $fwhm$ = 7.1 Å is the width of the distribution, and α was chosen to be 10 k_BT. The proximity of oxygen sites within a water cluster results in the superposition of individual trapping potentials, thereby generating a three-dimensional energy landscape where protons can thermally hop from one oxygen to another while still being trapped within the cluster. This coalescence of curves is analogous to the merging of potential wells seen in high level proton transfer simulations upon bringing individual water molecules in contact with each other [51, 53, 68].

It is instructive to examine the energy landscape obtained from the combined contributions of individual trapping potentials. Figure 2.1A depicts a one-dimensional representation of such a landscape for a nanodroplet consisting of 1248 waters that is centered around the origin of a Cartesian coordinate system. The data were obtained by scanning through the cluster at $y = 0$ and $z = 0$. Ideally, the plot should have a "box shape" with a bottom that is more or less flat (i.e. having thermally accessible barriers on the order of k_BT), such that all oxygen sites within the cluster are equally accessible. Evidently, this is not the case for the profile in Figure 2.1A. Instead, the curve shows a pronounced minimum close to $x = 0$ which would cause artifactual proton enrichment in the center of the cluster. This problem can be eliminated by truncating $U^{trap}(r)$ at a suitable cutoff distance r_{co}, thereby generating a modified trapping potential $T(r)$ according to

$$T(r) = U^{trap}(r) - U^{trap}(r_{co}) \qquad \text{for } r \le r_{co}$$

and (2.4)

$$T(r) = 0 \qquad \text{for } r > r_{co}$$

An approximately box-shaped profile with relatively small internal barriers is obtained for r_{co} = 4.5 Å (Figure 2.1B). A smaller value of 3.2 Å increases the roughness of the energy landscape, thereby impeding proton diffusion within the cluster (Figure 2.1C). Reducing r_{co} even further to 1.2 Å (Figure 2.1D) produces individual potential wells that

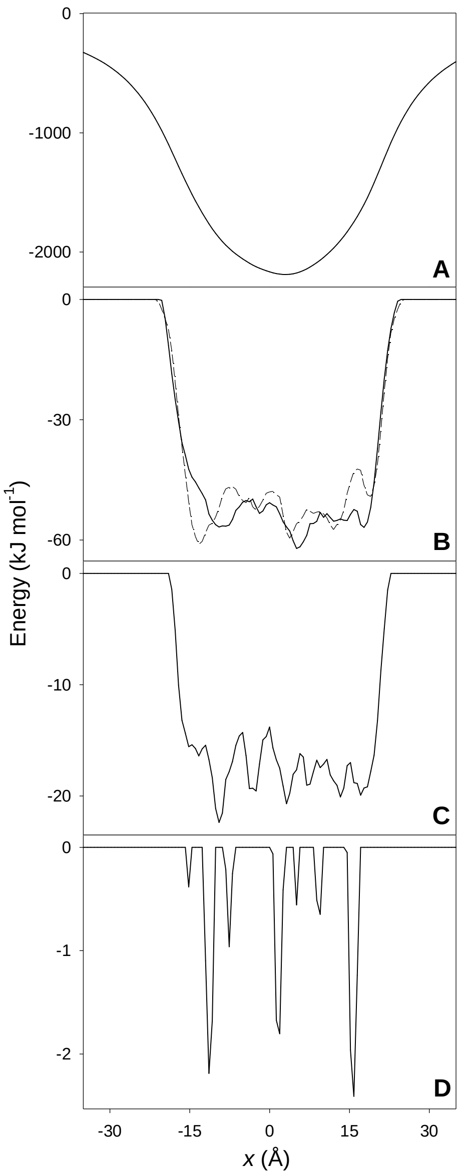

Figure 2.1. One-dimensional representations of the energy landscape experienced by a single proton within a nanodroplet consisting of 1248 water molecules, each of which contributes a trapping potential $T(r)$ according to Equation 2.4. (A) no cutoff, $r_{co} = \infty$; (B) $r_{co} = 4.5$ Å; (C) $r_{co} = 3.2$ Å; (D) $r_{co} = 1.2$ Å. Solid lines refer to a simulation time of $t = 320$ ps, representing one particular cluster configuration. The dashed line in panel B is for $t = 400$ ps. Charge-charge interactions are not considered for the plots shown here.

are quite shallow and no longer merged together. For the simulations discussed below we used a $T(r)$ profile with r_{co} = 4.5 Å (Figure 2.1B). This choice of parameter results in a sufficiently deep potential energy drop relative to the the vacuum environment, preventing thermally activated ejection of unsolvated protons from the nanodroplet. At the same time, the energy landscape within the cluster is relatively flat with barriers that can easily be surmounted, which is the prerequisite for rapid proton hopping. The solid lines in Figure 2.1 represent potentials for a single time point chosen at random from a constant energy MD trajectory. The barrier heights and locations undergo constant fluctuations due to the motions and self diffusion of water molecules. This is illustrated in Figure 2.1B, where the dashed and solid profiles represent potential curves for time points that are 80 ps apart.

2.2.5 Modified Coulomb Potential

Modeling electrostatic interactions between a proton and oxygen according to the standard Coulomb expression

$$U^{Coul} = \frac{q_{pro} q_O}{4\pi\varepsilon_0} \frac{1}{r} \tag{2.5}$$

is not feasible when employing the trapping potential concept outlined in the preceding section. Numerical instabilities arise due to the precipitous drop of $-r^{-1}$ for transiently encountered proton-oxygen distances close to zero (Figure 2.2, solid line). This pathological behavior is an artifact of the point charge approximation. The problem can be circumvented by using an expression that mimics $-r^{-1}$ for large distances, while adopting a more or less constant value for small r. Similar strategies have previously been employed in the context of path integrals [73]. A suitable approach is to use a "pseudo Coulomb" potential U^{PC} of the form

$$U^{PC}(r) = \frac{q_{pro} q_O}{4\pi\varepsilon_0}\left[\frac{1}{r}\left(1 - \frac{A^6}{A^6 + r^6}\right) + C\left(\frac{A^6}{A^6 + r^6}\right)\right] \tag{2.6}$$

where A and C are adjustable parameters. The behavior of two different U^{PC} profiles is illustrated in Figure 2.2 (dashed and dotted lines), where distances r and energies E are expressed as dimensionless quantities according to $r' = r\,\sigma_{OO}^{-1}$ and $E' = E\,\varepsilon_{OO}^{-1}$ [64]. The potential $U^{PC}1$ with $A = 2.6$ and $C = 0.4$ mimics the standard Coulomb curve down to $r' \approx 2.6$ before performing a smooth truncation. $U^{PC}2$ with $A = 1$ and $C = 1.2$ departs from the Coulomb curve at $r' \approx 1$ and results in a much deeper well. Simulation results for both parameter sets will be discussed below. Equation 2.6 was used not only for modeling proton-oxygen interactions, but also those between protons and SPC/E hydrogens (based on the same parameters A and C as in the oxygen case, but using q_H instead of q_O, along with the corresponding distances r).

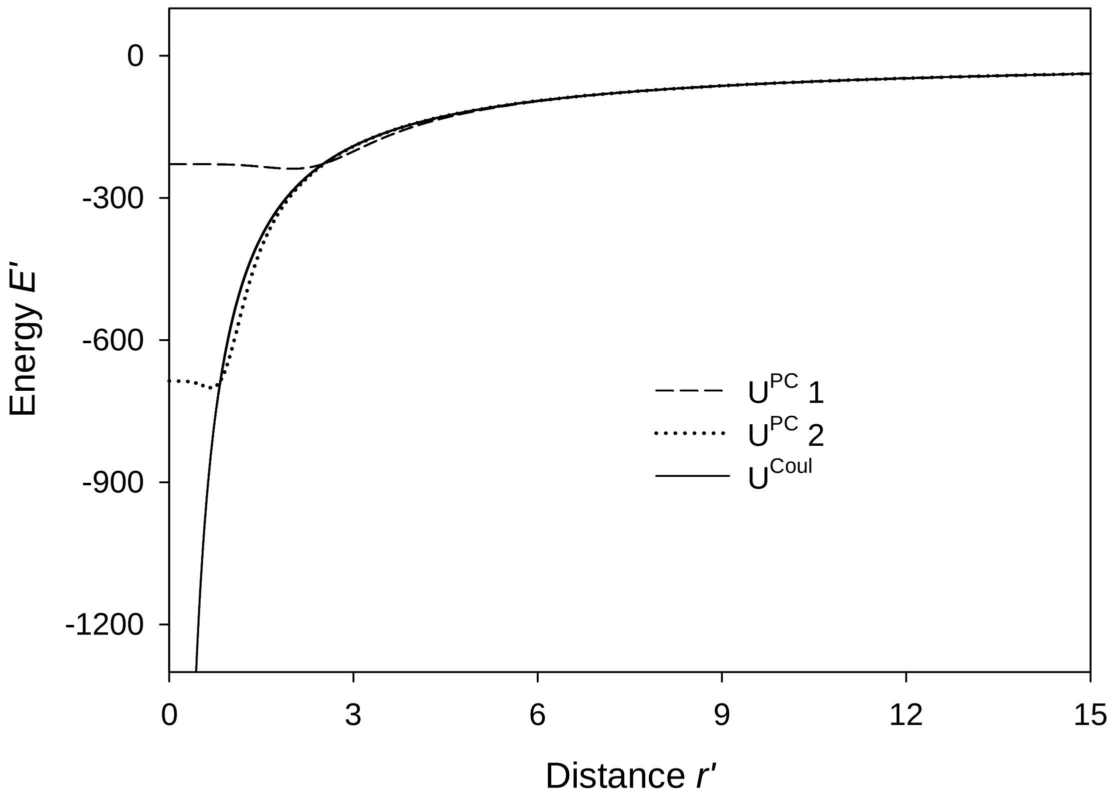

Figure 2.2. Different potentials for describing charge-charge interactions between a proton and a SPC/E oxygen. Solid line: standard Coulomb potential (Equation 2.5). Dashed and dotted profiles: "pseudo-Coulomb" potentials $U^{PC}1$ and $U^{PC}2$ with different parameters A and C (Equation 2.6). Proton-oxygen distances r' and energy values E' are expressed as dimensionless quantities, as explained in the text.

2.3 Results and Discussion

Multiply protonated water nanodroplets were studied by MD simulations at a temperature of $T \approx 320$ K. A snapshot of a cluster consisting of 582 water molecules and seven protons is depicted in Figure 2.3A. Similarly, Figure 2.3B shows a nanodroplet containing 1248 waters and ten protons. The droplet radii in the two panels are on the order of 16 and 21 Å, respectively, the density is about 0.96 g cm^{-3}, and the protonation states correspond to roughly 85% of the Rayleigh limit (Equation 2.1). During the 1 ns simulation runs the droplets maintained an approximately spherical shape, but with an undulating surface. Evaporation is rare on this time scale, affecting less than ten water molecules for each of the systems studied. Similarly, proton ejection was not observed. The metastable nature of the droplets under the conditions used here is consistent with previous simulations [48], and with experimental data which indicate that evaporation and fission occur on much longer (microsecond) time scales [26].

2.3.1 Proton Mobility under Different Modeling Conditions

Figure 2.4 illustrates path traces for the seven protons within a cluster consisting of 582 waters. Only 200 ps segments out of the 1 ns trajectories are shown to prevent cluttering. To provide a basis for evaluating the performance of our hopping proton framework we initially modeled protons as solvated ions that undergo Stokes diffusion. For this purpose proton-water interactions were described analogous to those for Na$^+$, [74] with $\sigma_{io} = 2.876$ Å, $\varepsilon_{io} = 0.5216$ kJ mol^{-1}, LJ parameters, and standard Coulomb

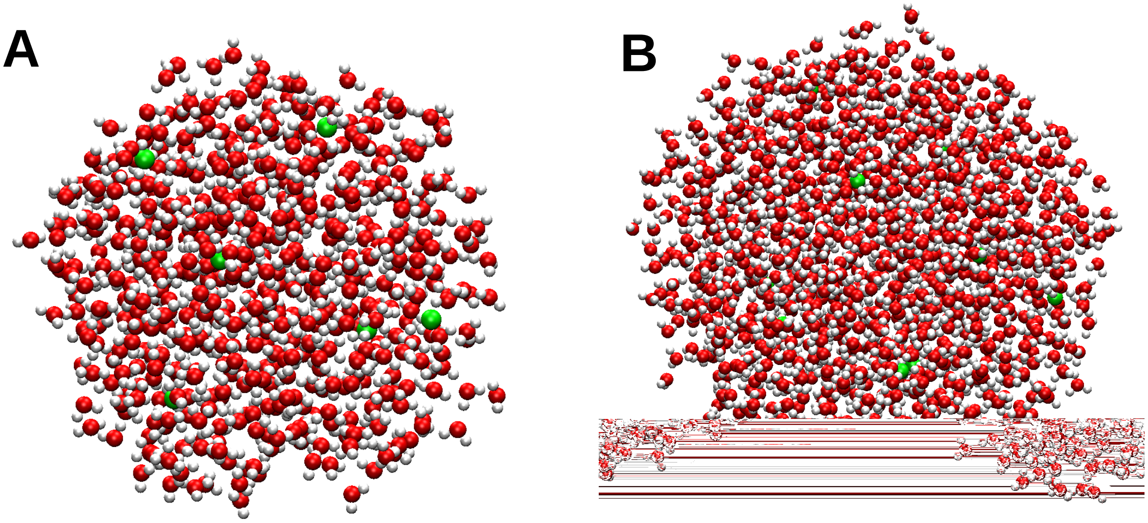

Figure 2.3. Snapshots of MD nanodroplet simulations for systems consisting of (A) 582 waters and 7 protons and (B) 1248 waters and 10 protons. Red and white represents oxygen and hydrogen, respectively. Protons are depicted as large green spheres for visualization purposes. The image was generated using VMD (developed by the Theoretical and Computational Biophysical Group, UIUC).

interactions (Equation 2.5), but using a particle mass of 1 amu. Under these conditions the individual H^+ trajectories are confined to relatively small regions of the nanodroplet (Figure 2.4A). Qualitatively similar path traces are obtained when using the hopping proton model with potential $U^{PC}2$ (Figure 2.4B). Since proton mobilities predicted by Stokes diffusion are known to be much too low [50-52], it is clear that also the scenario of Figure 2.4B is inadequate. A totally different behavior is observed when employing the mobile proton model with the more shallow potential $U^{PC}1$. Under these conditions each of the proton trajectories covers a dramatically larger range (Figure 2.4C).

An alternative way to analyze the proton dynamics under the different conditions of Figure 2.4 is to tally the number of waters visited during the simulation time window. For this purpose a H_2O molecule was marked as being visited or protonated if a proton ventured within 2.5 Å of the corresponding oxygen. Return visits to the same oxygen were not counted. Within the Stokes framework every proton contacts roughly 40 water molecules during 1 ns (Figure 2.5A). Only a slightly higher number of solvent molecules is visited when carrying out the simulation by employing the hopping proton model with potential $U^{PC}2$ (Figure 2.5B). In contrast, the greatly enhanced mobility within the $U^{PC}1$ hopping proton framework allows each proton to jump rapidly between a very large number of host oxygens, leading to the visitation of up to 500 water molecules within the time window studied (Figure 2.5C). Qualitatively similar results were obtained for nanodroplets consisting of 1248 waters and ten protons (data not shown). The behavior depicted in Figure 2.5C is consistent with previous reports that found proton hopping from one site to another roughly every 1 - 2 ps [43].

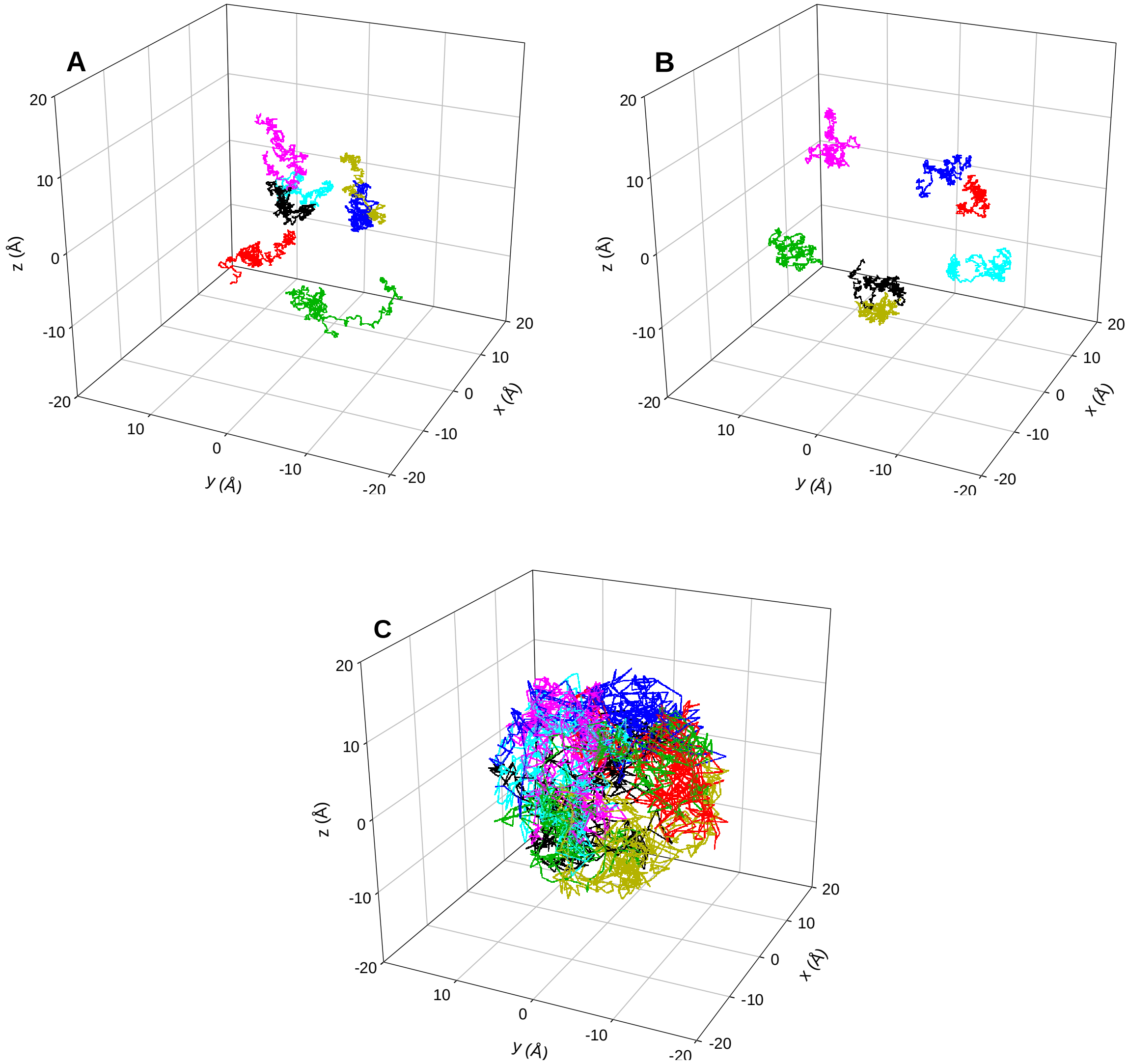

Figure 2.4. 200 ps trajectories of seven protons within a nanodroplet consisting of 582 water molecules under different conditions. (A) Protons modeled as Na^+-like Stokes particles; (B) mobile proton model using potential $U^{PC}2$; (C) mobile proton model using potential $U^{PC}1$. Each proton trajectory is shown in a different color.

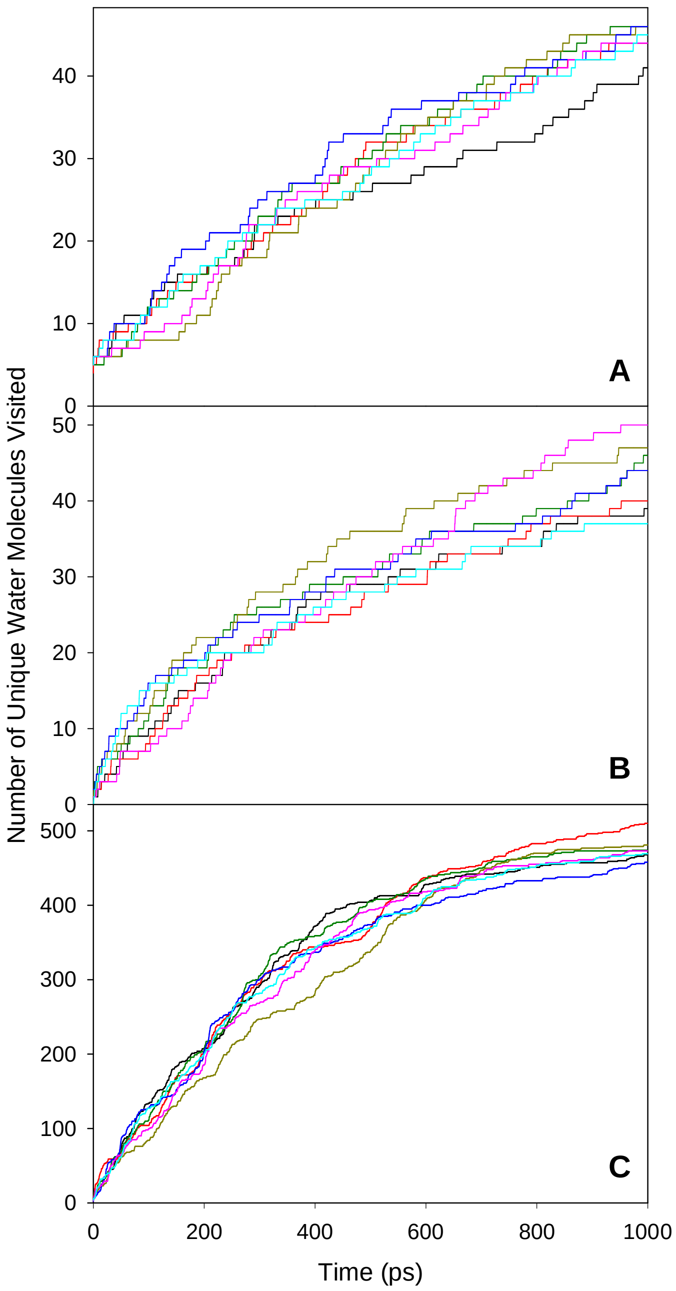

Figure 2.5. Number of unique water molecules (oxygen sites) visited by individual protons under the conditions of Figure 2.4. (A) Protons modeled as Stokes particle; (B) mobile proton model using potential $U^{PC}2$; (C) mobile proton model using potential $U^{PC}1$. The proton color scheme is the same as for the previous Figure.

The pronounced differences in mobility for hopping proton simulations with $U^{PC}1$ and $U^{PC}2$ (Figure 2.2) are related to the roughness of the three-dimensional energy landscapes experienced by the H^+ particles [75, 76]. $U^{PC}2$ provides a fairly rugged landscape, with deep minima (oxygen sites) and large positive spikes (hydrogens). These obstacles dramatically slow down proton diffusion. The more shallow potential $U^{PC}1$, on the other hand, provides a much smoother landscape that promotes high mobility.

2.3.2 Diffusion Coefficient

The mean square displacement (MSD) of particles that undergo unconstrained diffusion in three dimensions follows the equation [7, 66]

$$\left\langle \left| \vec{r}(0) - \vec{r}(t) \right|^2 \right\rangle = 6Dt \tag{2.7}$$

where D is the diffusion coefficient. Simulations employing the $U^{PC}1$ hopping proton model result in the plot shown in Figure 2.6. This graph represents an average of five simulation runs for nanodroplets containing 10 protons and 1248 water molecules (fifty H^+ trajectories in total). The MSD profile initially shows approximately linear behavior, as predicted by Equation 2.7. For longer times the curve levels off towards an MSD value of *ca*. 400 $Å^2$. This deviation from linearity is attributed to confinement of the proton motion within the droplet. The proton diffusion coefficient was estimated by linear regression in an early time window of 0.4 to 14 ps where confinement effects are least pronounced (Figure 2.6, inset), and a value of $D = (9.2 \pm 0.7) \times 10^{-9}\ m^2\ s^{-1}$ was found.

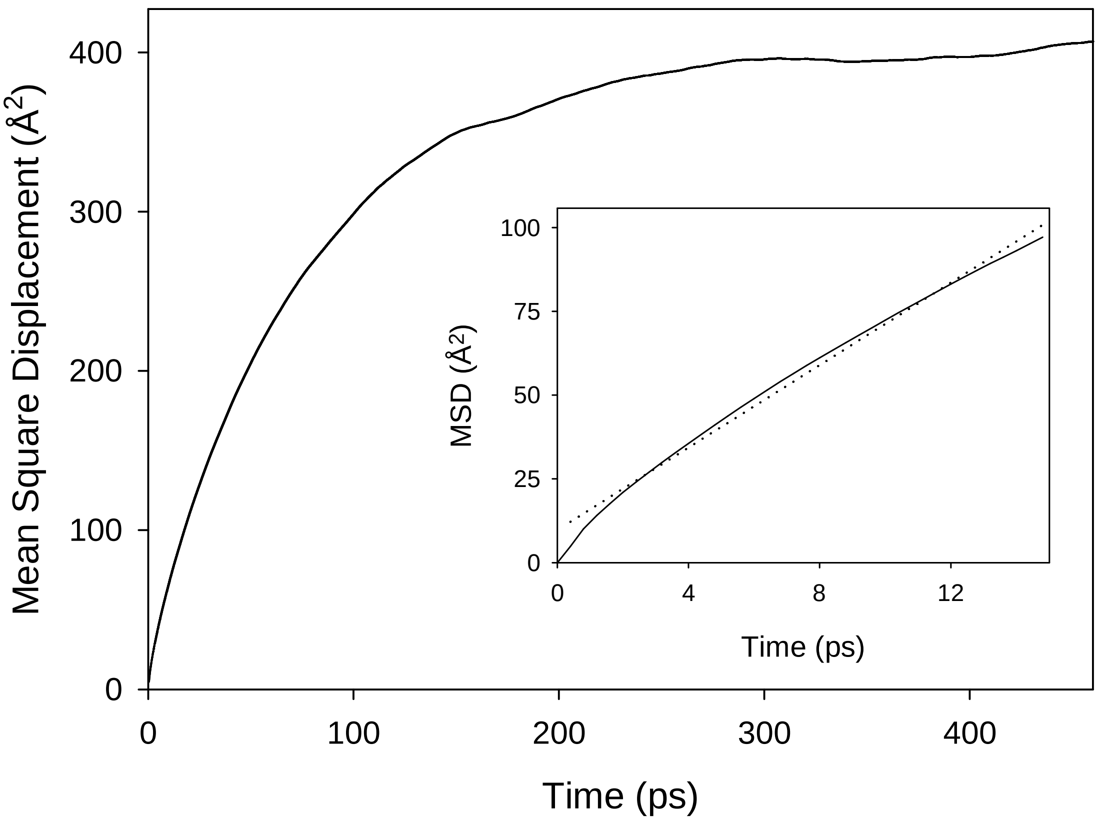

Figure 2.6. Proton mean square displacement for nanodroplets consisting of 1248 waters and ten protons, obtained using the U^{PC}1hopping proton model. The data shown represent an average of five simulation runs (50 trajectories in total). Inset: Data for one selected run (average of ten trajectories). The dotted line represents a linear regression plot according to Equation 2.7.

Experimental data for H^+ diffusion in water nanoclusters are not available, but our simulation result is in close agreement with the value in bulk solution, $D = 9.3 \times 10^{-9}$ m^2 s^{-1} [50-52]. Applying the same framework to nanodroplets consisting of 582 waters and seven protons results in a somewhat lower value of $D = (6.6 \pm 0.3) \times 10^{-9}$ m^2 s^{-1}, reflecting the more pronounced confinement effects for these smaller clusters (data not shown). Overall, the data discussed here suggest that the $U^{PC}1$ mobile proton model provides a simple, yet effective framework for simulating the proton dynamics in water nanodroplets.

2.3.3 Radial Distributions

From here on we will discuss the behavior of systems that consist of 1248 waters and ten excess charges, representing a regime that is typical for nanodroplets during the final stages of ESI [26]. All H^+ diffusion results presented below were obtained by using the $U^{PC}1$ potential.

Figure 2.7A depicts radial distribution functions for a droplet charged with ten mobile protons. The oxygen and hydrogen density is approximately constant from the center up to radial positions of *ca*. 17 Å. This is followed by a sigmoidal decrease in density between 17 and 26 Å, corresponding to a diffuse water/vacuum interface [48]. The droplet radius of $R \approx 21$ Å cited earlier reflects the midpoint of this transition. A completely different picture is observed for protons (dashed line in Figure 2.7A), which exhibit a distribution with a broad maximum at $r \approx 14$ Å and a minimum around 8 Å. Although counting statistics lead to some noise for $r < 5$ Å, it is clear that a substantial

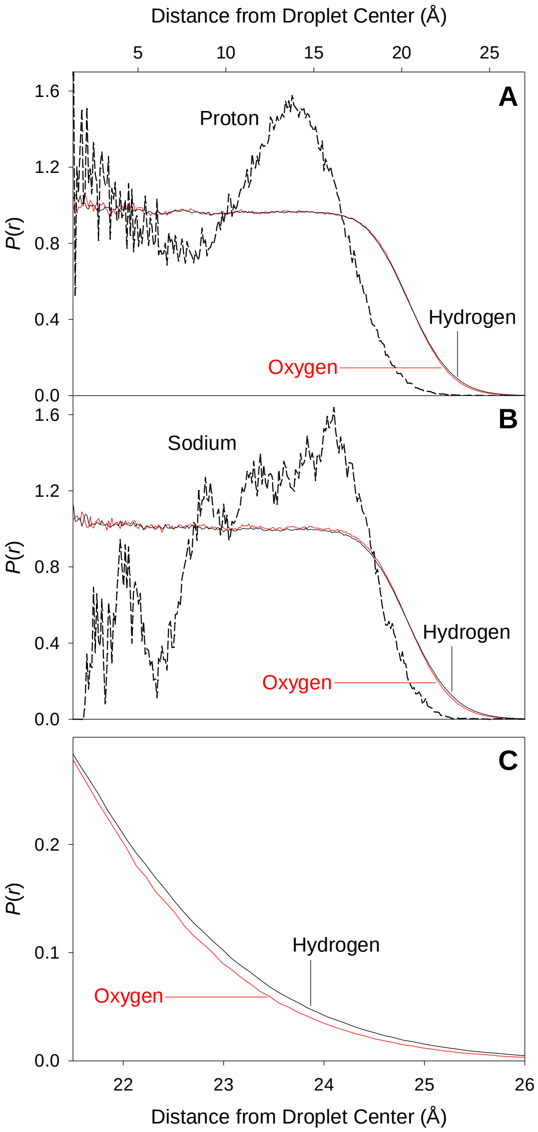

Figure 2.7. (A) Radial distribution of oxygen, hydrogen, and protons, averaged over five 1 ns runs. The data are for 1248 waters and ten protons, modeled based on the $U^{PC}1$ mobile proton model. (B) Similar to panel A, but for nanodroplets containing ten Na^+ ions instead of protons. (C) Expanded region of the outermost water layers from panel A (similar plots [not shown] were obtained based on the data in panel B). All histograms were corrected for the $4\pi r^2$ surface area of individual bins originating from the spherical geometry.

proton density is encountered around the cluster center.

The shape of the proton radial distribution in Figure 2.7A is unexpected. Simple continuum models suggest that excess charge on water droplets should be located exclusively within the outermost solvent layers, and this notion is widely used in the ESI-MS literature [18, 19, 32, 34, 77-80]. Such a behavior is analogous to that of metallic conductors charged with electrons. For example, ref. [81] states that "*excess charge placed on an isolated conductor moves entirely to the outer surface of the conductor. None of the excess charge is found within the body of the conductor*". The thin layer of surface charge predicted by this statement is very different from the proton behavior observed in Figure 2.7A.

Simulations were also carried out for droplets carrying ten Na^+ ions, in order to determine whether the lack of a charged surface layer is specific to the type of charge carrier. The σ_{iO} and ε_{iO} parameters employed for sodium were the same as for Figure 2.4A, but with the proper Na^+ mass of 23 amu [74]. The radial distribution of sodium (Figure 2.7B) is dominated by a broad and slightly structured band centered around 14 Å, which roughly coincides with that observed for mobile protons in panel A. An additional smaller feature is seen around 5 Å. Despite some differences in their radial distribution functions, it is readily apparent that both Na^+ and H^+ share a tendency to occupy radial positions within the droplet, instead of forming a thin layer the liquid/vacuum interface. A similar behavior was observed for nanodroplets charged with NH_4^+ ions (not shown). The sodium data in Figure 2.7B are consistent with earlier work on water slabs [13, 57]. Similar observations were also made in the MD study by Znamenskiy et al. [48] where ESI nanodroplets were charged with different ionic Stokes particles (H_3O^+ and protonated diglycine). The authors of that work tried to rationalize the presence of charge in the droplet interior on the basis of a two-dimensional model, but such arguments have little relevance for ion distributions in three dimensions [77, 78, 81].

A key aspect for understanding why protons and sodium ions (Figure 2.7A, B) are not confined to a thin surface layer is the realization that water nanodroplets do *not* represent a homogeneous continuum. Instead, ordering at the liquid/vacuum interface leads to potential gradients that strongly affect the trajectories of charged solutes. The non-random orientation of H_2O molecules at vacuum and hydrophobic interfaces has been examined previously [42, 82-87]. However, the implications of this phenomenon for the distribution of charge carriers within nanodroplets have been studied to a much lesser extent.

A first indication of the mechanism by which surface water ordering might affect the behavior of charged solutes is obtained from Figure 2.7C, which focuses on the hydrogen and oxygen radial distributions in the outermost droplet layers. In this range the distribution function of hydrogen is significantly above that of oxygen. This attests to the prevalence of molecular orientations where surface water exposes hydrogen, rather than oxygen, to the vacuum. Due to the partial charges within each H_2O molecule, this ordering generates a double layer at the droplet surface that is positive on the outside and negative on the inside.

Experimentally it has not been possible to determine the sign and magnitude of the electric field associated with interfacial water ordering [43, 88-90]. However, computational studies consistently show that the direction of the potential drop is in agreement with our findings (i.e., positive on the outside) [43, 91]. The magnitude of this

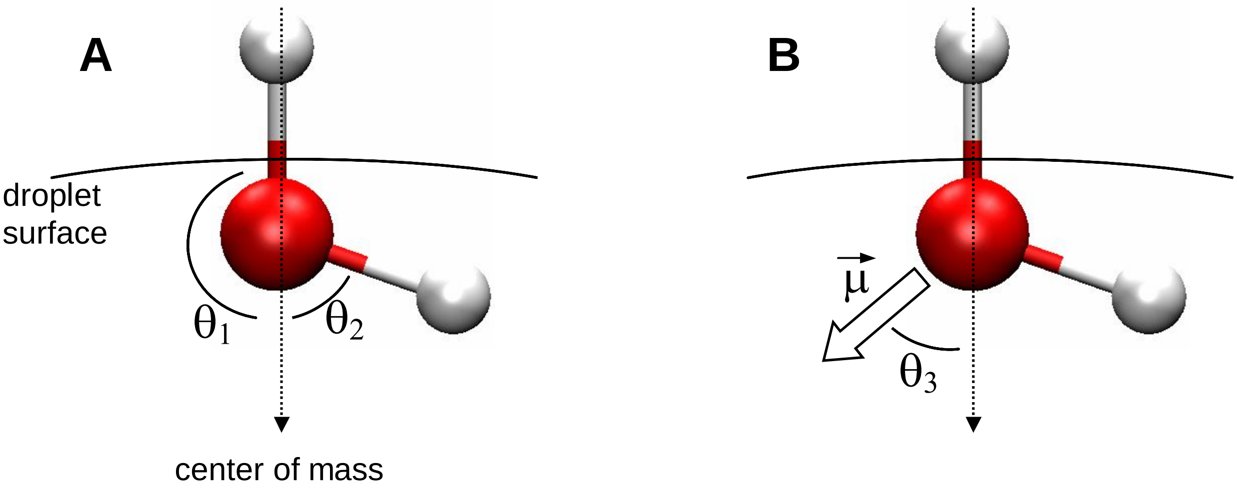

Figure 2.8. Depiction of angles used to describe the orientation of water molecules relative to the inward pointing normal vector (dotted arrow). (A) O-H angles θ_1 and θ_2; (B) angle θ_3 of the dipole moment $\vec{\mu}$. The orientation of the H_2O molecule shown here approximately illustrates the preferred values of the three angles within the outermost droplet layer.

phenomenon is somewhat model-dependent, and the SPC/E framework used here was found to yield results similar to several other water models [91]. Clearly, charged solutes such as H^+ and Na^+ will interact with an electrostatic potential gradient at the surface. To gain additional insights into this effect we will now examine the orientation of water molecules within the nanodroplet in more detail.

2.3.4 O-H and Dipole Moment Orientations

Figure 2.8 defines the angles used to describe the orientation of H_2O molecules relative to the vector pointing to the nanodroplet center of mass. Angles for the two O-H axes of each water molecule (θ_1 and θ_2, Figure 2.8A) were tallied into the same histogram. The dipole moment vector $\vec{\mu}$ lies in the plane defined by the H-O-H atoms, and its orientation is described by the angle θ_3 (Figure 2.8B).

For the purpose of data analysis the nanodroplets were divided into six layers with a thickness of 5 Å, and individual water molecules were assigned to these layers on the basis of their oxygen positions. Angular distribution functions plotted *vs.* cos(θ) [7, 92, 93] are depicted in Figure 2.9 for each of the layers. The three inner layers are characterized by distributions that are relatively flat, indicating that solvent molecules in this range adopt random orientations similar to bulk water (Figure 2.9A-C). In contrast, ordering of water molecules in the vicinity of the droplet surface is apparent for radial values greater than 15 Å. Non-random features are most pronounced for the outermost layer (Figure 2.9F). The O-H angular distribution in this panel has a sharp peak at cos(θ) = -1 (equivalent to θ = 180°), which corresponds to a preferred orientation where one of

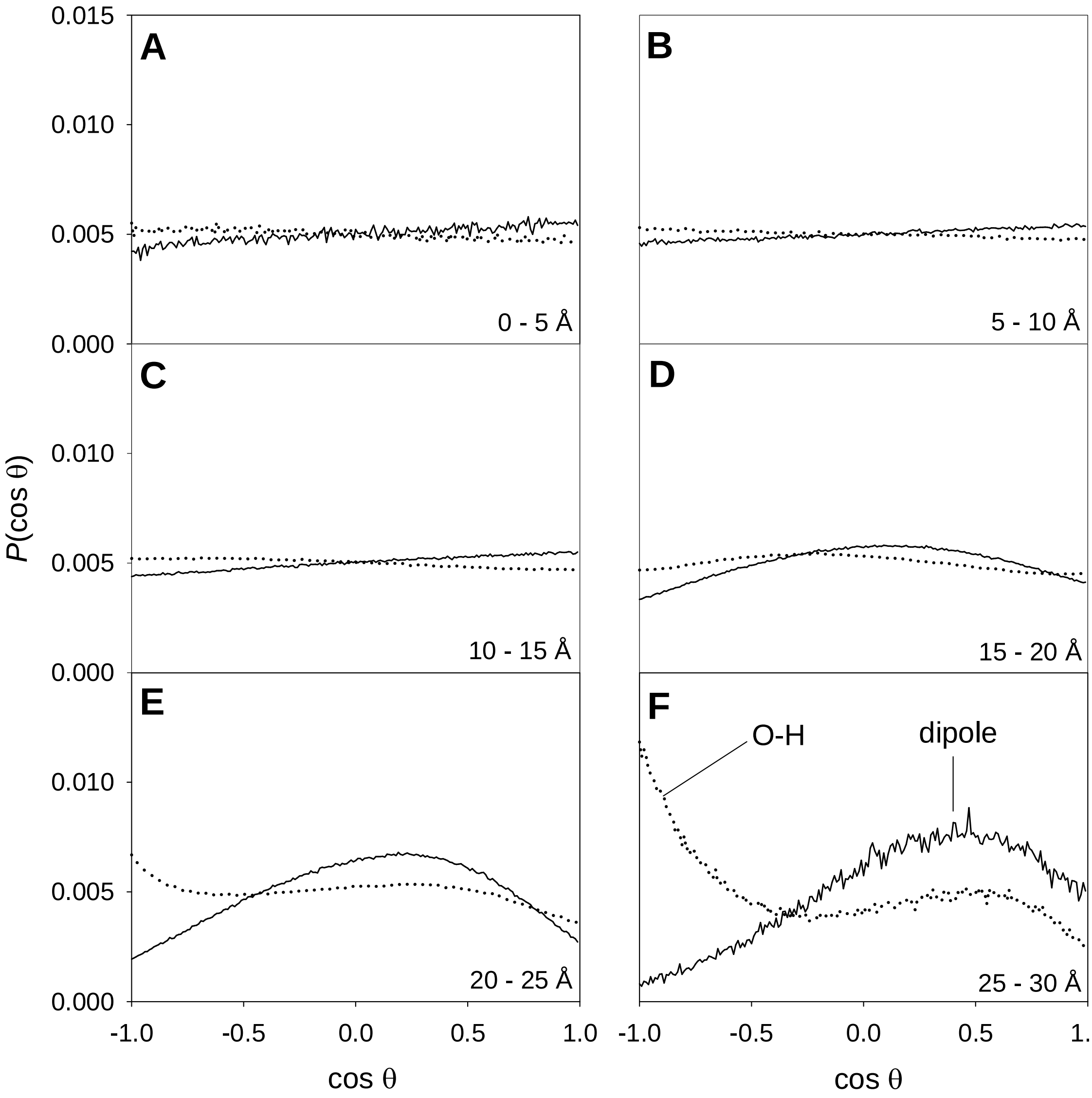

Figure 2.9. Distribution functions for the orientation of O-H angles (dotted lines, defined in Figure 2.8A), and dipole moment angles (solid lines, defined in Figure 2.8B). (A) - (F) represent concentric droplet layers, with radial boundaries as indicated in each panel. The distributions shown are for the same simulation data as those in Figure 2.7.

the hydrogen atoms is pointing straight into the vacuum environment (illustrated in Figure 2.8A). The dipole moment angular distribution in the outermost surface layer exhibits a broad maximum around $\cos(\theta) = 0.4$, which corresponds to $\theta \approx 66°$ (Figure 2.8B). The data in Figure 2.9 were obtained for nanodroplets carrying ten mobile protons, but virtually identical results (not shown) were found in simulations on uncharged water clusters. The preferential H_2O orientation at the droplet surface with one hydrogen "sticking out" reflects the tendency of water molecules to sacrifice one bonding interaction to maximize the total interactions with other solvent molecules [93, 94]. These findings are in line with earlier simulations on smaller clusters [93], computational studies on slabs [95], as well as results of sum frequency generation [96-99] and infrared spectroscopy [4], all of which confirm the presence of dangling O-H groups with the hydrogen pointing into the vapor phase.

2.3.5 Electrostatic Energy Landscape

We will now return to the reasons underlying the H^+ distribution within the nanodroplet, where proton trajectories frequently cross through the droplet interior instead of being confined to the surface (Figure 2.7A, dashed line). From the preceding section we know that water dipole moments $\vec{\mu}$ on the surface tend to orient themselves such that a radial vector component of roughly $\cos(66°) \times |\vec{\mu}| = 0.4 \times |\vec{\mu}|$ points towards the droplet center. The combination of all these surface dipole contributions leads to an electrostatic energy landscape with a deep minimum in the droplet center. This is demonstrated in Figure 2.10A, which shows a two-dimensional representation of the

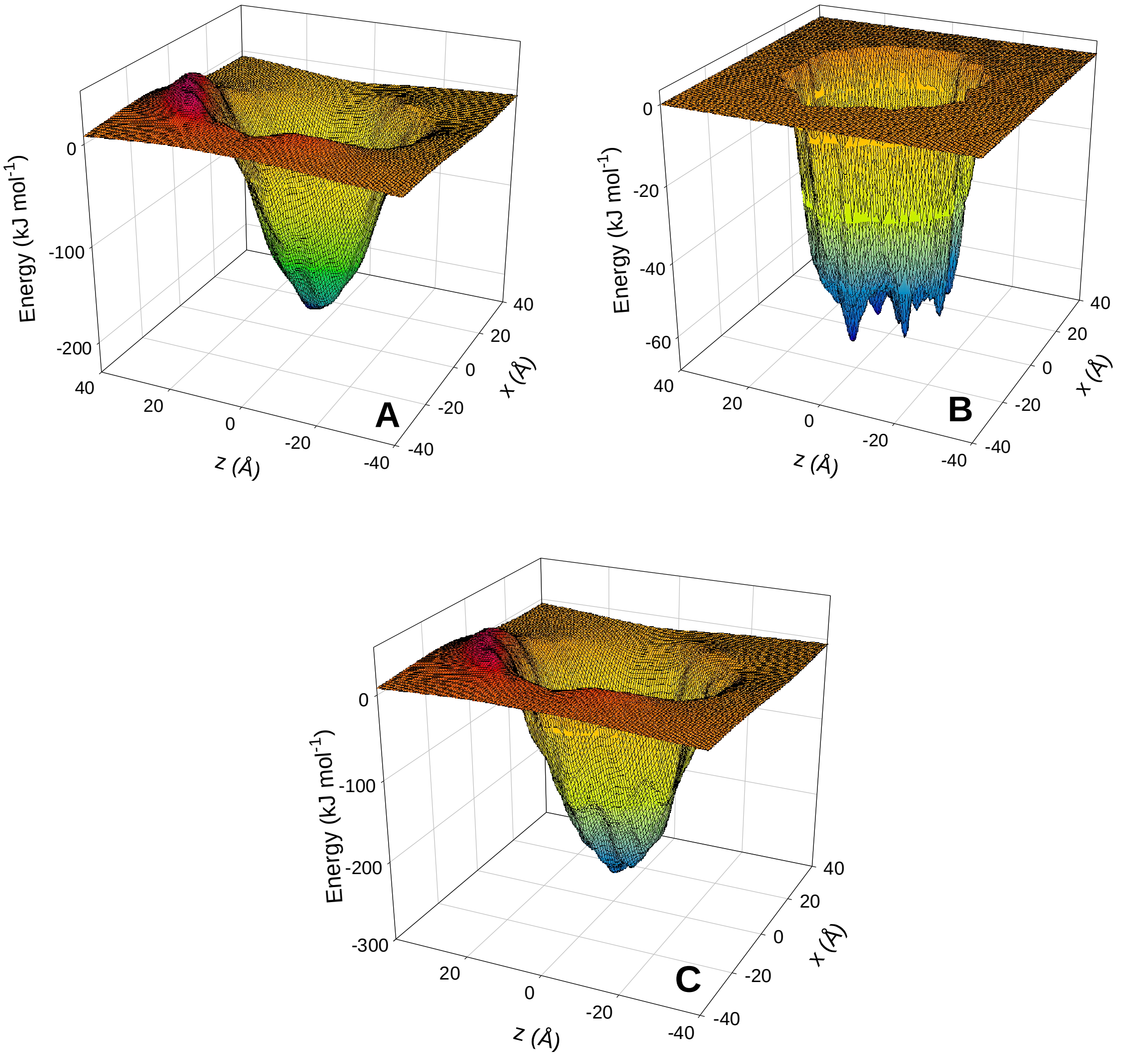

Figure 2.10. Potential energy scans through the central *xz* plane of a nanodroplet consisting of 1248 water molecules (protons removed), for one selected time point. (A) Total electrostatic ($U^{PC}1$) contributions experienced by a single proton. (B) Total trapping potential (T) contributions experienced by a single proton. (C) Overall energy landscape (sum of A and B).

combined $U^{PC}1$ contributions experienced by a single proton in the *xz* plane of a droplet at $y = 0$. Note that for this energy profile all other protons were removed from the cluster. Figure 2.10A represents just one random time point, but qualitatively similar data were obtained for other simulation times. The $U^{PC}1$ landscape reveals small positive features around the circumference of the nanodroplet which originate from dangling hydrogens. More important is the major energy minimum in the droplet center with a depth on the order of -200 kJ mol^{-1}. Clearly, such a funnel-shaped landscape provides a strong incentive for protons to move away from the droplet surface and venture into the interior. Separate MD runs (not shown) confirmed that this tendency is most pronounced for droplets containing a single excess proton, i.e., under conditions where mutual repulsion among charge carriers is absent. Potential energy scans similar to that in Figure 2.10A have previously been obtained for other water models using the standard Coulomb potential (Equation 2.5) [100]. This reflects the fact that the electrostatic energy landscape is dominated by long-range effects, which are identical in the r^{-1} and $U^{PC}1$ cases (Figure 2.2). Accordingly, a pull towards the droplet interior will occur not only for the mobile protons used in our model (Figure 2.7A), but for *any* cationic species (such as Na^+, Figure 2.7B).

Figure 2.10B illustrates the contributions of the proton trapping potential (*T*, Equation 2.4), which exhibits numerous local minima representing oxygen atoms. The overall energy landscape experienced by a mobile proton is given by the sum of the $U^{PC}1$ and *T* profiles (Figure 2.10C). Again, we note that the exact shapes of the landscapes change with time as a result of the internal droplet dynamics.

Overall, the H^+ and Na^+ radial distributions in Figures 2.7 reflect an interplay of several factors. When treating both solvent and charge within simple continuum models, Coulombic repulsion would be expected to induce the formation of a thin charged surface layer, analogous to the behavior seen for macroscopic metal conductors [18, 77, 78, 81]. For example, the energy released upon expanding a spherical layer with a total charge of ten protons from a radius of 14 to 21 Å is on the order of 160 kJ mol^{-1} per proton. On the other hand, dielectric considerations for discrete charges on a continuum conductor suggest that ions should move away from the droplet surface and into the bulk [13, 43]. At the molecular level, solvation of charged species in the outermost solvent layers is sub-optimal due to the decreasing H_2O density. In addition, the orientation of water molecules at the droplet surface (Figure 2.9F) generates a potential gradient, providing an electrostatic force that pulls positive charge carriers towards the droplet interior (Figure 2.10A). As a result of these contributions, positive charge carriers in our MD simulations are not confined to the droplet surface but preferentially occupy intermediate radial positions. This finding is consistent with earlier studies on metal cations, [13, 57] but it is contrary to the assumptions made in most ESI studies [18, 19, 32, 34, 77-80].

2.3.6 Comparison of Proton Behavior with Earlier Investigations

The current work predicts preferential positioning at intermediate radial locations for Na^+ as well as for protons. This finding is in line with the Stokes diffusion simulations of Znamenskiy et al. [48] Interestingly, other computational investigations suggest a possible enrichment of protons in the outermost layers of the water/vacuum interface for slabs [57, 95] and nanodroplets [101]. It has been proposed that proton surface affinity could arise from an amphiphilic character of H_3O^+ [12, 57, 95, 101], resulting from the inability of oxygen in such an Eigen-type hydronium ion to act as H-bond acceptor [72]. Considering the sparse overall hydration of ions at the liquid/vacuum interface, the prediction of a high surface proton density in those studies [12, 57, 72, 95, 101] is surprising. Specifically, a configuration where an H_3O^+ moiety sits "above" the surface with its hydrogen tripod pointing towards the bulk [95] should not be conducive to H-bond formation with an interface that is dominated by dangling O-H groups [4, 93-99]. In addition, the proposed amphiphilic character and associated surface affinity would be expected to apply for Eigen structures only, not for Zundel-type ($H_2O...H^+...OH_2$) arrangements which represent another common hydration motif. [12, 70, 102, 103] Suggestions have been made that the surface affinity of H_3O^+ is most pronounced for very small clusters (e.g. dozens of waters), and that the magnitude of this effect should decrease for larger nanodroplets [70]. Also, it has been demonstrated that the extent to which computational studies predict a surface affinity for protons in solution is highly model dependent [104]. Recent work employing second harmonic [105] and sum frequency generation spectroscopy [57] bolster the notion of proton enrichment at water surfaces, but these results are in stark contrast to the conclusions derived from earlier macroscopic experiments [106]. It will be interesting to see if future studies can provide additional support for the enrichment of protons at surfaces, or whether the H^+ distribution in ESI droplets resembles that of small inorganic cations [13, 57] as predicted in this work and elsewhere [48].

2.4 Conclusions

In this study, we have established a simple framework for MD simulations of multiply protonated water nanodroplets. Protons are described as highly mobile point charges. The $U^{PC}1$ parameter set provides a H^+ diffusion coefficient within nanodroplets which matches that in bulk solution. Nonetheless, it is clear that any computational model has its limitations [68]. The advantage of the framework developed here is its ability to describe proton mobility at minimal computational cost. On the other hand, our model cannot address more subtle features such as the mechanism of Grotthus diffusion, H^+ solvation in terms of Zundel or Eigen structures [53, 102], or the extent to which hydrated protons exhibit amphiphilic character [12, 57, 95, 101]. Nonetheless, approaches of the type used here should be well suited for simulating the final stages of ESI in a semi-quantitative manner, including solvent evaporation, droplet fission, and release of analyte ions into the gas phase.

It is well documented that the charge states of gas-phase ions produced by ESI can be dramatically different from the corresponding analyte charge states in bulk solution [107, 108]. At present it is unclear when this transition occurs. Obviously, one important factor for understanding the mechanism of this process is the spatial distribution of excess charge carriers (e.g., protons, metal cations, or ammonium ions) within the droplet. The concept of a thin surface charge layer is widely used in the ESI-MS literature [18, 19, 32, 34, 77-80]. The current study suggests that a critical re-evaluation of this paradigm may be in order, at least for droplets with radii on the order of a few nanometers. It seems likely that the effects of surface water ordering on the internal charge distribution become less pronounced for larger droplets. Thus, a continuum treatment may be adequate for micrometer-sized droplets encountered during the initial stages of ESI.

2.5 References

1. Chaplin, M., *Do we underestimate the importance of water in cell biology?* Nat. Rev. Mol. Cell Bio., 2006. **7**: p. 861-866.

2. Ball, P., *Water as an Active Constituent in Cell Biology.* Chem. Rev., 2008. **108**: p. 74-108.

3. Zweir, T.S., *The structure of protonated water clusters.* Science, 2004. **304**: p. 1119-1120.

4. Shin, J.-W., N.I. Hammer, E.G. Diken, M.A. Johnson, R.S. Walters, T.D. Jaeger, M.A. Duncan, R.A. Christie, and K.D. Jordan, *Infrared Signature of Structures Associated with the H+(H2O)n (n = 6 to 27) Clusters.* Science, 2004. **304**: p. 1137-1140.

5. Stone, A.J., *Intermolecular Potentials.* Science, 2008. **321**: p. 787-789.

6. Klein, M.L. and W. Shinoda, *Large-Scale Molecular Dynamics Simulations of Self-Assembling Systems.* Science, 2008. **321**: p. 798-800.

7. Rossky, P.J. and M. Karplus, *Solvation. A Molecular Dynamics Study of a Dipeptide in Water.* J. Am. Chem. Soc., 1979. **101**: p. 1913-1937.

8. Swanson, J.M.J., C.M. Maupin, H. Chen, M.K. Petersen, J. Xu, Y. Wu, and G.A. Voth, *Proton solvation and transport in aqueous and biomolecular systems: Insights from computer simulations.* J. Phys. Chem. B, 2007. **111**: p. 4300-4314.

9. Marx, D., M.E. Tuckerman, J. Hutter, and M. Parrinello, *The nature of the hydrated excess proton in water.* Nature, 1999. **397**: p. 601-604.

10. Lee, H.M., S.B. Suh, J.Y. Lee, P. Tarakeshwar, and K.S. Kim, *Structures, energies, vibrational spectra and electronic properties of water monomer to decamer.* J. Chem. Phys., 2000. **112**: p. 9759-9772.

11. Lee, H.M., S.B. Suh, and K.S. Kim, *Structures, energies and vibrational spectra of water undecamer and dodecamer: An ab initio study.* J. Chem. Phys., 2001. **114**: p. 10749-10756.

12. Wang, F., S. Izvekov, and G.A. Voth, *Unusual "amphiphilic" association of hydrated protons in strong acid solution.* J. Am. Chem. Soc., 2008. **130**: p. 3120-3126.

13. Garrett, B.C., *Ions at the Air/Water Interface.* Science, 2004. **303**: p. 1146-1147.

14. Bruins, A.P., T.R. Covey, and J.D. Henion, *Ion Spray Interface for Combined Liquid Chromatography/Atmospheric Pressure Ionization Mass Spectrometry.* Anal. Chem., 1987. **59**: p. 2642-2646.

15. Fenn, J.B., *Electrospray Wings for Molecular Elephants (Nobel Lecture).* Angew. Chem. Int. Ed., 2003. **42**: p. 3871-3894.

16. Kaltashov, I.A. and S.J. Eyles, *Mass Spectrometry in Biophysics*. 2005, Hoboken, NJ: John Wiley and Sons, Inc.

17. Nemes, P., I. Marginean, and A. Vertes, *Spraying Mode Effect on Droplet Formation and Ion Chemistry in Electrosprays.* Anal. Chem., 2007. **79**: p. 3105-3116.

18. Iavarone, A.T. and E.R. Williams, *Mechanism of Charging and Supercharging Molecules in Electrospray Ionization.* J. Am. Chem. Soc., 2003. **125**: p. 2319-2327.

19. Fenn, J.B., *Ion Formation from Charged Droplets: Roles of Geometry, Energy, and Time.* J. Am. Soc. Mass Spectrom., 1993. **4**: p. 524-535.

20. Van Berkel, G.J. and V. Kertesz, *Electrochemistry/spray Ion Source.* Anal. Chem., 2007. **79**: p. 5511-5520.

21. Konermann, L., E.A. Silva, and O.F. Sogbein, *Electrochemically Induced pH Changes Resulting in Protein Unfolding in the Ion Source of an Electrospray Mass Spectrometer.* Anal. Chem., 2001. **73**: p. 4836-4844.

22. Felitsyn, N., M. Peschke, and P. Kebarle, *Origin and number of charges observed on multiply-protonated native proteins produced by ESI.* Int. J. Mass Spectrom. Ion Proc., 2002. **219**: p. 39-62.

23. Verkerk, U.H. and P. Kebarle, *Ion-Ion and Ion-Molecule Reactions at the Surface of Proteins Produced by Nanospray. Information on the Number of Acidic Residues and Control of the Number of Ionized Acidic and Basic Residues.* J. Am. Soc. Mass Spectrom., 2005. **16**: p. 1325-1341.

24. Kebarle, P. and M. Peschke, *On the Mechanisms by which the charged droplets produced by electrospray lead to gas phase ions.* Anal. Chim. Acta, 2000. **406**: p. 11-35.

25. Rayleigh, L., *On the Equilibrium of Liquid Conducting Masses charged with Electricity.* Phil. Mag., 1882. **14**: p. 184-186.

26. Kebarle, P. and L. Tang, *From ions in solution to ions in the gas phase: The mechanism of electrospray mass spectrometry.* Anal. Chem., 1993. **65**: p. 972A-986A.

27. Gu, W., P.E. Heil, H. Choi, and K. Kim, *Comprehensive model for fine Coulomb fission of liquid droplets charged to Rayleigh limit.* Appl. Phys. Lett., 2007. **91**: p. 064104.

28. Gomez, A. and K. Tang, *Charge and fission of droplets in electrostatic sprays.* Phys. Fluids, 1994. **6**: p. 404-414.

29. Duft, D., T. Achtzehn, R. Muller, B.A. Huber, and T. Leisner, *Coulomb fission: Rayleigh jets from levitated microdroplets.* Nature, 2003. **421**: p. 128.

30. Li, D., M. Marquez, and Y. Xia, *Capturing electrified nanodroplets under Rayleigh instability by coupling electrospray with a sol–gel reaction.* Chem. Phys. Lett., 2007. **445**: p. 271-275.

31. Konermann, L., *A Simple Model for the Disintegration of Highly Charged Solvent Droplets during Electrospray Ionization.* J. Am. Soc. Mass Spectrom., 2009. **20**: p. 496-506.

32. Hogan, C.J. and P. Biswas, *Monte Carlo Simulation of Macromolecular Ionization by Nanoelectrospray.* J. Am. Soc. Mass Spectrom., 2008. **19**: p. 1098-1107.

33. Dole, M., L.L. Mack, R.L. Hines, R.C. Mobley, L.D. Ferguson, and M.B. Alice, *Molecular beams of macroions.* J. Chem. Phys., 1968. **49**: p. 2240-2249.

34. Iribarne, J.V. and B.A. Thomson, *On the evaporation of small ions from charged droplets.* J. Chem. Phys., 1975. **64**: p. 2287-2294.

35. Gamero-Castaño, M. and F. de la Mora, *Kinetics of small ion evaporation from the charge and mass distribution of multiply charged clusters in electrosprays.* J. Mass Spectrom., 2000. **35**: p. 790-803.

36. de la Mora, F.J., *Electrospray Ionization of large multiply charged species proceeds via Dole's charged residue mechanism.* Anal. Chim. Acta, 2000. **406**: p. 93-104.

37. Nesatyy, V.J. and M.J.-F. Suter, *On the conformation-dependent neutralization theory and charging of individual proteins and their non-covalent complexes in the gas phase.* J. Mass Spectrom., 2004. **39**: p. 93-97.

38. Kaltashov, I.A. and A. Mohimen, *Estimates of Protein Surface Area in Solution by Electrospray Ionization Mass Spectrometry.* Anal. Chem., 2005. **77**: p. 5370-5379.

39. Samalikova, M. and R. Grandori, *Protein Charge-State Distributions in Electrospray-Ionization Mass Spectrometry Do Not Appear To Be Limited by the Surface Tension of the Solvent.* J. Am. Chem. Soc., 2003. **125**: p. 13352-13353.

40. Peters, J.M.H., *Rayleigh's electrified water drops.* Eur. J. Phys., 1980. **1**: p. 143-146.

41. Consta, S., K.R. Mainer, and W. Novak, *Fragmentation mechanisms of aqueous clusters charged with ions.* J. Chem. Phys., 2003. **119**: p. 10125-10132.

42. Townsend, R.M. and S.A. Rice, *Molecular dynamics studies of the liquid–vapor interface of water.* J. Chem. Phys., 1991. **94**: p. 2207-2218.

43. Jungwirth, P. and D.J. Tobias, *Specfic ion effects at the air/water interface.* Chem. Rev., 2006. **106**: p. 1259-1281.

44. Nguyen, S. and J.B. Fenn, *Gas-phase ions of solute species from charged droplets of solutions.* Proc. Natl. Acad. Sci. U.S.A., 2007. **104**: p. 1111-1117.

45. Hogan, C.J., J.A. Carroll, H.W. Rohrs, P. Biswas, and M.L. Gross, *Charge Carrier Field Emission Determines the Number of Charges on Native State Proteins in Electrospray Ionization.* J. Am. Chem. Soc., 2008. **130**: p. 6929-6927.

46. Consta, S., *Fragmentation reactions of charged aqueous clusters.* J. Mol. Struct. (Theochem), 2002. **591**: p. 131-140.

47. Ichiki, K. and S. Consta, *Disintegration Mechanisms of Charged Aqueous Nanodroplets Studied by Simulations and Analytical Models.* J. Phys. Chem. B, 2006. **110**: p. 19168-19175.

48. Znamenskiy, V., I. Marginean, and A. Vertes, *Solvated Ion Evaporation from Charged Water Droplets.* J. Phys. Chem. A, 2003. **107**: p. 7406-7412.

49. Marginean, I., V. Znamenskiy, and A. Vertes, *Charge Reduction in Electrosprays: Slender Nanojets as Intermediates.* J. Phys. Chem. B, 2006. **110**: p. 6397-6404.

50. Glietenberg, D., A. Kutschker, and M. v. Stackelberg, *Der Diffusionskoeffizient des Protons in waessrigen Loesungen einiger Salze.* Ber. Bunsenges., 1968. **72**: p. 562-565.

51. Heberle, J., *A Local Area Network of Protonated Water Molecules.* Biophys. J., 2004. **87**: p. 2105-2106.

52. Schifino, J. and R.M. Olegario, *Self-diffusion Coefficients of Na+ in Water-methanol Mixtures.* J. Braz. Chem. Soc., 1993. **4**: p. 102-107.

53. Marx, D., *Proton transfer 200 years after von Grotthuss: Insights from Ab initio simulations.* ChemPhysChem., 2006. **7**: p. 1848-1870.

54. Cukierman, S., *Et tu, Grotthuss! and other unfinished stories.* Biochimica et Biophysica Acta, 2006. **1757**: p. 876-885.

55. Iyengar, S.S., C.J. Burnham, M.K. Petersen, and G.A. Voth, *Modeling condensed-phase chemistry through molecular dynamics simulation.* Comput. Chem., 2003: p. 31-35.

56. Schmid, R.G. and J. Brickmann, *Molecular Dynamics Simulation of the Proton Transport in Water.* Ber. Bunsenges. Phys. Chem., 1997. **101**: p. 1816-1827.

57. Mucha, M., T. Frigato, L.M. Levering, H.C. Allen, D.J. Tobias, L.X. Dang, and P. Jungwirth, *Unified molecular picture of the surfaces of aqueous acid, base and salt solutions.* J. Phys. Chem. B, 2005. **109**: p. 7617-7623.

58. Konermann, L., *A Minimalist Model for Exploring Conformational Effects on the Electrospray Charge State Distribution of Proteins.* J. Phys. Chem. B, 2007. **111**: p. 6534-6543.

59. Berendsen, H.J.C., J.R. Grigera, and T.P. Straatsma, *The missing term in effective pair potentials.* J. Phys. Chem., 1987. **91**: p. 6269-6271.

60. Verlet, L., *Computer "Experiments" on Classical Fluids. I. Thermodynamical Properties of Lennard-Jones Molecules.* Phys. Rev., 1967. **159**: p. 98-103.

61. Frenkel, D. and B. Smit, *Understanding Molecular Simulations: From Algorithms To Applications*. 1996, San Diego: Academic Press.

62. Nose, S., *A molecular dynamics method for simulations in the canonical ensemble.* Mol. Phys., 1984. **52**: p. 255-268.

63. Hoover, W.G., *Canonical dynamics: Equilibrium phase-space distributions.* Phys. Rev. A, 1985. **31**: p. 1695-1697.

64. Allen, M.P. and D.J. Tildesley, *Computer Simulation of Liquids*. 1987: Clarendon Press.

65. Forester, T.R. and W. Smith, *SHAKE, Rattle and Roll: Efficient Constraint Algorithms for Linked Rigid Bodies.* J. Comput. Chem., 1998. **19**: p. 102-111.

66. Lill, M.A. and V. Helms, *Molecular dynamics simulation of proton transport with quantum mechanically derived proton hopping rates (Q-HOP MD).* J. Chem. Phys., 2001. **115**: p. 7993-8005.

67. Consta, S. and R. Kapral, *Dynamics of proton transfer in mesoscopic clusters.* J. Chem. Phys., 1996. **104**: p. 4581-4590.

68. Billeter, S.R. and W.F. van Gunsteren, *Protonizable Water Model for Quantum Dynamical Symulations.* J. Phys. Chem. A, 1998. **102**: p. 4669-4678.

69. Morrone, J.A., K.E. Haslinger, and M.E. Tuckerman, *Ab initio molecular dynamics simulations of the structure and proton transport dynamics of methanol-water solutions.* J. Phys. Chem. B, 2006. **110**: p. 3712-3720.

70. Singh, N.J., M. Park, S.K. Min, S.B. Suh, and K.S. Kim, *Magic and antimagic protonated water clusters: Exotic structures with unusual dynamic effects.* Angew. Chem. Int. Ed., 2006. **45**: p. 3795-3800.

71. Car, R. and M. Parrinello, *Unified approach for molecular dynamics and density-functional theory.* Phys. Rev. Lett., 1985. **55**: p. 2471-2474.

72. Markovitch, O. and N. Agmon, *Structure and Energetics of the Hydronium Hydration Shells.* J. Phys. Chem. A, 2007. **111**: p. 2253–2256.

73. Müser, M.H. and B.J. Berne, *Circumventing the pathological behavior of path-integral Monte Carlo for systems with Coulomb potentials.* J. Chem. Phys., 1997. **107**: p. 571-575.

74. Koneshan, S., J.C. Rasaiah, R.M. Lynden-Bell, and S.H. Lee, *Solvent structure, dynamics and ion mobility in aqueous solutions at 25 C.* J. Phys. Chem. B, 1998. **102**: p. 4193-4204.

75. Dill, K.A. and H.S. Chan, *From Levinthal to pathways to funnels.* Nat. Struct. Biol., 1997. **4**: p. 10-19.

76. Plotkin, S.S. and P.G. Wolynes, *Buffed energy landscapes: Another solution to the kinetic paradoxes of protein folding.* Proc. Natl. Acad. Sci. U.S.A., 2003. **100**: p. 4417-4422.

77. Fenn, J.B., J. Rosell, and C.K. Meng, *In Electrospray Ionization, How Much Pull Does an Ion Need to Escape Its Droplet Prison.* J. Am. Soc. Mass Spectrom., 1997. **8**: p. 1147-1157.

78. Echt, O. and T.D. Märk, *Multiply Charged Clusters*, in *Clusters of Atoms and Molecules II*, H. Haberland, Editor. 1994, Springer: Berlin Heidelberg New York. p. 183-220.

79. Bruins, A.P., *Mechanistic aspects of electrospray ionization.* J. Chromatogr. A, 1998. **794**: p. 345-357.

80. Hogan, C.J., J.A. Carroll, H.W. Rohrs, P. Biswas, and M.L. Gross, *Combined Charged Residue-Field Emission Model of Macromolecular Electrospray Ionization.* Anal. Chem., 2009. **81**: p. 369-377.

81. Halliday, D., R. Resnick, and K.S. Krane, *Physics.* 4 ed. 1992, New York: Wiley.

82. Essex, J.W. and W.L. Jorgensen, *An empirical boundary potential for water droplet simulations.* J. Comput. Chem., 1995. **16**: p. 951-972.

83. Hore, D.K., D.S. Walker, and G.L. Richmond, *Water at hydrophobic surfaces: When weaker is better.* J. Am. Chem. Soc., 2008. **130**: p. 1800-1801.

84. Walker, D.S., D.K. Hore, and G.L. Richmond, *Understanding the population, coordination and orientation of water species contributing to the nonlinear optical spectroscopy of the vaper-water interface through molecular dynamics simulations.* J. Phys. Chem. B, 2006. **110**: p. 20451-20459.

85. Despa, F. and R.S. Berry, *Hydrophobe-Water Interactions: Methane as a Model.* Biophys. J., 2008. **95**: p. 4241-4245.

86. Wang, L. and J. Hermans, *The dielectric properties of simulated water droplets.* Mol. Simulat., 1996. **17**: p. 67-74.

87. Paluch, M., *Electrical properties of free surface of water and aqueous solutions.* Adv. Colloid Interfac., 2000. **84**: p. 27-45.

88. Yu, J.Y. and M.S. Jhon, *Molecular dynamics study on the properties of water clusters.* J. Colloid Interf. Sci., 1991. **147**: p. 443-449.

89. Sokhan, V.P. and D.J. Tildesley, *The free surface of water: molecular orientation, surface potential and nonlinear susceptibility.* Mol. Phys., 1997. **92**: p. 625-640.

90. Parfenyuk, V.I., *Surface Potential at the Gas–Aqueous Solution Interface.* Colloid Journal, 2002. **64**: p. 588-595.

91. Kathmann, S.M., I.-F.W. Kuo, and C.J. Mundy, *Electronic Effects on the Surface Potential at the Vapor-Liquid Interface of Water.* J. Am. Chem. Soc., 2008. **130**: p. 16556–16561.

92. Brodskaya, E.N., J.C. Eriksson, A. Laaksonen, and A.I. Rusanov, *Local structure and work of formation of water clusters studied by molecular dynamics simulations.* J. Colloid Interf. Sci., 1996. **180**: p. 86-97.

93. Belch, A.C. and M. Berkowitz, *Molecular dynamics simulations of TIPS2 water restricted by a spherical hydrophobic boundary.* Chem. Phys. Lett., 1985. **113**: p. 278-282.

94. Lee, C.-Y., J.A. McCammon, and P.J. Rossky, *The structure of liquid water at an extended hydrophobic surface.* J. Chem. Phys., 1984. **80**: p. 4448-4455.

95. Petersen, M.K., S.S. Iyengar, T.J.F. Day, and G.A. Voth, *The hydrated proton at the water liquid/vapor interface.* J. Phys. Chem. B, 2004. **108**: p. 14804-14806.

96. Miranda, P.B. and Y.R. Shen, *Liquid Interfaces: A Study by Sum-Frequency Vibrational Spectroscopy.* J. Phys. Chem. B, 1999. **103**: p. 3292-3307.

97. Perry, A., C. Neipert, B. Space, and P.B. Moore, *Theoretical modeling of interface specific vibrational spectroscopy: Methods and applications to aqueous interfaces.* Chem. Rev., 2006. **106**: p. 1234-1258.

98. Shen, Y.R. and V. Ostroverkhov, *Sum-frequency vibrational spectroscopy on water interfaces: Polar orientation of water molecules at interfaces.* Chem. Rev., 2006. **106**: p. 1140-1154.

99. Gopalakrishnan, S., D. Liu, H.C. Allen, M. Kuo, and M.J. Shultz, *Vibrational spectroscopic studies of aqueous interfaces: Salt, acids, bases and nanodrops.* Chem. Rev., 2006. **106**: p. 1155-1175.

100. Chang, T.-M. and L.X. Dang, *Recent advances in molecular simulations of ion solvation at liquid interfaces.* Chem. Rev., 2006. **106**: p. 1305-1322.

101. Iyengar, S.S., T.J.F. Day, and G.A. Voth, *On the amphiphilic behavior of the hydrated proton: an ab initio molecular dynamics study.* Int. J. Mass Spectrom., 2005. **241**: p. 197-204.

102. Ojamae, L., I. Shavitt, and S.J. Singer, *Potential models for simulations of the solvated proton in water.* J. Chem. Phys., 1998. **109**: p. 5547-5564.

103. Park, M., I. Shin, N.J. Singh, and K.S. Kim, *Eigen and zundel forms of smaller protonated water clusters: Structures and infrared spectra.* J. Phys. Chem. A, 2007. **111**: p. 10692-10702.

104. Dang, L.X., *Solvation of the hydronium ion at the water liquid/vapor interface.* J. Chem. Phys., 2003. **119**: p. 6351-6353.

105. Petersen, P.B. and R.J. Saykally, *Evidence for an enhanced hydronium concentration at the liquid water surface.* J. Phys. Chem. B, 2005. **109**: p. 7976-7980.

106. Petersen, P.B. and R.J. Saykally, *Is the liquid water surface basic or acidic? Macroscopic vs. molecular-scale investigations.* Chem. Phys. Lett., 2008. **458**: p. 255-261.

107. Wang, G. and R.B. Cole, *Disparity Between Solution-phase Equilibria and Charge State Distributions in Positive-ion Electrospray Mass Spectrometry.* Org. Mass Spectrom., 1994. **29**: p. 419-427.

108. Konermann, L. and D.J. Douglas, *Unfolding of Proteins Monitored by Electrospray Ionization Mass Spectrometry: A Comparison of Positive and Negative Ion Modes.* J. Am. Soc. Mass Spectrom., 1998. **9**: p. 1248-1254.

Chapter 3 – Surface Charge of Electrosprayed Water Nanodroplets: A Molecular Dynamics Study

3.1 Introduction

Electrospray ionization (ESI) mass spectrometry (MS) [1] is an analytical method that has found scientific and commercial applications in many areas [2-4]. The ESI process commences when a flow of analyte solution (e.g., the eluent from a chromatographic column) is passed through a metal capillary to which a positive potential of several kilovolts has been applied [5]. ESI-MS studies often employ mixtures of water and organic cosolvents, but purely aqueous solutions may be used as well [6]. The capillary outlet is separated from the ion sampling interface of the mass spectrometer by an atmospheric pressure gap. The interface is held at a potential close to ground, and it acts as counter electrode. The ensuing electric field leads to electrophoretic charge separation within the solution at the capillary tip. The liquid emanating from the capillary is drawn out into a Taylor cone that emits positively charged droplets. Excess charge on these droplets may be due to various cationic species, including Na^+, NH_4^+ and H^+ [7-9]. The described scenario applies to the commonly used positive ion ESI mode. It is also possible to produce droplets carrying excess anions, by applying a negative potential to the metal capillary [10].

The size of the droplets emitted from the Taylor cone is in the micrometer range. Subsequent solvent evaporation increases the charge density until the droplets become unstable at the Rayleigh limit where the net charge Q_R is given by [5, 11]

$$Q_R = 8\pi(\varepsilon_0 \gamma R^3)^{1/2} \tag{3.1}$$

where ε_0 is the vacuum permittivity, γ is the surface tension, and R is the droplet radius. Jet emission at the Rayleigh limit leads to the formation of smaller progeny droplets [12-15]. Following several evaporation/fission cycles the process ultimately yields nanometer-sized droplets that can release gas-phase analyte ions [5]. For ESI experiments that employ organic/aqueous mixtures, the water percentage of these nanodroplets can be greatly enhanced as a result of differential vapor pressures [16, 17]. The past few years have witnessed considerable progress in the general understanding of the ESI mechanism [5, 7, 18-20]. However, the final step that generates free analyte ions from highly charged nanodroplets remains enigmatic [21]. In addition to the classical theories of charged residue mechanism [22-24] *vs.* ion evaporation model [25, 26], alternative scenarios have been proposed [27].

A basic assumption of currently existing ESI models is that excess charge carriers are confined to a thin layer at the droplet surface [5, 24, 25, 27-30]. This view originates from simple electrostatic arguments for a conducting sphere, where a quasi-continuum description is used for both solvent and charge [31]. However, it remains an open question whether these arguments are applicable to charged nanodroplets. One concern is that placing charge carriers at a liquid/vapor interface should result in the loss of enthalpically favorable solvation interactions. Also, the Onsager-Samaras [32] image charge formalism predicts that ions will be repelled from a dielectric interface such as the one between an aqueous solution and the vapor phase [κ_e(water) $\approx$ 80, κ_e(vapor) $\approx$ 1] [33-35]. Indeed, molecular dynamics (MD) simulations [36-41] and surface tension measurements [42] reveal a depletion of small, non-polarizable ions (such as Na^+, K^+, and F$^-$) at the surface of planar water slabs. In contrast, anions with large electronic polarizabilities such as Br$^-$ and I$^-$ appear to accumulate at the surface [34, 38]. Recent computational studies predict a high surface affinity also for solvated protons [43], although experimental work does not necessarily support this notion [41]. Most previous investigations on the behavior of ions at interfaces have focused on planar systems carrying zero excess charge. Hence, the implications of those studies for ESI nanodroplets are not immediately clear [33]. A related issue that is not widely discussed in the ESI literature concerns the occurrence of solvent ordering in the droplet periphery (Chapter 2), a factor that could have implications for analyte interactions with the surface [19, 44]. Sum frequency generation (SFG) spectroscopy and MD studies have shown that the properties of planar water/vapor interfaces resemble those at a hydrophobic surface [41, 45-48].

Overall, it appears that the widely used model of highly charged nanodroplets as homogenous spheres with a thin layer of surface charge [5, 24, 25, 27-30] needs to be carefully scrutinized, if improved models of the final ESI steps are to be developed. Experimental investigations on the behavior of nanodroplets are not straightforward, but recent MD studies have begun to reveal interesting aspects of their properties [15, 49-54].

An earlier study from our laboratory (Chapter 2) employed the SPC/E water model [55] for MD simulations on water droplets close to the Rayleigh limit. The SPC/E framework was extended to include excess protons as highly mobile charge carriers. Protons were found to reside at radial positions around 2/3 R, i.e., not at the surface. The observed behavior was tentatively attributed to an interplay of Coulomb repulsion, solvation effects [36], surface water ordering [41, 46-48], and Onsager-Samaras depletion

[32]. However, solvated protons likely exhibit the most complex behavior of all ESI charge carriers. Therefore the predictive power of simple H^+ models is limited (Chapter 2). In particular, these models cannot adequately account for Zundel or Eigen-type solvation [56], Grotthus migration [57, 58], and possible amphiphilic effects that might enhance surface affinity [43]. Hence, many fundamental aspects of ESI nanodroplets will be more readily accessible by focusing on charge carriers other than protons.

The current work employs MD simulations for exploring the properties of nanometer-sized water droplets that are charged with atomic ions. We specifically focus on the behavior of Na^+. This choice is motivated by the fact that Na^+-containing droplets play an important role for mechanistic investigations on the ESI process [5, 25, 49]. Moreover, electronic polarization effects have been shown to be negligible for the surface affinity of Na^+, a fact that greatly simplifies the data interpretation of this work [36-42, 54]. We find that all Na^+ ions adopt positions in the nanodroplet interior. It is tempting to rush to the conclusion that this behavior violates the commonly accepted surface charge paradigm. However, closer inspection reveals an interesting mechanism that amounts to dipole-mediated charge transfer from the droplet interior to the surface. As a result, excess charge *is* located on the surface the droplets, as expected on the basis of simple electrostatic arguments. At the same time, the actual charge carriers (ions) are *not* located on the surface, but buried in the interior where they are extensively solvated. This intriguing effect adds a new perspective to the ongoing debate regarding the validity of the surface charge paradigm.

3.2 Methods

MD simulations were carried out based on C++ code developed in-house (Chapter 2). The temporal evolution of droplets consisting of 1248 SPC/E water molecules [55] in a vacuum environment was determined by integrating the classical equations of motion using the Verlet algorithm [59, 60] with a time step of 2 fs. The water geometry is defined by a O-H bond distance of 1.0 Å and a H-O-H angle of 109.47° [55]. The system was initially subjected to Nose-Hoover thermalization [61, 62] at 320 K for 80 ps. The simulation was then switched to constant energy MD (at $T \approx 320$ K) for typically 1 ns, during which particle coordinates were extracted every 0.4 ps for analysis. Lennard Jones (LJ) parameters for water were $\sigma_{OO} = 3.166$ Å and $\varepsilon_{OO} = 0.6502$ kJ mol^{-1}, with charges $q_O = -0.8476\ e$ and $q_H = 0.4238\ e$ [55]. Na$^+$ ions where modeled using $\sigma_{NaNa} = 2.586$ Å, $\varepsilon_{NaNa} = 0.4184$ kJ mol^{-1}, and $q_{Na} = +1.0\ e$ [63]. The mixing of LJ parameters for Na-O interactions was done according the Lorentz-Berthlot rules [64], i.e., $\sigma_{ij} = \frac{1}{2}(\sigma_{ii} + \sigma_{jj})$ and $\varepsilon_{ij} = \sqrt{\varepsilon_{ii}\varepsilon_{jj}}$, resulting in $\sigma_{NaO} = 2.876$ Å and $\varepsilon_{NaO} = 0.5216$ kJ mol^{-1}. Interactions between ions and SPC/E hydrogens were modeled purely based on the Coulomb potential. LJ potentials were truncated at 9.5 Å but no cutoffs were used for Coulomb interactions. Electronic polarization effects were not considered in this work. Radial distributions represent histograms that are plotted vs. the distance r from the droplet center of mass, corrected for the $4\pi r^2$ surface area of individual bins to account for the spherical geometry. Nanodroplet simulations were run on SHARCNET. Desktop computers were used for smaller test systems and code development. Images of MD frames were rendered using VMD [65].

3.3 Results and Discussion

3.3.1 Conducting Sphere with Excess Charge

For the following discussion it is helpful to briefly review the classical arguments [31] that provide the basis for the widely accepted surface charge paradigm of electrosprayed droplets [5, 24, 25, 27-30]. For this purpose, we initially model a droplet as a solid sphere with radius R that consists of a homogeneous and electrically conducting material. The system accommodates a large number of charge carriers, resulting in an excess charge Q. At this level of description, the "ESI droplet" is treated analogously to a charged metal conductor. Gauss' Law [31] states that the electric flux through any closed surface S is equal to the net charge q enclosed within this surface, divided by ε_0.

$$\oint_S \vec{E} \cdot d\vec{A} = \frac{q}{\varepsilon_0} \tag{3.2}$$

$\vec{E}$ in this expression is the electric field, and $d\vec{A}$ is an infinitesimal surface element with a vector direction that coincides with the outward normal. We now evaluate the integral in equation 3.2 for a Gaussian surface that lies just inside the actual surface of the conductor, i.e., where S encompasses all points with radial position $r = R - \delta$, with $\delta << R$. The key point for the argument made here is that the electric field $\vec{E}_{\text{internal}}$ anywhere inside a conductor has to be zero under equilibrium conditions [31]. Hence, it follows from equation 3.2 that the overall charge enclosed by the Gaussian surface is $q = 0$. In other words, all of the charge Q must be located on the surface of the sphere, at $r = R$.

Let us now assume that all charge carriers that constitute Q can be immobilized once equilibrium has been reached. In this way it is possible to map the Coulomb potential of the sphere by means of a point charge q_{test} without disturbing the existing charge distribution. The potential energy $V(r)$ of this point charge as a function of distance r from the droplet center is given by [31]

$$V(r) = constant = C\,R^{-1} \qquad \text{for } r \leq R$$

and (3.3)

$$V(r) = C\,r^{-1} \qquad \text{for } r > R$$

with $C = Q\,q_{test} / (4\pi\varepsilon_0)$. Equation 3.3 represents the hallmark of *any* physical system where an overall charge Q is arranged in a thin spherical layer of radius R. This last point may appear trivial, but it will become important later on.

The behavior predicted by equation 3.2 is readily confirmed by simple MD simulations on charge carriers that are trapped within a spherical conductor of radius R. Figure 3.1 depicts a scenario where the interior of a sphere is modeled as vacuum, where Na^+ ions (mass = 23 Da) move with zero friction while only experiencing their mutual Coulomb repulsion. The boundaries of the conductor were defined by a radial trapping potential $V_{trap}(r) = k \times r$, with $k = 2000$ kJ mol^{-1} Å^{-1} for $r \geq R$, whereas $V_{trap}(r) = 0$ for $r < R$. The radius $R = 21$ Å chosen for this demonstration is typical for droplets during the final stages of the ESI process [5].

Placing 500 ions within the sphere after thermalization at $T = 100$ K results in a spatial distribution where all charge carriers are spread across the surface. No ions are found in the interior (Figure 3.1A). The potential energy $V(r)$ of the sphere was mapped by using a point charge ($q_{test} = +e$), employing the strategy outlined above. Consistent with equation 3.3, this procedure reveals that $V(r)$ in the interior of the sphere is constant ($\vec{E}_{\text{internal}} = 0$). For $r > R$, $V(r)$ shows the expected r^{-1} dependence (Figure 3.1B) [31].

A very similar behavior with all charge carriers at the surface of the sphere is observed when the number of ions is reduced from 500 to 10 (Figure 3.1C, D). Close inspection of the $V(r)$ profile in Figure 3.1D reveals slight deviations from the ideal $\vec{E}_{\text{internal}} = 0$ behavior because charge can no longer be treated as a quasi-continuous entity. Raising the temperature to 1000 K leads to thermal broadening of the distributions in Figure 3.1A, C, but all ions remain confined to the outermost 1.5 Å (data not shown).

In summary, the data of Figure 3.1 confirm the surface charge paradigm [5, 24, 25, 27-30] for an ideal conductor, even in cases where only relatively few ions are involved such that excess charge can no longer be treated as a quasi-continuum entity. Of particular interest for our discussion is Figure 3.1C, D, because the size and charge regime of that scenario is typical for droplets during the final stages of the ESI process. Specifically, an aqueous droplet with R = 21 Å and γ = 0.072 N m^{-1} that carries 10 charges e is close to the Rayleigh limit ($Q = 0.83\ Q_R$, equation 3.1). The first scenario considered above exceeds the Rayleigh limit and was included for illustrative purposes only. On the basis of a two-dimensional model it has previously been proposed that excess charges might be able to adopt stable positions in the interior of a conducting sphere [49]. Along with the predictions of equation 3.2, the results of Figure 3.1 reveal that for the three-dimensional case considered here such an assertion is not correct.

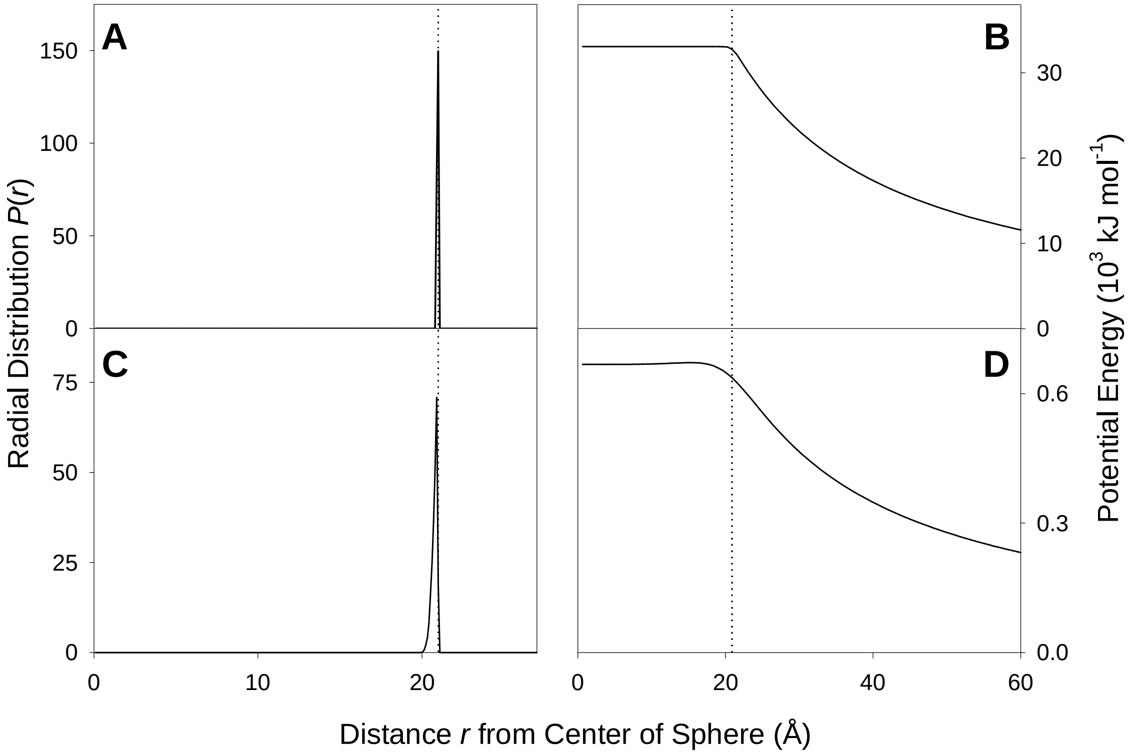

Figure 3.1. Results of constant energy MD simulations for Na^+ ions that are trapped inside a hollow vacuum sphere at 100 K. Radial distributions are shown for the case of 500 (A) and 10 (C) ions. Panels B, D show the corresponding potential energy profiles, obtained by immobilizing the ion positions and mapping the Coulomb energy of a point charge (+*e*) as a function of radial distance r from the center of the sphere. To avoid singularities during this mapping procedure the Coulomb potential was truncated for charge-charge distances of less than 1 Å. Dotted lines at r = 21 Å indicate the radius of the sphere.

3.3.2 Water Droplets Carrying Na^+ and X^- Ions

We will now depart from models that treat ESI nanodroplets as unstructured conductors, and instead explore the behavior of aqueous systems containing atomic ions. The droplets considered here have radii of around 21 Å, comparable to the examples of Figure 3.1. MD simulations on these aqueous systems were based on the full set of LJ and Coulomb potentials, as described in the Methods section. In addition to exploring the behavior of systems with ten Na^+ ions that are close to the Rayleigh limit, we also consider water droplets that contain only a single ion. Additionally, we examine the behavior of negatively charged (-*e*) ions having the same mass and LJ characteristics as Na^+. Although these so-called "X^- ions" do not correspond to any naturally occurring species, they represent a useful tool for comparative studies that provide insights into the origin of Na^+ behavior [36].

Water droplets containing ten Na^+ maintain a shape that is roughly spherical during most of the 1 ns simulation window (Figure 3.2A). Evaporation is negligible on this time scale at the temperature used (320 K), but the droplets undergo occasional surface undulations (Figure 3.2B). Droplets containing ten X^- exhibit a similar behavior (Figure 3.2C). These observations are consistent with earlier MD studies [15, 49-51].

The most pertinent issue in the context of the current study is the location of ions within these aqueous systems. In stark contrast to the behavior seen for an unstructured conducting sphere (Figure 3.1), excess Na^+ and X^- ions are *not* located on the surface of the aqueous droplets. This is illustrated in Figure 3.3, where ionic radial distributions are depicted together with those of H and O. For all cases considered here the water density

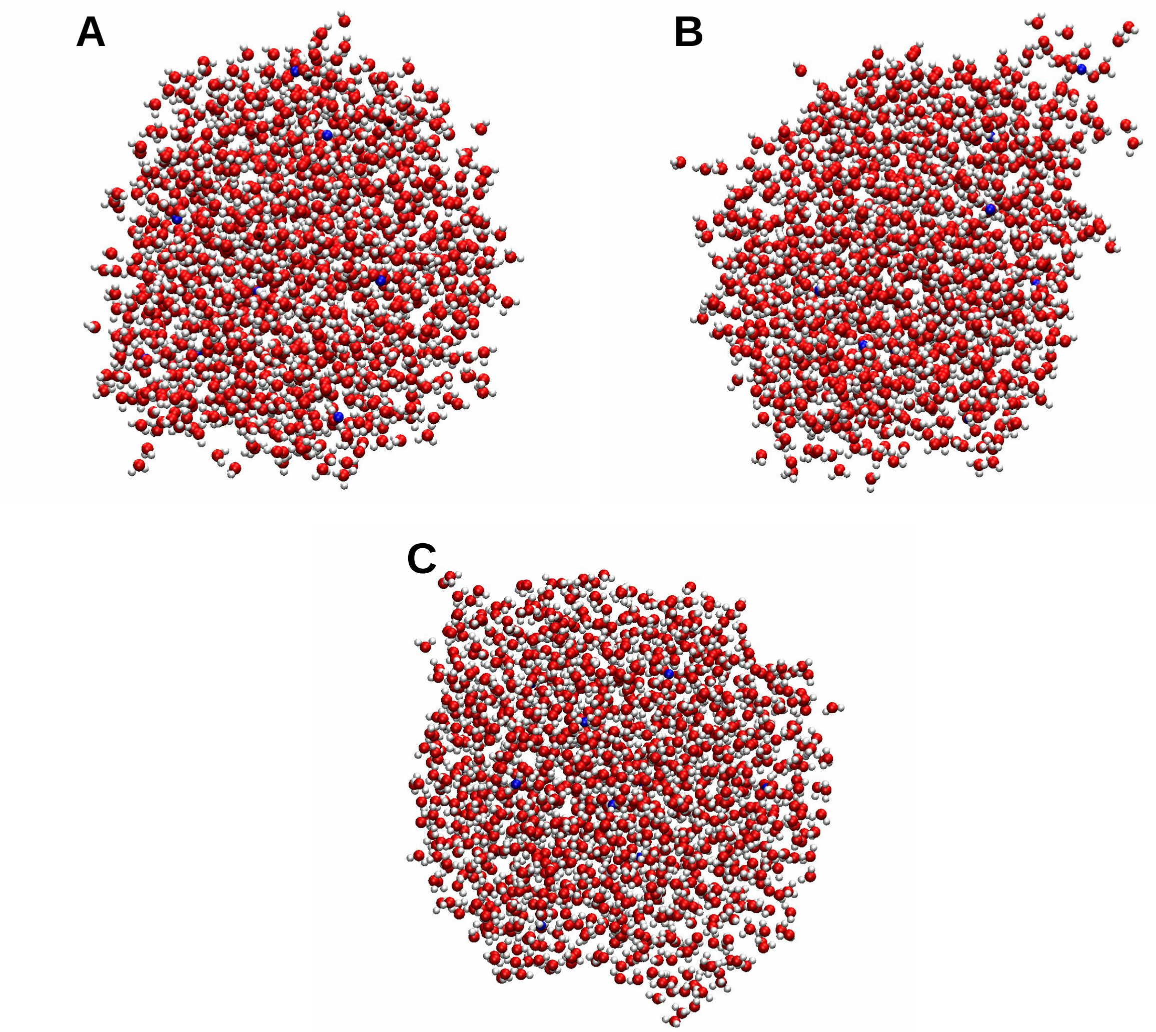

Figure 3.2. Snapshots taken from MD simulations of SPC/E water nanodroplets (O, red; H white) containing 1248 H_2O and 10 charge carriers (blue). Panels A, B are for a system containing Na^+, whereas panel C is for a droplet that contains X^- (see text for details).

in the interior is approximately constant, followed by a sigmoidal transition region towards the vapor phase with a midpoint of roughly 21 Å. Droplets carrying ten Na^+ exhibit a broad ion distribution centered at 13 Å (Figure 3.3A). For systems carrying only one Na^+ the charge distribution is more narrow and its centroid is shifted to r = 9.4 Å (Figure 3.3B). The charge distribution for 10 X^- is similar to that observed in the case of 10 Na^+, with a centroid at 13 Å (Figure 3.3C). Droplets carrying single X^- exhibit a distribution with a centroid at 14 Å (Figure 3.3D). The general phenomena depicted in Figure 3.3 are in line with earlier simulation studies [49, 51, 54]. In the following sections we will explore the internal droplet structure in more detail, with the aim of uncovering why the observed ion distributions are in apparent violation of the surface charge paradigm [5, 24, 25, 27-30].

3.3.3 Local Ion Solvation

For droplets carrying ten sodium ions, the O/Na^+ pair correlation function exhibits a dominant maximum at 2.5 Å and a smaller more diffuse peak at 4.5 Å. The corresponding H/Na^+ signals are found at 3.1 and 5.2 Å (Figure 3.4A). These double peaks for oxygen and hydrogen represent the first and second solvation shells of Na^+. A typical first solvation shell structure is displayed in the inset of Figure 3.4A, showing Na^+ with its six nearest neighbor water molecules in an approximately octahedral arrangement where the oxygens point towards the ion. A dramatically different solvation pattern is observed for X^- (Figure 3.4B). While still being surrounded by six waters, these ions are in close contact with hydrogens, while the oxygen atoms tend to point away from the

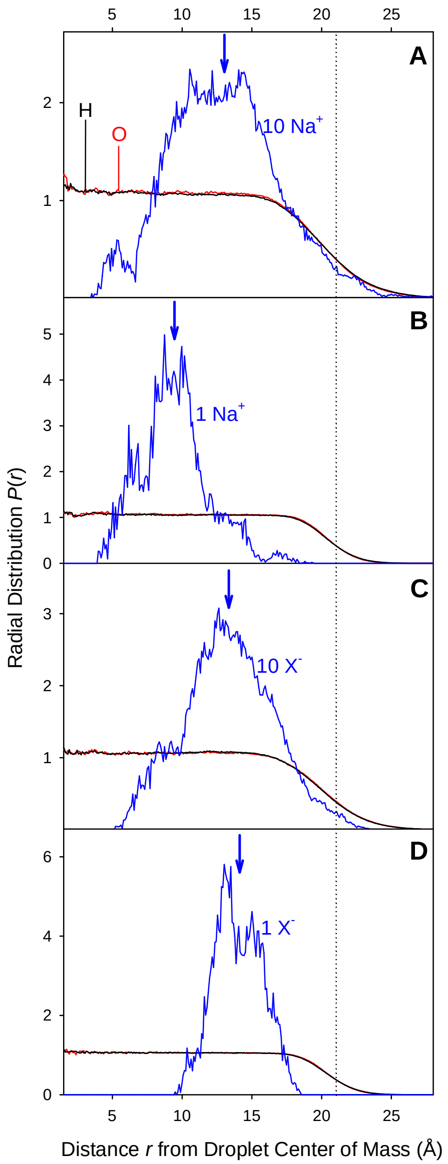

Figure 3.3. Radial distributions of charge carriers (blue) in aqueous droplets containing 10 Na$^+$ (A), 1 Na$^+$ (B), 10 X$^-$ (C), and 1 X$^-$ (D). Vertical blue arrows represent the centroids of these ion distributions. Water distributions are included for comparison (oxygen, red; hydrogen, black). Data were averaged over three 1 ns runs for each panel. The dotted line at *r* = 21 Å indicates the approximate position of the liquid/vapor interface.

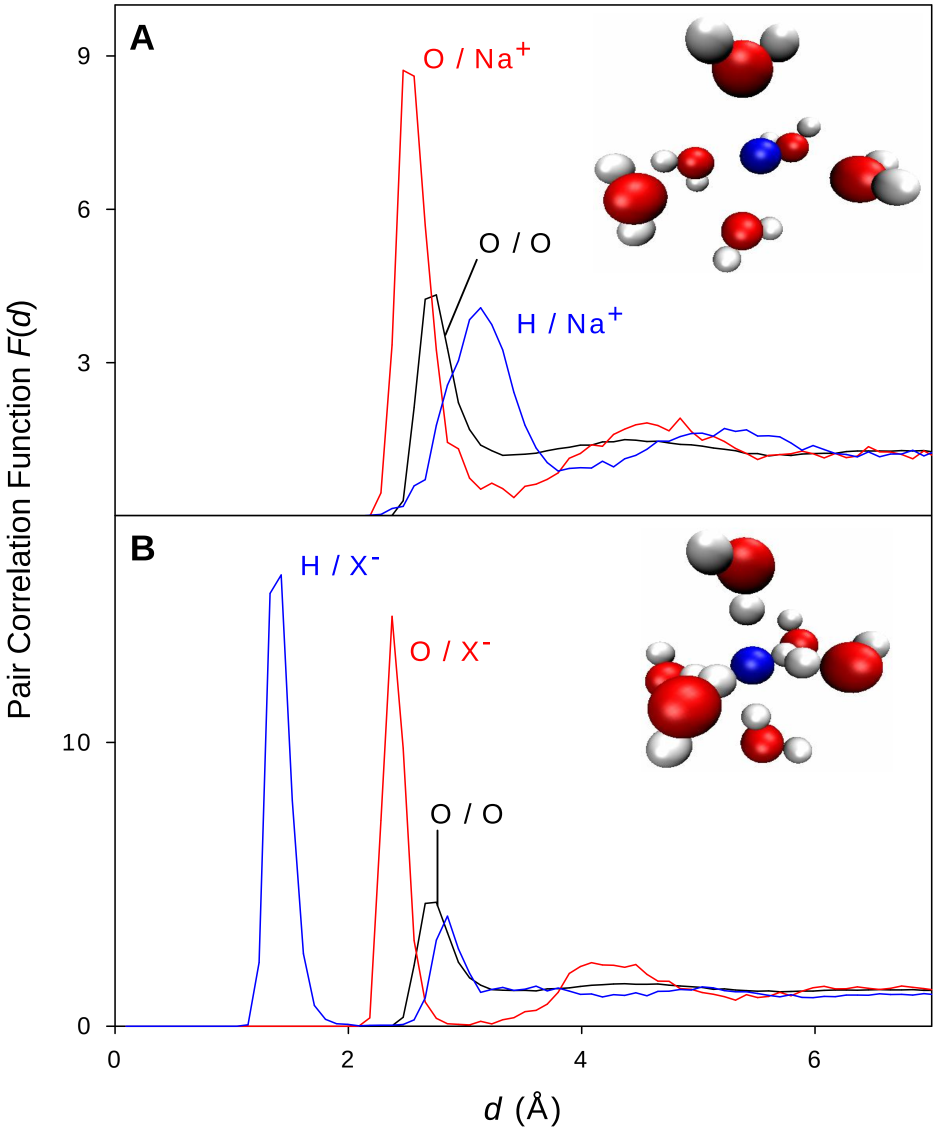

Figure 3.4. Local solvation pattern of Na$^+$ (A) and X$^-$ (B), as revealed through pair correlation functions with oxygen and hydrogen. Oxygen-oxygen data are included for comparison. Insets depict typical snapshots of the Na$^+$ (A) and X$^-$ (B) first solvation shell, obtained by selecting all waters contained within a 3.5 Å sphere around the ion. The data depicted here were obtained for droplets with ten ions; very similar results (not shown) were obtained for systems containing a single ion.

charge center [66]. These differences are readily apparent from the pair correlation function in Figure 3.4B, which has its main H/X$^-$ maximum at 1.4 Å, and a smaller peak at 2.8 Å. The corresponding O/X$^-$ maxima are at 2.4 Å and around 4.2 Å. The relative orientations of water molecules in the second solvation shell are similar to those of the first shell, albeit the former are more disordered (data not shown). The local solvation phenomena depicted in Figure 3.4 are consistent with neutron and X-ray scattering, as well as modeling data obtained for ions in bulk solution [63, 67, 68].

3.3.4 Macrosolvation

Orientational preferences of water can be analyzed by considering the angle θ between the H_2O dipole moment (H-O-H bisector) and the vector that points from oxygen to the droplet center of mass (Figure 3.5). For this analysis the droplets are divided into radial shells with a thickness of 5 Å. We will first examine the dipole orientations for purely aqueous systems, i.e., in the absence of ions. The $P(\cos(\theta))$ [69-71] distributions in this case are flat for radial shells up to approximately 15 Å from the center, representing bulk-like water molecules in random orientations (Figure 3.5A). Orientational preferences become increasingly apparent for radial shells towards the droplet surface. The outermost layer considered here (20-25 Å, red in Figure 3.5A) exhibits a maximum at $\cos(\theta) \approx 0$, corresponding to a preferred orientation where the water dipole moments lay flat on the droplet surface ($\theta \approx 90°$). This finding is consistent with earlier work [71-75]. Surface ordering is further enhanced for layers that are even farther removed from the droplet center ($r > 25$ Å) (Chapter 2), but those data are not

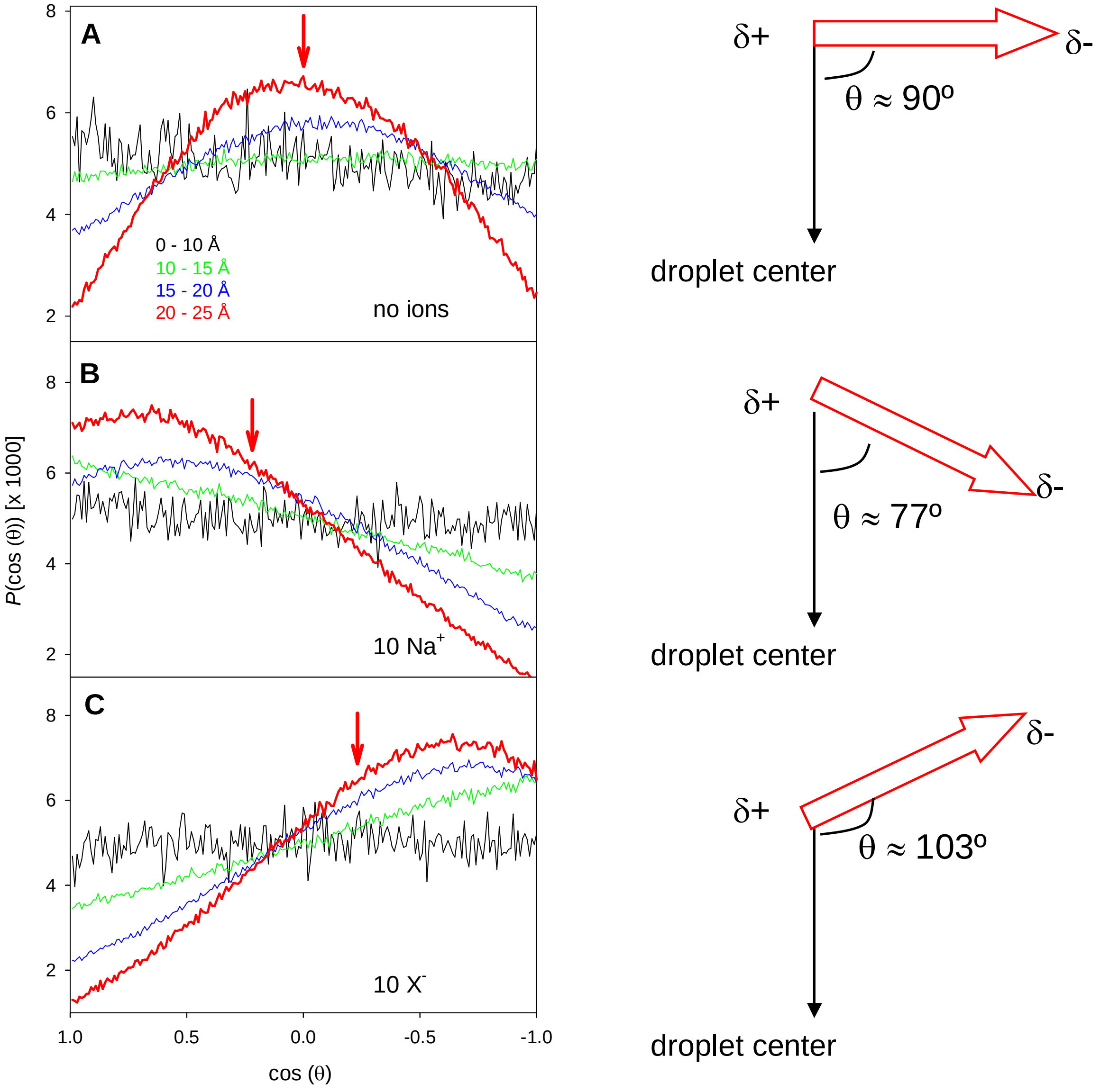

Figure 3.5. Distribution functions of the angle *θ* between the water dipole vector and the vector pointing from oxygen to the droplet center. The panels are for droplets without ions (A), with 10 Na$^+$ (B), and with 10 X$^-$ (C). Data are shown for four different droplet radial shells: 0 - 10 Å (black), 10 - 15 Å (green), 15 - 20 Å (blue), and 20 - 25 Å (red). Vertical red arrows in A-C represent centroids of the 20 - 25 Å (red) distributions. Schematic diagrams along the right hand side depict the most likely water dipole orientations in the 20 - 25 Å radial shell for each of the three cases.

included in Figure 3.5 due to the low particle density in those regions (see Figure 3.3). Angular distributions for systems carrying single Na^+ or X^- ions (not shown) are very similar to those of pure water in Figure 3.5A.

Dramatically different dipole orientations are observed for systems that contain ten excess ions. In the case of droplets with 10 Na^+, water close to the surface exhibits preferred orientations where the negative (oxygen) end of the dipole moment is tilted towards the droplet interior at an angle of $\theta \approx 77^o$ (Figure 3.5B). The opposite effect is observed for droplets with 10 X^- ions, resulting in preferred surface orientations where oxygen points away from the interior at $\theta \approx 103^o$ (Figure 3.5C). The data of Figure 3.5 demonstrate that the presence of ten excess ions has profound consequences for all molecules located within the outer droplet layers. The sign of the excess charge electrostatically dictates the tilt angle of the water dipoles. The resulting large-scale orientational polarization[1] provides enthalpically favorable charge-dipole interactions that go far beyond the local solvation patterns depicted in Figure 3.4.

3.3.5 Location of Charge in Droplets with Excess Ions

We will now return to the key question addressed in this work, namely the ion distribution within highly charged water nanodroplets. As pointed out, our finding that Na^+ and X^- reside in the interior (Figure 3.3) is in apparent conflict with the general notion [5, 24, 25, 27-30] that excess charge carriers should be located on the droplet surface.

---

[1] Readers are reminded that *electronic polarization* refers to the induction of dipole moments in an electric field, an effect that is not considered in our study (see Introduction). In contrast, o*rientational polarization* results from the alignment of pre-existing dipole moments. The latter phenomenon is fully captured by the modeling strategy used here.

The key to solving this conundrum is found by mapping the Coulomb energy of a point charge (q_{test} = +e) that probes the combined contributions of all H, O, and Na^+ charge centers within the droplet. Remarkably, the time-averaged energy profile for droplets containing 10 Na^+ is virtually constant up to $r \approx 26$ Å, followed by a r^{-1} decrease (red curve in Figure 3.6A). Superimposed on these data is the $V(r)$ profile of an arrangement where a charge of $Q = +10\ e$ is evenly spread on the surface of a sphere with $R = 26$ Å (Equation 3.3, dashed line in Figure 3.6A). It is evident that the two profiles are in very close agreement with each other. On the basis of the discussion above (Equation 3.3), we have to conclude that droplets containing ten Na^+ carry all their excess charge in a surface layer located ca. 26 Å from the droplet center.

How is it possible for excess charge to reside at the extreme periphery of the droplet ($r \approx 26$ Å), while all ten Na^+ are buried in the interior ($r \approx 13$ Å)? Figure 3.7A shows in cartoon representation how the interaction of an ion with two oriented dipoles effectively neutralizes a fraction of the ionic charge at site r_1, thereby transferring this fractional charge to the opposite end of the dipole chain at r_2. In Figure 3.7B it is illustrated how the large-scale orientational polarization of water molecules (Figure 3.5B) leads to charge transfer from buried Na^+ to the droplet surface via such a mechanism. Thus, Na^+ ions in the droplet interior become effectively "neutralized" by solvation, while the positive ends of water dipoles at the droplet periphery assume the role of surface charge.

A transfer mechanism symmetrical to that illustrated in Figure 3.7 for Na^+ is also operative for droplets containing 10 X^-. Following arguments that are analogous to those outlined above, Coulomb energy scanning with q_{test} = -e reveals that excess charge is

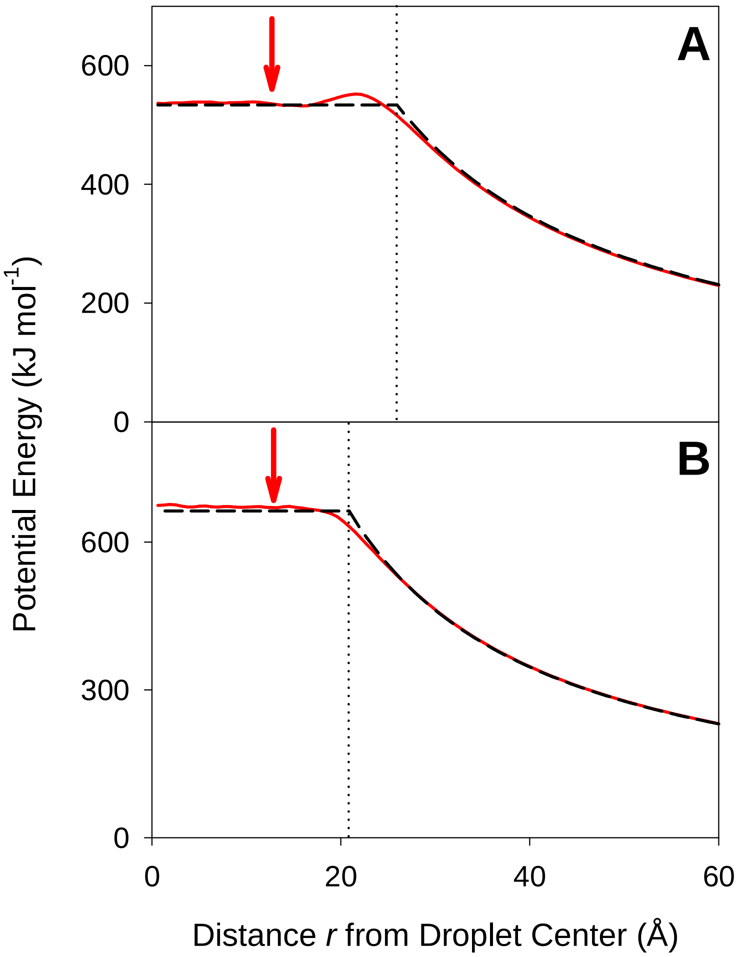

Figure 3.6. (A) Red curve: Coulomb energy profile experienced by a point charge (q_{test} = +e) for droplets containing 10 Na^+ ions. This profile includes all interaction of the point charge with H, O, and Na^+. Dashed line: $V(r)$ profile predicted by Equation 3.3 for a sphere that carries a surface charge layer of Q = +10 e at R = 26 Å. (B) Same as in panel A but for droplets containing 10 X^- ions and a point charge q_{test} = -e. The theoretical $V(r)$ profile in (B) is based on Q = -10 e and R = 21 Å. Red vertical arrows denote centroids of ion radial distributions from Figure 3.3A, C. Vertical dotted lines indicate R values. Red profiles represent data that were averaged over three 1 ns MD runs.

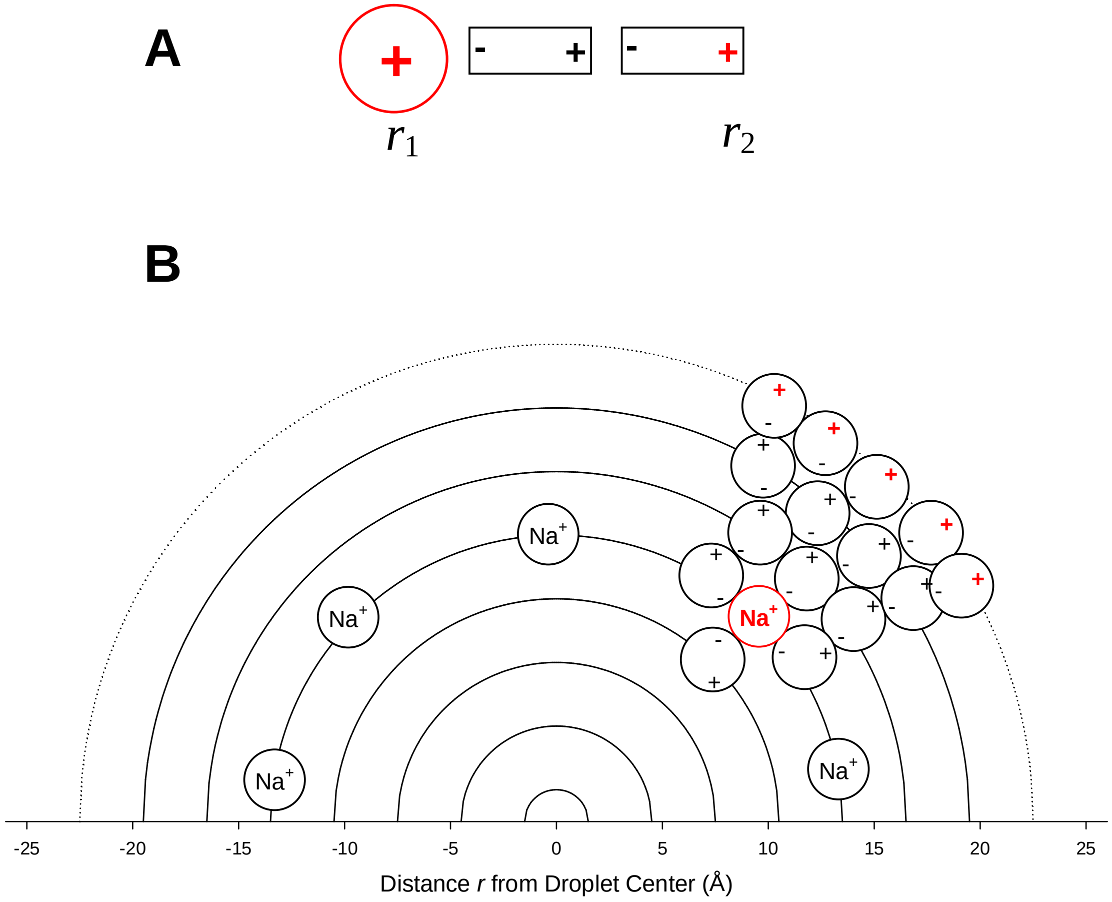

Figure 3.7. (A) Schematic cartoon, illustrating how the interaction of a cation with two oriented dipoles effectively transfers a fraction of the positive charge from position r_1 to r_2. (B) Schematic semi-cross section through an aqueous nanodroplet carrying excess Na^+ ions. Concentric circles represent the approximate spacing of water molecules. For one of the Na^+ ions (red) this cartoon illustrates how orientational polarization of water dipoles acts to transfer the ionic charge from the interior to the surface. Note that this representation greatly exaggerates the extent of water ordering, compared to the actual situation of Figure 3.5.

entirely located on the droplet surface, although the X^- ions reside in the interior (Figure 3.6B). In the case of X^- the orientational solvent polarization (Figure 3.5C) causes the *negative* ends of the water dipoles at the droplet periphery to assume the role of surface charge. The location of the resulting surface charge layer is at $r \approx 21$ Å (Figure 3.6B).

The discussion of this paragraph reconciles the surface charge paradigm for ESI nanodroplets [5, 24, 25, 27-30] with the tendency of small atomic ions to maximize enthalpically favorable solvation by migrating into the interior. Excess charge is indeed located on the droplet surface, but only in the form of half-dipoles that point into the water-vapor interface as a result of orientational solvent polarization. This arrangement allows all ions to remain fully solvated in the droplet interior. In contrast to earlier proposals [25, 49], therefore, the presence of a charged surface layer on ESI nanodroplets does *not* imply that the actual charge carriers (ions) have to be located at the water/vapor interface.

The charge transfer phenomenon illustrated in Figure 3.7 bears a remote analogy to the Grotthus mechanism of H^+ transfer in water [57, 58], but we caution that this comparison should not be overextended. Grotthus migration involves the rearrangement of H- bonds, whereas the effect considered here originates from the orientation of pre-existing dipoles.

3.3.6 Preferred Ion Depth

The previous discussion has made it clear that Na^+ and X^- do not reside at the droplet surface because this would imply the loss of enthalpically favorable local solvation, as well as macrosolvation. On the other hand, Figure 3.3 reveals that the ions also avoid the innermost droplet regions, giving rise to preferred positions in the 9 - 14 Å range. It is interesting to briefly discuss the factors that determine the optimal penetration depth of the ions relative to the droplet center.

In the absence of any other considerations, one might naively assume that ion solvation is most favorable at $r \approx 0$. For droplets containing multiple ions it is obvious, however, that positions in the droplet center will be disfavored by mutual Coulomb repulsion, as well as solvation shell distortions (Figure 3.4). The significance of both aspects can be tested by reducing the number of ions from ten to one, such that charge-charge repulsion and the distortion of solvation shells by other ions are eliminated.

Consistent with our expectation, droplets containing a single Na^+ have their centroid shifted somewhat more to the droplet center than the systems containing ten Na^+ (Figure 3.3A, B). However, in the case of X^- this effect is not observed (Figure 3.3C, D). More importantly, even for the single ion systems there remains an obvious tendency to avoid the innermost regions (Figure 3.3B, D). We conclude that ion exclusion from the $r \approx 0$ region must involve factors in addition to those considered above. Specifically, we note that any ordering of water is entropically unfavorable [45]. The droplet interior ($r <$ 10 Å) has bulk-like properties without any orientational preferences for all the systems studied here (Figure 3.5). Placing an ion with its relatively ordered local solvation shells (Figure 3.4) close to the center would reduce the entropy of the droplet interior, thereby repelling ions from the center region. We propose that this "entropic buoyancy" is a major factor that prevents ions from venturing close to the droplet midpoint.

3.4 Conclusions

This study examined the structure of aqueous nanodroplets containing excess charge due to the presence of small atomic ions. Droplets of this type play an important role for mechanistic studies on the ESI process [5, 15, 25, 49, 76]. Understanding the physical properties of these systems, therefore, is of considerable importance.

The widely accepted notion that excess charge is located on the surface of ESI nanodroplets is in apparent conflict with the well known tendency of ions such as Na^+ to maximize charge-solvent interactions by migrating towards the bulk. The MD simulations of this work confirm that charged droplets exhibit ion radial distributions centered around 2/3 R (for $R \approx 21$ Å), where solvation requirements are fully satisfied. In other words, *excess* Na^+ *ions are not located at the droplet surface*. Nonetheless, Coulomb energy mapping reveals that *all excess charge is confined to a thin layer at the droplet periphery*. These seemingly contradictory findings are reconciled on the basis of charge-induced orientation of water dipole moments. Ions in the droplet interior become effectively neutralized through charge-dipole interactions. Orientational polarization of water molecules then acts to transfer the excess charge to the droplet periphery. Figure 3.7 illustrates how the charge layer generated in this way at the water/vapor interface can be thought of as unpaired half-dipoles. This layer has exactly the same time-averaged magnitude as the buried ionic charge Q (Figure 3.6). Related phenomena have recently been discussed by Consta [77].

Although not explicitly addressed in the current work, our findings have implications for the mechanism by which Na^+ and other small ions are released into the gas phase during the final stages of ESI. It is usually assumed that this process occurs via the ion evaporation mechanism [5, 25, 26]. According to this model, ions reside close to the surface of the droplet, from where they can be electrostatically ejected. Our results indicate that excess Na^+ ions are not part of the charged surface layer, such that their ejection directly from the water/vapor interface may not be feasible. Recent work suggests that these emission events more likely proceed through thin liquid jets [15]. In future work it will be interesting to extend studies of the type performed here to aqueous/organic solvent mixtures, and other ESI charge carriers including hydrated protons and ammonium ions.

3.5 References

1. Fenn, J.B., M. Mann, C.K. Meng, S.F. Wong, and C.M. Whitehouse, *Electrospray Ionization for Mass Spectrometry of Large Biomolecules.* Science, 1989. **246**: p. 64-71.

2. Griffiths, J., *A Brief History of Mass Spectrometry.* Anal. Chem., 2008. **80**: p. 5678-5683.

3. Hofstadler, S.A. and K.A. Sannes-Lowery, *Applications of ESI-MS in drug discovery: interrogation of noncovalent complexes.* Nat. Rev. Drug Discov., 2006. **5**: p. 585-595.

4. Kaltashov, I.A., C.E. Bobst, R.R. Abzalimov, S.A. Berkowitz, and D. Houde, *Conformation and Dynamics of Biopharmaceuticals: Transition of Mass Spectrometry-Based Tools from Academe to Industry.* J. Am. Soc. Mass Spectrom., 2010. **21**: p. 323-337.

5. Kebarle, P. and U.H. Verkerk, *Electrospray: From Ions in Solutions to Ions in the Gas Phase, What We Know Now.* Mass Spectrom. Rev., 2009. **28**: p. 898-917.

6. Benesch, J.L.P., B.T. Ruotolo, D.A. Simmons, and C.V. Robinson, *Protein Complexes in the Gas Phase: Technology for Structural Genomics and Proteomics.* Chem. Rev., 2007. **107**: p. 3544-3567.

7. Van Berkel, G.J. and V. Kertesz, *Electrochemistry/spray Ion Source.* Anal. Chem., 2007. **79**: p. 5511-5520.

8. Verkerk, U.H. and P. Kebarle, *Ion-Ion and Ion-Molecule Reactions at the Surface of Proteins Produced by Nanospray. Information on the Number of Acidic Residues and Control of the Number of Ionized Acidic and Basic Residues.* J. Am. Soc. Mass Spectrom., 2005. **16**: p. 1325-1341.

9. Felitsyn, N., M. Peschke, and P. Kebarle, *Origin and number of charges observed on multiply-protonated native proteins produced by ESI.* Int. J. Mass Spectrom. Ion Proc., 2002. **219**: p. 39-62.

10. Loo, J.A., R.R.O. Loo, K.J. Light, C.G. Edmonds, and R.D. Smith, *Multiply Charged Negative Ions by Electrospray Ionization of Polypeptides and Proteins.* Anal. Chem., 1992. **64**: p. 81-88.

11. Rayleigh, L., *On the Equilibrium of Liquid Conducting Masses charged with Electricity.* Phil. Mag., 1882. **14**: p. 184-186.

12. Gomez, A. and K. Tang, *Charge and fission of droplets in electrostatic sprays.* Phys. Fluids, 1994. **6**: p. 404-414.

13. Duft, D., T. Achtzehn, R. Muller, B.A. Huber, and T. Leisner, *Coulomb fission: Rayleigh jets from levitated microdroplets.* Nature, 2003. **421**: p. 128.

14. Konermann, L., *A Simple Model for the Disintegration of Highly Charged Solvent Droplets during Electrospray Ionization.* J. Am. Soc. Mass Spectrom., 2009. **20**: p. 496-506.

15. Marginean, I., V. Znamenskiy, and A. Vertes, *Charge Reduction in Electrosprays: Slender Nanojets as Intermediates.* J. Phys. Chem. B, 2006. **110**: p. 6397-6404.

16. Wang, R. and R. Zenobi, *Evolution of the Solvent Polarity in an Electrospray Plume.* J. Am. Soc. Mass Spectrom., 2010. **21**: p. 378-385.

17. Zhou, S. and K.D. Cook, *Probing Solvent Fractionation in Electrospray Droplets with Laser-Induced Fluorescence of a Solvatochromic Dye.* Anal. Chem., 2000. **72**: p. 963-969.

18. Kaltashov, I.A. and A. Mohimen, *Estimates of Protein Surface Area in Solution by Electrospray Ionization Mass Spectrometry.* Anal. Chem., 2005. **77**: p. 5370-5379.

19. Cech, N.B. and C.G. Enke, *Practical Implication of Some Recent Studies in Electrospray Ionization Fundamentals.* Mass Spectrom. Rev., 2001. **20**: p. 362-387.

20. Cole, R.B., *Electrospray Ionization Mass Spectrometry*. 1997, New York: John Wiley & Sons, Inc.

21. Wang, G. and R.B. Cole, *Charged residue versus ion evaporation for formation of alkali metal halide clusters ions in ESI.* Anal. Chim. Acta, 2000. **406**: p. 53-65.

22. Dole, M., L.L. Mack, R.L. Hines, R.C. Mobley, L.D. Ferguson, and M.B. Alice, *Molecular beams of macroions.* J. Chem. Phys., 1968. **49**: p. 2240-2249.

23. de la Mora, F.J., *Electrospray Ionization of large multiply charged species proceeds via Dole's charged residue mechanism.* Anal. Chim. Acta, 2000. **406**: p. 93-104.

24. Iavarone, A.T. and E.R. Williams, *Mechanism of Charging and Supercharging Molecules in Electrospray Ionization.* J. Am. Chem. Soc., 2003. **125**: p. 2319-2327.

25. Iribarne, J.V. and B.A. Thomson, *On the evaporation of small ions from charged droplets.* J. Chem. Phys., 1975. **64**: p. 2287-2294.

26. Nguyen, S. and J.B. Fenn, *Gas-phase ions of solute species from charged droplets of solutions.* Proc. Natl. Acad. Sci. U.S.A., 2007. **104**: p. 1111-1117.

27. Hogan, C.J., J.A. Carroll, H.W. Rohrs, P. Biswas, and M.L. Gross, *Combined Charged Residue-Field Emission Model of Macromolecular Electrospray Ionization.* Anal. Chem., 2009. **81**: p. 369-377.

28. Fenn, J.B., J. Rosell, and C.K. Meng, *In Electrospray Ionization, How Much Pull Does an Ion Need to Escape Its Droplet Prison.* J. Am. Soc. Mass Spectrom., 1997. **8**: p. 1147-1157.

29. Fenn, J.B., *Ion Formation from Charged Droplets: Roles of Geometry, Energy, and Time.* J. Am. Soc. Mass Spectrom., 1993. **4**: p. 524-535.

30. Bruins, A.P., *Mechanistic aspects of electrospray ionization.* J. Chromatogr. A, 1998. **794**: p. 345-357.

31. Halliday, D., R. Resnick, and K.S. Krane, *Physics*. 4 ed. 1992, New York: Wiley.

32. Onsager, L. and N.N.T. Samaras, *The Surface Tension of Debye-Hückel Electrolytes.* J. Chem. Phys., 1934. **2**: p. 528-536.

33. Messina, R., *Electrostatics in soft matter.* J. Phys.: Condens. Matter, 2009. **21**: p. 1-18.

34. Jungwirth, P. and D.J. Tobias, *Ions at the air/water interface.* J. Phys. Chem. B, 2002. **106**: p. 6361-6373.

35. Chang, T.-M. and L.X. Dang, *Recent advances in molecular simulations of ion solvation at liquid interfaces.* Chem. Rev., 2006. **106**: p. 1305-1322.

36. Benjamin, I., *Theoretical study of ion solvation at the water liquid–vapor interface.* J. Chem. Phys., 1991. **95**: p. 3698-3709.

37. Jungwirth, P. and D.J. Tobias, *Molecular structure of salt solutions: A new view of the interface with implications for heterogeneous atmospheric chemistry.* J. Phys. Chem. B, 2001. **105**: p. 10468-10472.

38. Wick, C.D. and L.X. Dang, *Recent advances in understanding transfer ions across aqueous interfaces.* Chem. Phys. Lett., 2008. **458**: p. 1-5.

39. Knipping, E.M., M.J. Lakin, K.L. Foster, P. Jungwirth, D.J. Tobias, R.B. Gerber, D. Dabdub, and B.J. Finlayson-Pitts, *Ion-enhanced interfacial chemistry on aqueous NaCl aerosols.* Science, 2000. **288**: p. 301-306.

40. Burnham, C.J., M.K. Petersen, T.J.F. Day, S.S. Iyengar, and G.A. Voth, *The properties of ion-water clusters. II. Solvation structures of Na+, Cl-, and H+ clusters as a function of temperature.* J. Chem. Phys., 2006. **124**: p. 024327.

41. Tian, C.S. and Y.R. Shen, *Structure and Charging of Hydrophobic Material/Water Interfaces Studied by Phase-Sensitive Sum-Frequency Vibrational Spectroscopy.* Proc. Natl. Acad. Sci. U.S.A., 2009. **106**: p. 15148-15153.

42. Petersen, P.B. and R.J. Saykally, *Is the liquid water surface basic or acidic? Macroscopic vs. molecular-scale investigations.* Chem. Phys. Lett., 2008. **458**: p. 255-261.

43. Iuchi, S., H. Chen, F. Paesani, and G.A. Voth, *Hydrated Excess Proton at Water-Hydrophobic Interfaces.* J. Phys. Chem. B, 2009. **113**: p. 4017-4030.

44. Kuprowski, M.C. and L. Konermann, *Signal Response of Co-Existing Protein Conformers in Electrospray Mass Spectrometry.* Anal. Chem., 2007. **79**: p. 2499-2506.

45. Chandler, D., *Interfaces and the driving force of hydrophobic assembly.* Nature, 2005. **437**: p. 640-647.

46. Du, Q., E. Freysz, and Y.R. Shen, *Surface vibrational spectroscopic studies of hydrogen bonding and hydrophobicity.* Science, 1994. **264**: p. 826-828.

47. Trudeau, T.G., K.C. Jena, and D.K. Hore, *Water Structure at Solid Surfaces of Varying Hydrophobicity.* J. Phys. Chem. C, 2009. **113**: p. 20002-20008.

48. Moore, F.G. and G.L. Richmond, *Integration or Segregation: How do molecules behave at oil/water interfaces?* Acc. Chem. Res., 2008. **41**: p. 739-748.

49. Znamenskiy, V., I. Marginean, and A. Vertes, *Solvated Ion Evaporation from Charged Water Droplets.* J. Phys. Chem. A, 2003. **107**: p. 7406-7412.

50. Consta, S., K.R. Mainer, and W. Novak, *Fragmentation mechanisms of aqueous clusters charged with ions.* J. Chem. Phys., 2003. **119**: p. 10125-10132.

51. Ichiki, K. and S. Consta, *Disintegration Mechanisms of Charged Aqueous Nanodroplets Studied by Simulations and Analytical Models.* J. Phys. Chem. B, 2006. **110**: p. 19168-19175.

52. Konermann, L., *A Minimalist Model for Exploring Conformational Effects on the Electrospray Charge State Distribution of Proteins.* J. Phys. Chem. B, 2007. **111**: p. 6534-6543.

53. Iyengar, S.S., T.J.F. Day, and G.A. Voth, *On the amphiphilic behavior of the hydrated proton: an ab initio molecular dynamics study.* Int. J. Mass Spectrom., 2005. **241**: p. 197-204.

54. Caleman, C. and D. van der Spoel, *Evaporation from water clusters containing singly charged ions.* Phys. Chem. Chem. Phys., 2007. **9**: p. 5105-5111.

55. Berendsen, H.J.C., J.R. Grigera, and T.P. Straatsma, *The missing term in effective pair potentials.* J. Phys. Chem., 1987. **91**: p. 6269-6271.

56. Park, M., I. Shin, N.J. Singh, and K.S. Kim, *Eigen and zundel forms of smaller protonated water clusters: Structures and infrared spectra.* J. Phys. Chem. A, 2007. **111**: p. 10692-10702.

57. Cukierman, S., *Et tu, Grotthuss! and other unfinished stories.* Biochimica et Biophysica Acta, 2006. **1757**: p. 876-885.

58. Marx, D., *Proton transfer 200 years after von Grotthuss: Insights from Ab initio simulations.* ChemPhysChem., 2006. **7**: p. 1848-1870.

59. Verlet, L., *Computer "Experiments" on Classical Fluids. I. Thermodynamical Properties of Lennard-Jones Molecules.* Phys. Rev., 1967. **159**: p. 98-103.

60. Frenkel, D. and B. Smit, *Understanding Molecular Simulations: From Algorithms To Applications*. 1996, San Diego: Academic Press.

61. Nose, S., *A molecular dynamics method for simulations in the canonical ensemble.* Mol. Phys., 1984. **52**: p. 255-268.

62. Hoover, W.G., *Canonical dynamics: Equilibrium phase-space distributions.* Phys. Rev. A, 1985. **31**: p. 1695-1697.

63. Koneshan, S., J.C. Rasaiah, R.M. Lynden-Bell, and S.H. Lee, *Solvent structure, dynamics and ion mobility in aqueous solutions at 25 C.* J. Phys. Chem. B, 1998. **102**: p. 4193-4204.

64. Delhommelle, J. and P. Millie, *Inadequacy of the Lorentz-Berthelot combining rules for accurate predictions of equilibrium properties by molecular simulation.* Mol. Phys., 2001. **99**: p. 619-625.

65. Humphrey, W., A. Dalke, and K. Schulten, *VMD - Visual Molecular Dynamics.* J. Mol. Graphics, 1996. **14**: p. 33-38.

66. Tielrooij, K.J., N. Garcia-Araez, M. Bonn, and H.J. Bakker, *Cooperativity in Ion Hydration.* Science, 2010. **328**: p. 1006-1009.

67. Bouazizi, S., S. Nasr, N. Jaidane, and M.-C. Bellissent-Funel, *Local order in aqueous NaCl solutions and pure water: X-ray scattering and molecular dynamics simulations study.* J. Phys. Chem. B, 2006. **110**: p. 23515-23523.

68. Marcus, Y., *Effect of Ions on the Structure of Water: Structure Making and Breaking.* Chem. Rev., 2009. **109**: p. 1346-1370.

69. Brodskaya, E.N., J.C. Eriksson, A. Laaksonen, and A.I. Rusanov, *Local structure and work of formation of water clusters studied by molecular dynamics simulations.* J. Colloid Interf. Sci., 1996. **180**: p. 86-97.

70. Rossky, P.J. and M. Karplus, *Solvation. A Molecular Dynamics Study of a Dipeptide in Water.* J. Am. Chem. Soc., 1979. **101**: p. 1913-1937.

71. Belch, A.C. and M. Berkowitz, *Molecular dynamics simulations of TIPS2 water restricted by a spherical hydrophobic boundary.* Chem. Phys. Lett., 1985. **113**: p. 278-282.

72. Wang, L. and J. Hermans, *The dielectric properties of simulated water droplets.* Mol. Simulat., 1996. **17**: p. 67-74.

73. Townsend, R.M. and S.A. Rice, *Molecular dynamics studies of the liquid–vapor interface of water.* J. Chem. Phys., 1991. **94**: p. 2207-2218.

74. Lee, C.-Y., J.A. McCammon, and P.J. Rossky, *The structure of liquid water at an extended hydrophobic surface.* J. Chem. Phys., 1984. **80**: p. 4448-4455.

75. Kathmann, S.M., I.-F.W. Kuo, and C.J. Mundy, *Electronic Effects on the Surface Potential at the Vapor-Liquid Interface of Water.* J. Am. Chem. Soc., 2008. **130**: p. 16556–16561.

76. Van Berkel, G.J., J.F. De La Mora, C.G. Enke, R.B. Cole, M. Martinez-Sanchez, and J.B. Fenn, *Electrochemical processes in electrospray ionization mass spectrometry.* J. Mass Spectrom., 2000. **35**: p. 939-952.

77. Consta, S., *Manifestation of Rayleigh Instability in Droplets Containing Multiply Charged Macroions.* J. Phys. Chem. B, 2010. **114**: p. 5263–5268.

Chapter 4 – Ejection of Solvated Ions from Electrosprayed Methanol/Water Nanodroplets Studied by Molecular Dynamics Simulations

4.1 Introduction

Ever since Rayleigh's seminal studies in the late 1800s [1], electrically charged solvent droplets have been the subject of experimental and theoretical investigations. Recent work has focused on these systems from an electrospray ionization (ESI) perspective [2-15], although charged droplets also play an important role in atmospheric chemistry. ESI represents one of the most commonly used ionization methods for mass spectrometry (MS) [16], and it allows the transfer of a wide range of analytes from solution into the gas phase. During ESI droplets of analyte solution are emitted from the tip of a Taylor cone. For typical infusion rates of a few microliters per minute the radii of the initially formed droplets are in the micrometer range [17]. In positive ion mode, the droplets carry excess charge due to the presence of cationic species such as protons, sodium, or ammonium ions. Solvent evaporation reduces the droplet size to a point where cohesive interactions are balanced by electrostatic repulsion. At this so-called Rayleigh limit the net charge Q_R is given by [1, 2]

$$Q_R = 8\pi(\varepsilon_0 \gamma r_0^{\ 3})^{1/2} \tag{4.1}$$

where r_0 is the droplet radius, ε_0 is the permittivity of the vacuum, and γ is the surface tension. Droplets close to the Rayleigh limit can distort into non-spherical shapes with Taylor cone-like surface protrusions. This is followed by jet emission of smaller but highly charged progeny droplets from the protrusion tips [2, 18, 19]. Droplet fission events of this type may occur as thermally activated processes even slightly below Q_R. The significance of Equation 4.1 is that the activation barrier height becomes zero at the Rayleigh limit, such that certain types of droplet disintegration events can proceed in an energetic downhill fashion [1, 19-21]. Repeated evaporation/fission events ultimately lead to nanometer-sized droplets from which analyte molecules are released as intact gas phase ions.

The final steps of the ESI process are still a matter of debate, and two limiting scenarios are usually discussed in the literature. Large gas phase analyte ions such as proteins are likely formed by the charged residue mechanism (CRM), first proposed by Dole [22]. According to this scenario the final ESI nanodroplets are just slightly larger than the macromolecular species contained within them. Free gas phase ions are formed by evaporation to dryness, concomitant with transfer of most of the droplet charge to the analyte [2, 23]. Experimental support for the CRM comes from the fact that the ESI charge states of globular proteins match the Q_R value (equation 4.1) expected for water droplets of the same size [24-28]. Also, the formation of salt clusters [29] and nonspecific adducts [30-32] during ESI has been interpreted as evidence in favor of the CRM.

Very small analyte ions are thought to be formed via the ion evaporation mechanism (IEM), a framework developed by Iribarne and Thomson [33, 34] and subsequently expanded by others [35-38]. Most investigations related to the IEM have focused on the generation of gas phase species such as Na^+ and NH_4^+ that exist as preformed ions in solution. The early events of solvent evaporation and droplet fission are the same as for the CRM. However, once a critical droplet radius of a few nanometers is reached the IEM stipulates that the electric field at the droplet surface becomes sufficiently high to allow the ejection of solvated charge carriers into the vapor phase [2, 15, 33, 36, 37]. Transition state theory has been applied to express the first-order rate constant k of these field emission events as [33, 36, 37, 39]

$$k = \frac{k_B T}{h} \exp\left(\frac{-\Delta G^*}{k_B T} \right) \tag{4.2}$$

where ΔG^* represents the height of the activation free energy barrier, k_B is the Boltzmann constant, h is Planck's constant, and T is the temperature.

The distinction between CRM and IEM on the basis of analyte size remains a matter of debate [39, 40]. Some researchers propose that the IEM is operative even for proteins and other large analytes [41, 42]. It has also been noted that protein charge states do not always follow the surface tension dependence that is expected for the CRM (equation 4.1) [43]. Proposals of hybrid mechanisms have been put forward that involve elements of both the CRM and the IEM [13].

The difficulties in arriving at a comprehensive understanding of the ESI process are related to the fact that nanometer-sized droplets occupy a size regime that is difficult to access experimentally. Insights into the behavior of much larger (early) ESI droplets come from phase Doppler interferometry [44] and from various imaging techniques [45-48]. At the other end of the size spectrum, small clusters containing only a few dozen solvent molecules can be interrogated by infrared spectroscopy [49-51] and by direct mass analyses [52]. Late ESI droplets, however, contain on the order of a few thousand solvent molecules which makes them challenging targets for those experimental techniques.

Molecular dynamics (MD) simulations represent an interesting approach for gaining insights into the behavior of nanometer-sized droplets [10, 11, 14, 53-59]. For example, Znamenskiy et al. [53] used this approach for studying the ejection of solvated low molecular weight ions. It was found that ion emission occurs from the tip of transient solvent protrusions, resembling asymmetric droplet fission events seen in experiments on much larger systems [45, 46, 48]. Another recent study explored the location of charge carriers within ESI droplets. Much of the ESI literature implies that excess ions should be located directly at the solvent/vapor interface, as predicted by continuum electrostatic considerations [1, 2, 23, 41]. This view is in apparent conflict with the tendency of ions such as Na^+ to migrate towards the interior where solvation is more favorable (Chapter 2) [54], a point that was already raised in the initial IEM paper [33]. MD simulations reconciled the two viewpoints by demonstrating that small atomic cations do indeed reside within the droplet, but that all of the excess charge is projected to the outermost solvent layers by dipole-mediated polarization effects (Chapter 3).

The current work employs MD simulations for gaining better insights into the structure and dynamics of nanometer-sized (late) ESI droplets at the Rayleigh limit, with particular focus on the mechanism of charge carrier ejection ("ion evaporation"). Most previous ESI modeling studies focused on aqueous systems, whereas mixed aqueous/organic droplets have been explored to a much lesser extent. Yet, organic cosolvents such as methanol are of major importance for reversed-phase chromatographic analyses and many other ESI-MS applications [6]. The current work closes this gap by exploring the behavior of methanol/water droplets. We demonstrate the occurrence of solvent segregation and differential evaporation. Ammonium ions are chosen as charge carriers, reflecting the prevalence of NH_4^+ in many ESI-MS solvent systems [2, 6]. While the droplets studied here do not contain any actual analyte molecules, the ejection of small cationic bioorganic species (e.g. drug molecules and metabolites) likely follows a field emission mechanism similar to that seen for NH_4^+.

4.2 Methods

MD simulations on charged nanodroplets were carried out based on C++ code developed in-house, similar to that used for earlier studies from our laboratory (Chapters 2, 3). Each droplet initially contained 1500 solvent molecules and 11 NH_4^+ ions. Five different water:methanol number ratios were tested, 100:0, 75:25, 50:50, 25:75, and 0:100. All simulations were carried out in a vacuum environment without imposing boundary conditions. The temporal evolution of the systems was simulated by integrating Newton's equations of motion using the Verlet algorithm [60, 61] with a time step of 2 fs. The classical SPCE/E model was employed for water, with an O-H bond distance of 1.0 Å and a H-O-H angle of 109.47° [62]. Methanol was modeled using the H1 framework [63] where the -CH_3 group (Me) is treated as a single Lennard Jones particle. In the H1 model the distances are 0.9451 Å for the O-H bond and 1.4246 Å for the Me-O bond. The Me-O-H angle is 108.53°. A N-H bond distance of 1.02 Å and a H-N-H angle of 109.47° was used for ammonium ions [64]. All bond lengths and angles were constrained using the SHAKE algorithm [65]. The solvent mixtures were initially subjected to Nose-Hoover thermalization [66, 67] at 320 K for 100 ps. The simulations were then switched to constant energy MD (at $T \approx 320$ K) for 1 ns, during which particle coordinates were extracted every 0.4 ps for analysis. Three to six independent trajectories were calculated for each solvent composition. The onset of the constant energy runs is referred to as $t = 0$ time point. Lennard Jones (LJ) parameters for water are $\sigma_{OO} = 3.166$ Å and $\varepsilon_{OO} = 0.6502$ kJ mol^{-1}, with charges $q_O = -0.8476\,e$ and $q_H = 0.4238\,e$ [62] LJ parameters for methanol are $\sigma_{OO} = 3.083$ Å and $\varepsilon_{OO} = 0.7308$ kJ mol^{-1}, $\sigma_{MeMe} = 3.861$

Å and $\varepsilon_{MeMe} = 0.7575$ kJ mol^{-1}, with charges $q_O = -0.728\,e$, $q_{Me} = 0.297\,e$ and $q_H = 0.431\,e$ [63]. LJ parameters for ammonium ions are $\sigma_{NN} = 3.45$ Å and $\varepsilon_{NN} = 0.7782$ kJ mol^{-1}, with charges $q_N = -0.8172\,e$ and $q_H = 0.4543\,e$ [64]. Mixing of these LJ parameters was performed according to $\sigma_{ij} = 0.5 \times \left(\sigma_{ii} + \sigma_{jj}\right)$ and $\varepsilon_{ij} = (\varepsilon_{ii}\varepsilon_{jj})^{0.5}$ [68]. Interactions between the hydrogen atoms of all three species were described purely based on the Coulomb potential. LJ potentials were truncated at 9.5 Å, whereas no cut-offs were employed for electrostatic interactions [14]. Electronic polarization effects have been shown to be quite important for modeling the behavior of large polarizable anions such as I$^-$ and Br$^-$. In comparison, these effects are almost negligible for small cations of the type studied here [54, 69-76]. Electronic polarization was thus not explicitly considered in this work, thereby simplifying the calculations and data analysis (Chapter 2). Radial distributions represent histograms that are plotted vs. distance r from the droplet center of mass, corrected for the $4\pi r^2$ surface area of individual bins to account for the spherical geometry. H-bonds were identified by employing the geometric criterion that the O-O distance has to be less than 3.5 Å, and simultaneously the angle between the O-O axis and one of the O-H covalent bonds has to be less than 35º [77]. This method was applied to all three types of H-bonds: water-water, water-methanol, and methanol-methanol. Solvent molecules were considered to be evaporated from the droplet when their distance from the overall center of mass was more than 35 Å. Simulations were run on SHARCNET (www.sharcnet.ca). Desktop computers were used for smaller test systems, code development, and trajectory analyses. Images of MD frames were rendered using VMD [78]. Sigmaplot 11 was employed for least-square fitting.

4.3 Results and Discussion

4.3.1 Overall Droplet Behavior

MD simulations on charged nanodroplets containing 1500 solvent molecules were carried out for various water/methanol compositions, including pure water and pure methanol. At t = 0 ns all systems exhibit a roughly spherical shape with some surface undulations (Figures 4.1a, 4.2a, 4.3a). Each of the droplets initially contained 11 NH_4^+ ions. Methanol and mixed water/methanol droplets are highly dynamic with relatively pronounced shape fluctuations during the simulation time window, numerous solvent evaporation events, and ejection of solvated ions (Figure 4.2, 4.3). In contrast, purely aqueous droplets maintain a more spherical geometry (Figure 4.1), solvent evaporation is less pronounced, and ion ejection is rare. All of these aspects will be discussed in more detail below.

The excess charge $Q = 11 \times 1.6 \times 10^{-19}$ C in our simulations was chosen to ensure that the initial droplets are close to the Rayleigh limit (equation 4.1), mimicking the size and charge regime encountered during the final stages of the ESI process [2, 79]. Calculating the ratio Q/Q_R requires the droplet radii r_0 to be determined. Consistent with earlier results [53, 54], the liquid/vapor boundary of the simulated systems is relatively diffuse, with sigmoidal transitions in the corresponding solvent radial distribution functions (Figure 4.4). r_0 values were estimated from the midpoints of these transitions (Chapter 2), resulting in $r_0 \approx 21$ Å for pure water (Figure 4.4a) and $r_0 \approx 28$ Å for pure methanol (Figure 4.4e). Values for mixed water/methanol systems fall in-between these two numbers. These data reflect the bulkier nature of the methyl group in CH_3-OH

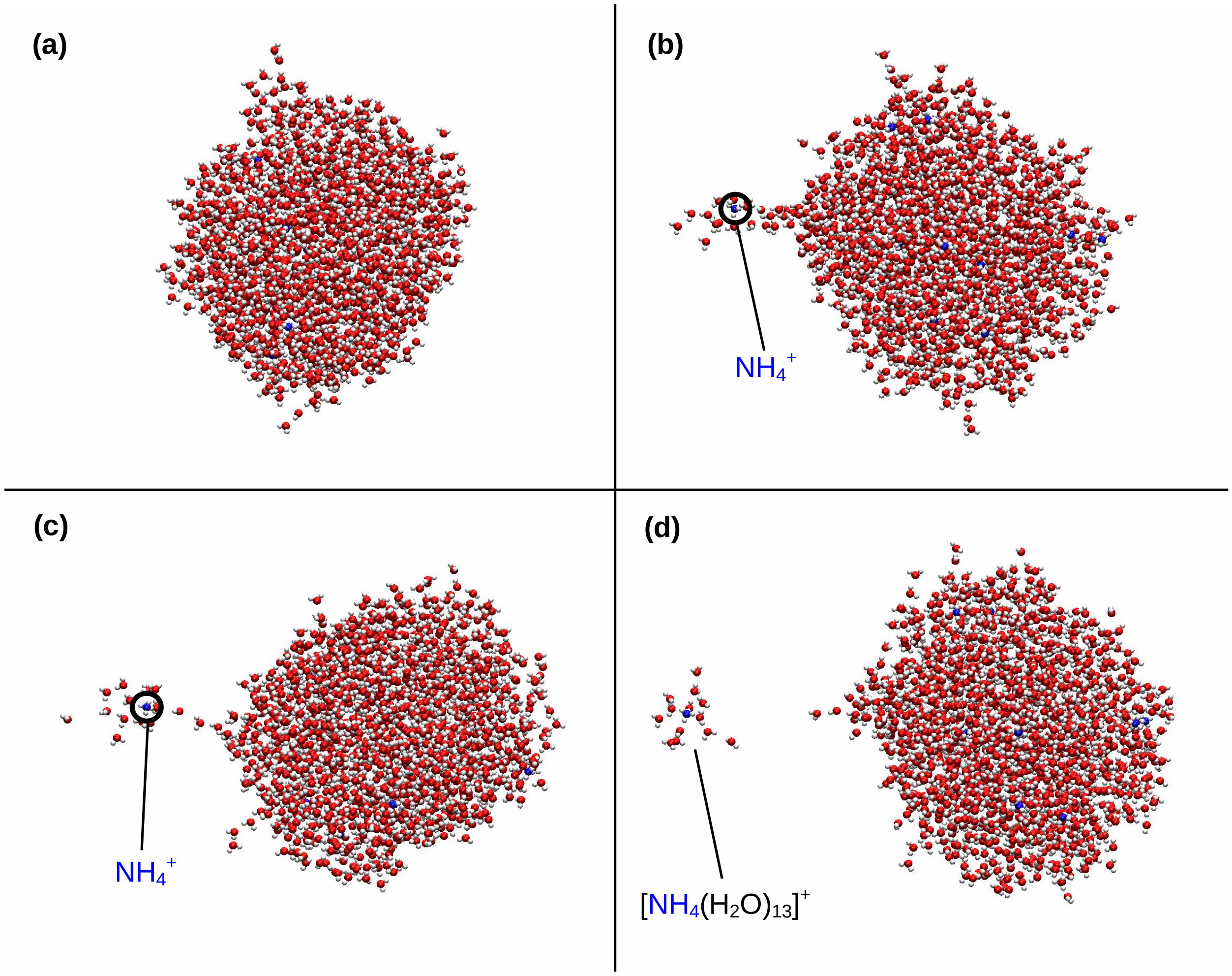

Figure 4.1. Snapshots taken from a MD trajectory of a nanodroplet initially containing 1500 water molecules and 11 ammonium ions. Hydrogen atoms are shown in white, oxygen in red, and nitrogen in blue. The time points shown correspond to (a) t = 0 ps, (b) t = 207 ps, (c) t = 212 ps, and (d) t = 219 ps. The location of the ammonium ion that is poised to be emitted is indicated in panels (b), (c). Also indicated in (d) is the overall composition of the ejected cluster.

relative to hydrogen in H-OH. The tabulated surface tension values γ of pure water and methanol are 0.0720 and 0.0225 N m^{-1}, respectively [80]. These bulk values are quite well reproduced by solvent models of the type used here [81, 82]. From equation 4.1 it follows that the charge on our aqueous droplets corresponds to Q/Q_R = 0.91, whereas the value for pure methanol is 1.06. We reiterate that the formation of these systems under experimental conditions starts with much larger droplets, which then undergo repeated cycles of evaporation and fission (see Introduction) [79]. Those earlier ESI steps are not accessible by MD simulations. Instead, this work deals with charged nanodroplets that represent the penultimate stage en route to the release of analyte ions into the gas phase [79].

Figure 4.1 depicts snapshots for the ejection of a solvated ammonium ion from a purely aqueous droplet. Formation of a surface protrusion that encloses a NH_4^+ ion (Figure 4.1b) is followed by a "bridged" arrangement where the departing cluster is connected to the parent droplet by a few H-bonded water molecules (Figure 4.1c). Subsequently the solvent bridge collapses, and the charged cluster is Coulombically propelled away from the residual droplet (Figure 4.1d). Qualitatively similar observations have been reported in previous MD studies [10, 11, 53, 54, 56, 57].

Formation of a transient solvent bridge between the departing charged cluster and the parent droplet is more extensive for methanol-containing droplets than for purely aqueous systems. Figure 4.2b shows a 50:50 system where a very long (~ 50 Å) protrusion involving both water and methanol has formed at the droplet surface. The gradual extension of this bridge is facilitated by electrostatic repulsion between the

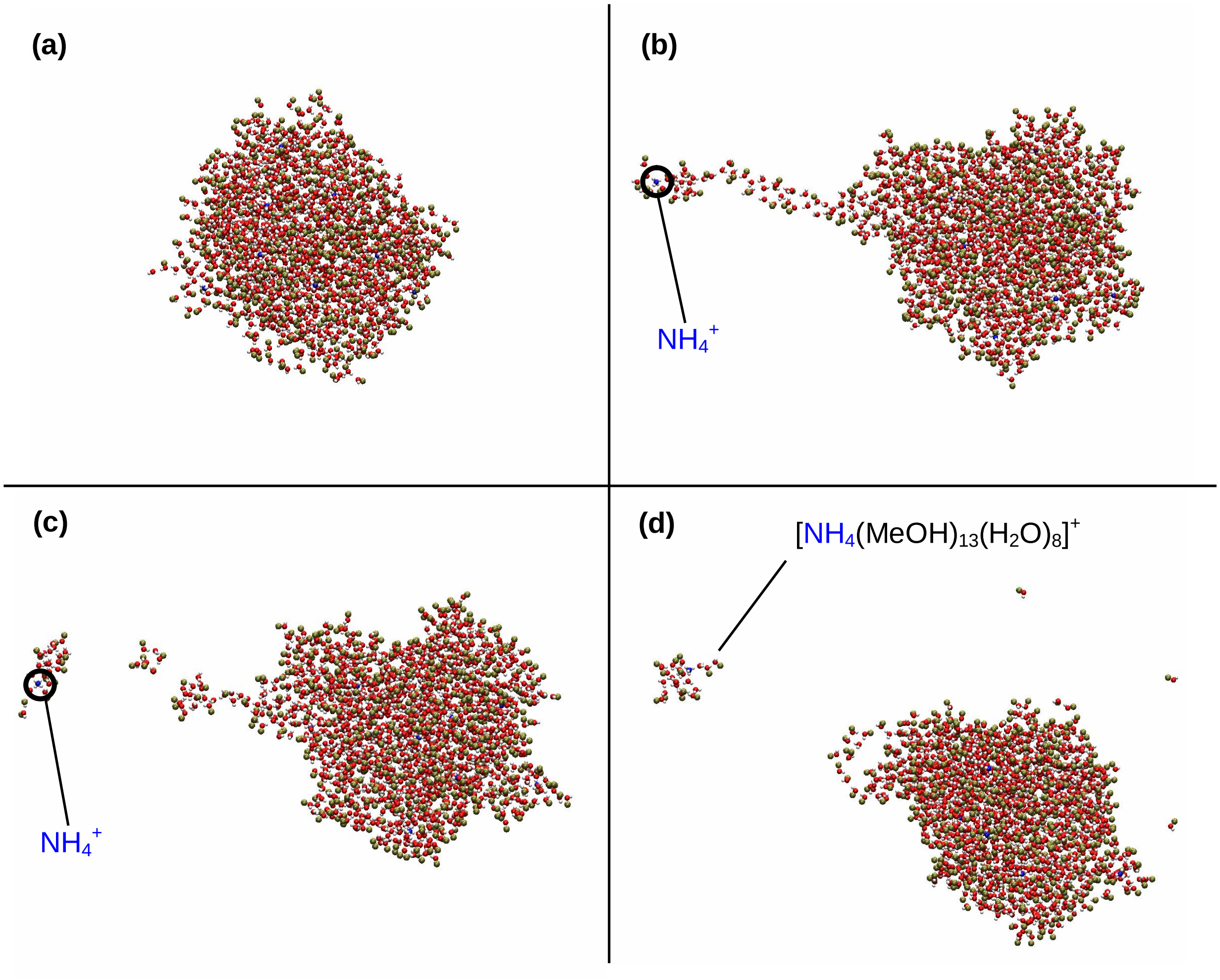

Figure 4.2. Snapshots taken from a MD trajectory of a nanodroplet initially containing 750 water, 750 methanol molecules and 11 ammonium ions. Color coding is as in Figure 4.1, with methyl groups shown in ochre. Time points: (a) *t* = 0 ps, (b) *t* = 802 ps, (c) *t* = 816 ps, and (d) *t* = 845 ps.

droplet and the solvated NH_4^+ at the protruding tip, up to a point where the bridge collapses (Figure 4.2c). The torn bridge elements then coalesce with the residual droplet, while the ejected cluster moves away from the center of mass (Figure 4.2d). A sequence of snapshots for an NH_4^+ emission event from a pure methanol droplet is depicted in Figure 4.3. The extent of bridging prior to secession (Figure 4.3c) is more pronounced than for the aqueous system (Figure 4.1c), but less than for the mixed cluster (Figure 4.2b). MD movies corresponding to Figures 4.1-4.3 can be found in the Supporting Information. The number of solvent molecules attached to the ejected ammonium ions is around ten to twenty for the various conditions studied here. Somewhat smaller solvation numbers (up to 8 H_2O per NH_4^+) have been found experimentally [34]. However, it is likely that those experiments involve additional solvent evaporation prior to detection, such that our results do not contradict those of ref. [34].

Earlier MD work has explored the surface energy *S* of nanometer-sized droplets [81, 83]. *S* represents the product of γ and surface area. It is instructive to consider the magnitude of ΔS associated with ejection of solvated ions. ΔS may be estimated as the difference in potential energy of the solvent before and after ejection [82]. We will focus on aqueous droplets (Figure 4.1), for which the overall potential energy has contributions from H_2O/H_2O, H_2O/NH_4^+, and NH_4^+/NH_4^+ interactions. The H_2O/H_2O contribution is dominant, amounting to -60,400 kJ mol^{-1}. The others are -7,700 and +3600 kJ mol^{-1}, respectively, with thermal fluctuations on the order of ± 1%. Dividing the H_2O/H_2O component by the number of solvent

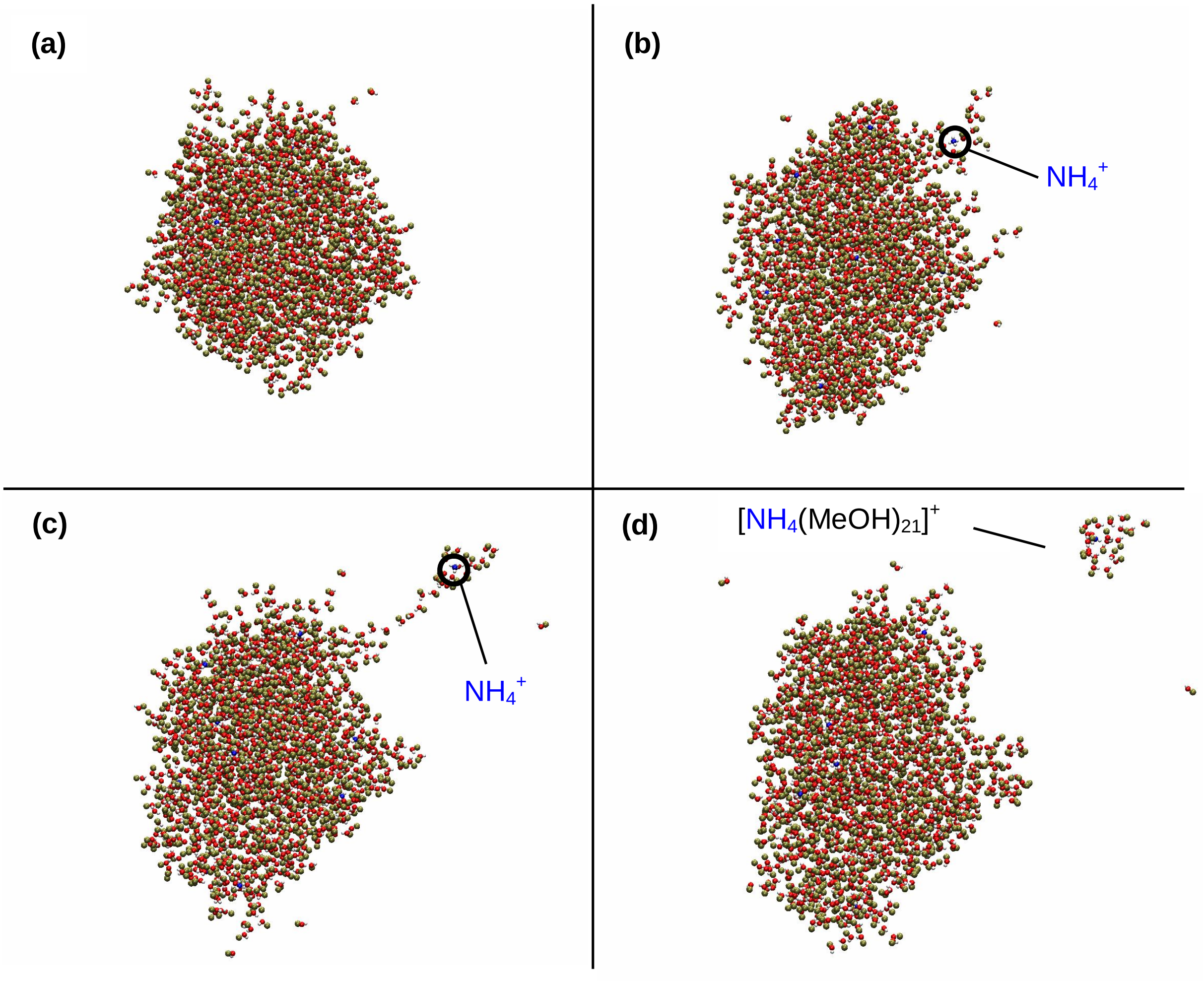

Figure 4.3. Snapshots taken from a MD trajectory of a nanodroplet initially containing 1500 methanol molecules and 11 ammonium ions. Color coding is as in Figures 4.1, 4.2. The time points shown correspond to (a) t = 0 ps, (b) t = 572 ps, (c) t = 645 ps, and (d) t = 663 ps.

molecules yields -60,400 kJ mol^{-1} : 1500 = -40.3 kJ mol^{-1}. This is close to the experimental enthalpy of condensation ($-\Delta_{vap}H$) [80], -43 kJ mol^{-1}, thus supporting the fidelity of our model. Ejection of a solvated ion from an aqueous nanodroplet (Figure 4.1) leads to a decrease in the overall NH_4^+/NH_4^+ interaction energy. However, only the H_2O/H_2O and H_2O/NH_4^+ contributions are pertinent for determining ΔS. Both of these remain virtually unchanged during ejection (data not shown), such that ΔS is exceedingly small. More specifically, based on the limited number of water molecules involved (~15, Figure 4.1b), it can be stated that ΔS will not exceed 15:1500 = 1%. ΔS may be larger for the methanol-containing droplets due to the greater number of solvent molecules that participate in ion ejection (e.g., Figure 4.2b). Unfortunately, energetic analyses of those situations are complicated by extensive solvent evaporation throughout the droplet lifetime (see below).

4.3.2 Droplet Structure

Distribution functions $P(r)$ were generated by tallying the radial position r of all droplet constituents into normalized histograms (Figure 4.4). This procedure was restricted to the first 200 ps of each trajectory for minimizing the effects of shape fluctuations and solvent evaporation. An overall trend towards larger r_0 with increasing methanol concentration has already been discussed above. It is interesting to note demixing of the two solvents, where methanol preferentially adopts positions more in the droplet periphery. This segregation is most pronounced for systems containing 25% methanol (Figure 4.4b), whereas the effect is diminished at higher concentrations

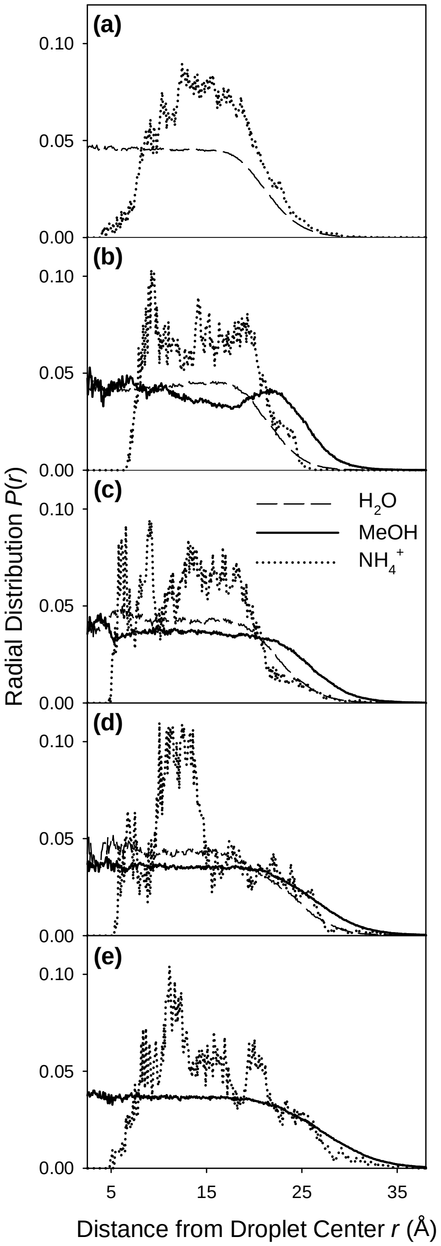

Figure 4.4. Radial distributions $P(r)$ for nanodroplets consisting of (a) 100% water, (b) 75% water / 25% methanol, (c) 50% water / 50% methanol, (d) 25% water / 75% methanol, and (e) 100% methanol. Dashed lines: oxygen of water, solid lines: methyl group of methanol, dotted lines: nitrogen of NH_4^+. Data were averaged over the first 200 ps of four 1 ns simulations for each panel.

(Figure 4.4c, d). Enrichment of methanol at the liquid/vapor interface has previously been observed in simulations of planar systems [84], and for small neutral clusters [85]. Consistent with our data (Figure 4.4), those previous studies [84, 85] reported that demixing is most pronounced at low methanol concentrations. Micro-immiscibilities were also found in MD studies and experimental investigations [86, 87] on bulk water/methanol solutions [88]. Notably, none of those earlier studies [84-88] explored the behavior of highly charged systems. Our results confirm that segregation also occurs for methanol/water droplets that are close to the Rayleigh limit. The surface enrichment of methanol seen in Figure 4.4 confirms the intuitive expectation that favorable water-water interactions (through H-bonding, see next section) can be maximized by preferentially gathering H_2O molecules in the center of the droplet. At the same time, methanol with its mildly hydrophobic -CH_3 group exhibits a higher affinity for the droplet surface, a phenomenon that is reminiscent of the behavior expected for partially nonpolar ESI analytes [6, 89, 90].

Similar to other cations [53, 54], NH_4^+ preferentially adopts radial positions towards the droplet interior, instead of being located at the solvent/vapor interface (dotted lines in Figure 4.4). This behavior is attributable to the more favorable solvation away from the surface, as mentioned in the Introduction and discussed in detail elsewhere (Chapter 3). Pure water droplets exhibit a simple bell-shaped $P(r)$ distribution for NH_4^+ (Figure 4.4a). In contrast, the NH_4^+ $P(r)$ profiles for methanol-containing droplets are more complex, reminiscent of data previously observed for other charge carriers [53].

4.3.3 Hydrogen Bonding and Solvent Evaporation

H-bonding is the main cohesive interaction for both water and methanol, whereas van der Waals interactions (modeled as LJ potentials) play a lesser role. In bulk water each molecule can donate ~2 H-bonds while also accepting ~2 H-bonds. In comparison, the propensity of methanol to act as donor and acceptor is compromised by the methyl group, resulting in less extensive H-bonding [91]. This behavior is reflected in the bulk vapor pressure values of 3.2 kPa and 16.9 kPa for water and methanol, respectively, at 25 °C [80].

As expected, the total number of H-bonds is highest for purely aqueous droplets. The 1500 waters form ~2700 interactions, corresponding to (2 × 2700) / 1500 = 3.6 H-bonds per H_2O molecule. Addition of methanol gradually lowers the total number of H-bonds down to ~1300 for droplets that are devoid of water (Figure 4.5a). In these pure methanol systems the number of H-bonds per solvent molecule is (2 × 1300) / 1500 = 1.7. Notably, these H-bonding numbers are in close agreement with bulk solution data, where 3.54 and 1.87 H-bonds per molecule were reported for neat water and methanol, respectively [91]. Thus, our data reveal that the presence of a solvent/vapor interface does not cause a marked reduction in the total number of H-bonds for the droplets, compared to bulk systems. Close inspection of Figures 4.2, 4.3 reveals that surface methanol molecules minimize the loss of H-bonding by pointing their $-CH_3$ group towards the vapor phase [84]. In the case of surface water one of the O-H bonds points into the vapor phase, such that only a single donor-type interaction is lost. This phenomenon is in line with dangling hydrogens detected by sum frequency spectroscopy [92] and in previous simulations (Chapter 2) [93].

The reduction in overall H-bonding with increasing methanol concentration diminishes cohesive interactions within the droplets. The resulting destabilization provides the mechanistic basis for the enhanced dynamics of methanol-containing droplets that was noted earlier (Figures 4.1-4.3). In addition, the reduced intermolecular contacts have a major effect on the solvent evaporation kinetics (Figure 4.5b). Only ~14 solvent molecules evaporate during the 1 ns simulation window from purely aqueous droplets, whereas ~180 molecules are lost for pure methanol. In the case of equimolar water/methanol mixtures the evaporation rate of methanol is *ca*. fourfold higher than that of water (Figure 4.5b). Most of these evaporation events correspond to the ejection of single solvent molecules from the droplet surface. Only on rare occasions two or three H-bonded molecules are ejected together.

The differential evaporation rates of organic/aqueous systems cause a significant water enrichment within mixed ESI nanodroplets. When extrapolating the magnitude of this effect from our 1 ns simulation window to typical lifetimes of larger droplets (μs to ms [33, 79]) the time-dependent changes in relative solvent composition can be expected to be dramatic. The existence of this effect has been assumed in several earlier studies [23, 43, 94]. Recent fluorescence spectroscopic investigations have directly monitored water enrichment within mixed aqueous/organic ESI droplets [95, 96]. Analogous phenomena may be operative in the case of ESI supercharging agents [97, 98].

Droplet destabilization due to the loss of H-bonding with increasing methanol concentration also has major implications for the emission of charge carriers. Solvated NH_4^+ get ejected from pure water droplets at a rate of ~0.5 ions per ns. This rate increases

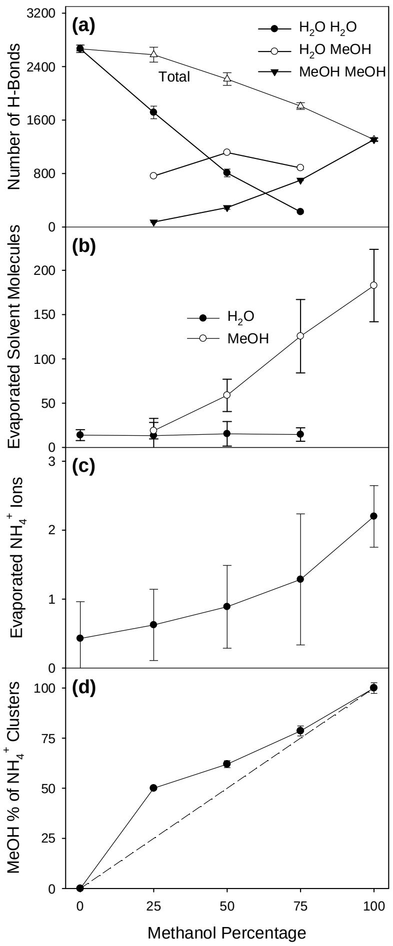

Figure 4.5. Several droplet parameters are plotted as a function of methanol percentage. (a) Number of different types of H-bonds (water-water, water-methanol, methanol-methanol). Also shown is the total number of H-bonds for each condition. Data were averaged for 3 time points (0 ps, 100 ps, and 200 ps) taken from a single MD run. (b) Number of evaporated solvent molecules after 1 ns. (c) Number of NH_4^+ ejected after 1 ns. (d) Composition of solvated NH_4^+ clusters after ejection. The dashed trend line represents a scenario where the offspring composition matches that of the parent droplet. Data in (b) - (d) correspond to average values obtained from three to six MD runs. Error bars represent one standard deviation.

by a factor of four for pure methanol (Figure 4.5c). As noted earlier, NH_4^+ ions are ejected as clusters encompassing roughly ten to twenty solvent molecules. The solvent composition of these small offspring clusters shows a certain degree of methanol enrichment relative to the parent droplet. This effect is most pronounced for a parent droplet methanol content of 25%, where the ejected charged clusters contain 50% methanol (Figure 4.5d).

4.3.4 Free Energy Profile for Ion Ejection

Further insights into the NH_4^+ dynamics and ejection are obtained when considering the ion free energy G as a function of distance r from the droplet center, where r serves as reaction coordinate. The following considerations are divided into two parts. We will first focus on $G(r)$ within the droplet interior, before considering $G(r)$ in the vicinity of the transition state.

The $P(r)$ ion distribution functions (Figure 4.4, dotted lines) are a manifestation of the metastable dynamics of NH_4^+ within the droplet. $P(r)\,dr$ denotes the probability of finding an ion at radial positions in the range r ... $(r + dr)$. We assume that an average potential energy ε can be assigned to an ion that is located at position r. $\varepsilon(r)$ includes all Coulombic and LJ interactions with other ions and solvent molecules. $P(r)$ is given by a Boltzmann distribution [99, 100] with

$$P(r)dr = \frac{1}{Z}\exp\left(-\frac{\varepsilon(r)}{k_B T}\right)dW(r) \tag{4.3}$$

where $dW(r)$ represents the number of energetically equivalent microstates in the range r ... $(r + dr)$. Z is the partition function. With the density of states $D(r) = dW(r) / dr$ equation 4.3 can be rewritten as

$$P(r)dr = \frac{D(r)}{Z}\exp\left(-\frac{\varepsilon(r)}{k_B T}\right)dr \tag{4.4}$$

Rearrangements leads to

$$P(r) = \frac{1}{Z}\exp\left(-\frac{G(r)}{k_B T}\right) \tag{4.5}$$

where $G(r)$ represents free energy of the ion inside the droplet, with energetic and entropic contributions according to

$$G(r) = \varepsilon(r) - TS(r) \tag{4.6}$$

The entropy term is given by $S(r) = k_B \ln D(r)$, and the partition function is

$$Z = \int_{r=0}^{\infty} \exp\left(-\frac{G(r)}{k_B T}\right)dr \tag{4.7}$$

thereby ensuring normalization of $P(r)$ to unity.

Determining $G(r)$ is most straightforward for aqueous droplets with their simple unimodal distribution function (Figure 4.4a), and hence we will focus on this particular case. $P(r)$ is well described by a Gaussian function

$$y = a\exp\left(-\frac{1}{2}\left[\frac{r - r_{eq}}{b}\right]^2\right) \tag{4.8}$$

with a = 0.0833, b = 4.89 Å, and a quasi-equilibrium position of r_{eq} = 14.8 Å (Figure 4.6a). Equating (4.5) and (4.8), and noting that $a = Z^{-1}$ leads to

$$\frac{G(r)}{k_B T} = \frac{1}{2}\left[\frac{r - r_{eq}}{b}\right]^2 \tag{4.9}$$

Unit conversion from J to J mol^{-1} , using $R = k_B \times N_A$ results in

$$G(r) = \frac{RT}{2}\left[\frac{r - r_{eq}}{b}\right]^2 \tag{4.10}$$

with the gas constant R = 8.314 J K^{-1} mol^{-1}. Equation 4.10 reveals that the dynamics of NH_4^+ within the nanodroplet interior are governed by a parabolic free energy profile (solid line in Figure 4.6b).

We will now consider the appearance of $G(r)$ in the transition state region. Ion ejection requires crossing of an activation barrier with $\Delta G^* = G(r_{TS}) - G(r_{eq})$ where r_{TS} denotes the location of the transition state [33]. The original formulation of the IEM assumed that the transition state corresponds to a configuration where a solvated ion has separated and is located a certain distance above the surface of a spherical parent droplet [33, 36]. The current work, as well as earlier investigations [10, 11, 37, 53, 54, 56, 57] have refined this view by noting that ion ejection involves distortion of the parent droplet along with formation of a transient solvent bridge prior to secession (Figures 4.1-4.3). Formation of such a protrusion does not always lead to successful ion ejection. Instead, our simulations reveal that configurations as in Figure 4.1b can also collapse back onto the parent droplet.

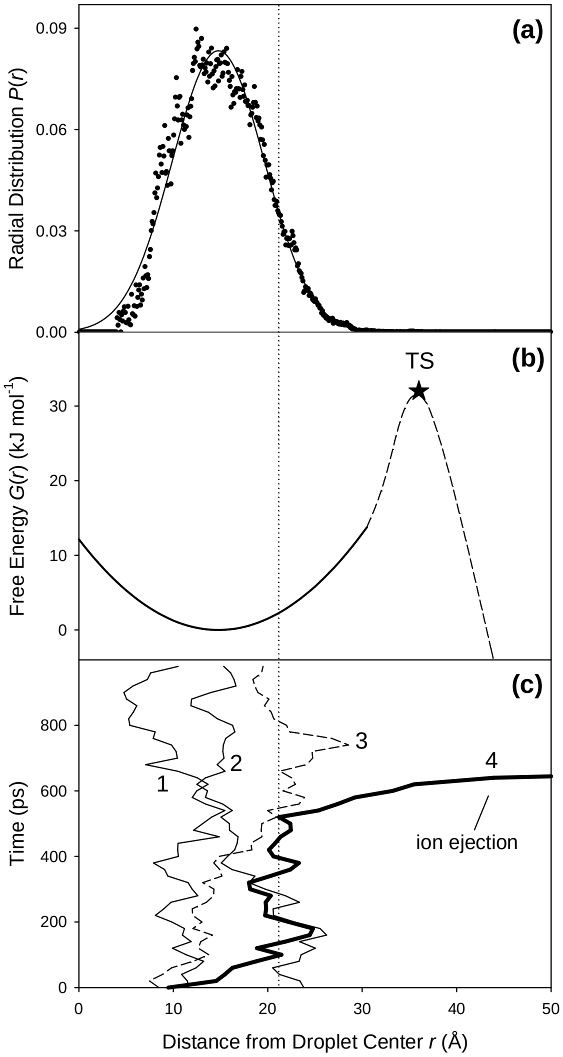

Figure 4.6. Various aspects of the NH_4^+ dynamics. (a) Radial distribution function $P(r)$ of ammonium ions (taken from Figure 4.4a), with a fitted Gaussian curve (solid line, equation 4.8). (b) Free energy profile $G(r)$. The solid line depicts $G(r)$ for ion motion in the droplet interior (equation 4.10). Also shown (dashed line) is an extension of $G(r)$ towards and beyond the transition state (TS, marked with an asterisk). (c) Radial position of four selected ions (1-4) vs. time. Ion 4 gets ejected from the droplet. The vertical dotted line indicates the approximate droplet radius r_0.

The transition state r_{TS} reflects the critical protrusion length where the emission probability reaches 0.5 [101]. Even without performing a detailed mapping analysis, we can conclude that r_{TS} is close to the linear dimension of a typical protrusion (e.g., Figure 4.1b, c), measured from the droplet center. For the aqueous droplets considered here this corresponds to $r_{TS} \approx 35$ Å.

For estimating the activation barrier height we recall that ion ejection can be treated as a first-order process [33] where the number of bound NH_4^+ ions $N(t)$ decreases according to

$$\frac{N(t)}{N_0} = \exp(-kt) \tag{4.11}$$

with $N_0 = 11$ and a rate constant k. For aqueous systems with an ejection rate of 0.5 ions per ns (Figure 4.5c) equation 4.11 provides a value of $k = 4.7 \times 10^7$ s^{-1}. This corresponds to an activation energy estimate of $\Delta G^* \approx 32$ kJ mol^{-1} (equation 4.2). In Figure 4.6b this barrier at $r_{TS} \approx 35$ Å is indicated by an asterisk. The dashed line in Figure 4.6b represents a spline extrapolation suggesting a possible shape of the $G(r)$ profile in the vicinity of the transition state. Application of our approach to methanol droplets with their elevated ejection rate of 2 ions per ns (Figure 4.5c) leads to a lower activation barrier of $\Delta G^* \approx 28$ kJ mol^{-1}. Our estimate of $\Delta G^* \approx 32$ kJ mol^{-1} for aqueous droplets is in quite close agreement with the value of 38 kJ mol^{-1} proposed in the original IEM paper [33]. Barriers on the order of 27 kJ mol^{-1} were reported in previous MD simulations for ion escape from smaller aqueous droplets [56, 57].

The free energy profile of Figure 4.6b allows the ion dynamics to be treated as a one-dimensional diffusion process, with escape from a metastable state via thermally activated barrier crossing. This situation is analogous to kinetic phenomena for other complex systems [100, 102, 103]. Figure 4.6c illustrates $r(t)$ trajectories of four selected ammonium ions. Ions 1 and 2 undergo Brownian motion [102] relatively close to the bottom of the parabolic $G(r)$ basin for much of the simulation window. Ion 3 initially resides close to the droplet center. It then diffuses towards the liquid/vapor interface, forms a transient surface protrusion around t = 700 ps, but ultimately moves back towards the interior. Thus, trajectory 3 represents an unsuccessful ejection event. Ion 4 starts at a radial position around 10 Å. Subsequently, it moves towards the water/vapor interface where it resides for the next 400 ps. At $t \approx 500$ ps the ion gets entrapped in a surface protrusion, crosses the barrier, and is ejected from the droplet.

4.4 Conclusions

This work examined the behavior of mixed water/methanol nanodroplets close to the Rayleigh limit. The presence of methanol destabilizes the overall droplet structure by reducing the extent of H-bonding. This effect provides the basis for the widespread use of organic cosolvents in ESI-MS, where rapid solvent evaporation and droplet fission are prerequisites for the efficient production of gas phase analyte ions [6, 79].

Nanodroplets containing a relatively low methanol concentration (e.g., 25%, Figure 4.4b) exhibit significant demixing, with an outer droplet layer that is mostly organic. While not explicitly investigated here, this segregation should favor partitioning of analytes according to their hydrophobicity. Past studies have suggested that surface affinity represents a major determinant of the ESI efficiency, even in homogeneous solvent systems [6, 89, 90]. In future work it will be interesting to explore how the presence of an organic outermost droplet layer around an aqueous core affects the analyte behavior.

Our simulations reveal that differential solvent evaporation leads to gradual water enrichment in mixed aqueous/organic droplets. Our findings support the view that late ESI droplets consist almost exclusively of the least volatile solvent component [23, 43, 94]. However, the situation could be different under nanoESI conditions where the initial droplet radii are much smaller [29, 104]. The resulting reduced droplet lifetime and lower number of evaporation/fission cycles may favor the retention of organic solvents in the final droplets.

The diffusive ion dynamics in the interior of aqueous droplets are governed by a parabolic free energy profile. Ion ejection corresponds to thermally activated barrier crossing. Following previous IEM studies [33, 36, 37, 39] we analyzed ion ejection using transition state theory. Future work is required to determine if the use of a single barrier is adequate. Alternatively, bridged arrangements as in Figures 4.1-4.3 might involve additional metastable states. Also, instead of interpreting ion ejection using transition state theory, one might consider the application of Kramers' framework [102]. Kramers' rate expression applies to the diffusive escape from a metastable minimum. Its pre-exponential factor takes into account friction effects, reflecting drag forces experienced by Brownian particles as they move within a viscous medium. Computational and experimental studies on the viscosity dependence of ion ejection could yield additional insights into the properties of the transition barrier.

Earlier studies on large droplets clearly distinguished between Rayleigh fission on one hand, and charge carrier ejection via IEM on the other [33, 36]. Figures 4.1-4.3 reveal that ion ejection from a nanodroplet morphologically resembles the asymmetric Rayleigh fission of larger droplets [45-48]. Both types of events occur when the droplet charge is close to Q_R [2, 33]. One may ask, then, whether a mechanistic distinction between the two processes remains meaningful for the size regime considered here. In other words, can an *"evaporated" ion with its solvent shell* also be interpreted as a (very small) *charged progeny droplet*? Progeny droplets generated during typical Rayleigh fission events contain ~2% of the parent mass and ~15% of the charge [79]. These values are close to those observed here, although Rayleigh fission typically involves multiple progeny droplets whereas the ejection of single ions is observed here. The latter difference can be rationalized by considering the very small number (and resulting discrete nature) of charge carriers in our nanodroplets. Losing 1/11 of the droplet charge corresponds to a substantial (9%) reduction, which lowers the driving force for subsequent ion ejection. One interesting aspect for the issue at hand is the observation that ion emission from charged nanodroplets is associated with a major activation barrier (Figure 4.6b). The presence of such a barrier is a salient IEM feature [33-37], whereas droplet fission by the Rayleigh mechanism is thought to proceed in a barrier-free fashion [1, 19-21]. Based on this criterion it would appear that the ion ejection observed here is more appropriately interpreted as IEM-like field emission, rather than Rayleigh fission. Nonetheless, the dividing line between the two mechanisms becomes somewhat blurred for droplets in the nano-regime, especially when the discussion is based on morphological features. The absence of barrier-free disintegration events in the current simulations may be attributable to the lack of collective shape fluctuations (such as prolate-oblate oscillations) in the initial droplets [1, 19]. Additional work will be required to explore the effects of such collective oscillations, which might represent an important determinant for the behavior of real ESI droplets.

It is hoped that future extensions of this study will provide further insights into the behavior of charged solvent droplets under ESI conditions. NH_4^+ ions were considered here because they represent a commonly used solvent additive in ESI-MS. From an analytical perspective, NH_4^+ ejection is of limited interest. However, it seems likely that ESI of small bioorganic species which exist as preformed ions will follow a mechanism similar to that discussed above for NH_4^+. Work to test this prediction is currently in progress. We are also exploring the behavior of much larger species, all the way to intact proteins, where a very different mechanism is expected. Also, the droplets considered here do not contain any counterions. Simulations involving both cations and anions are underway, with the aim of gaining insights into possible ion pairing and cluster formation [29]. The results of those investigations will be reported elsewhere.

4.5 References

1. Rayleigh, L., *On the Equilibrium of Liquid Conducting Masses charged with Electricity.* Phil. Mag., 1882. **14**: p. 184-186.

2. Kebarle, P. and U.H. Verkerk, *Electrospray: From Ions in Solutions to Ions in the Gas Phase, What We Know Now.* Mass Spectrom. Rev., 2009. **28**: p. 898-917.

3. Hogan, C.J. and J.F. de la Mora, *Tandem ion mobility-mass spectrometry (IMS-MS) study of ion evaporation from ionic liquid-acetonitrile nanodrops.* Phys. Chem. Chem. Phys., 2009. **11**: p. 8079-8090.

4. Cole, R.B., *Electrospray Ionization Mass Spectrometry*. 1997, New York: John Wiley & Sons, Inc.

5. Van Berkel, G.J. and V. Kertesz, *Electrochemistry/spray Ion Source.* Anal. Chem., 2007. **79**: p. 5511-5520.

6. Cech, N.B. and C.G. Enke, *Practical Implication of Some Recent Studies in Electrospray Ionization Fundamentals.* Mass Spectrom. Rev., 2001. **20**: p. 362-387.

7. Giglio, E., B. Gervais, J. Rangama, B. Manil, and B.A. Huber, *Shape deformations of surface-charged microdroplets.* Phys. Rev. E, 2008. **77**: p. 036319.

8. Feng, X., M.J. Bogan, and G.R. Agnes, *Coulomb Fission Event Resolved Progeny Droplet Production from Isolated Evaporating Methanol Droplets.* Anal. Chem., 2001. **73**: p. 4499-4507.

9. Tang, K. and R.D. Smith, *Theoretical prediction of charged droplet evaporation and fission in electrospray ionization.* Int. J. Mass Spectrom., 1999. **185/186/187**: p. 97-105.

10. Ichiki, K. and S. Consta, *Disintegration Mechanisms of Charged Aqueous Nanodroplets Studied by Simulations and Analytical Models.* J. Phys. Chem. B, 2006. **110**: p. 19168-19175.

11. Marginean, I., V. Znamenskiy, and A. Vertes, *Charge Reduction in Electrosprays: Slender Nanojets as Intermediates.* J. Phys. Chem. B, 2006. **110**: p. 6397-6404.

12. Storozhev, V.B. and E.N. Nikolaev, *Computer simulations of the fission process of charged nanometre droplets.* Phil. Mag., 2004. **84**: p. 157-171.

13. Hogan, C.J., J.A. Carroll, H.W. Rohrs, P. Biswas, and M.L. Gross, *Combined Charged Residue-Field Emission Model of Macromolecular Electrospray Ionization.* Anal. Chem., 2009. **81**: p. 369-377.

14. Luedtke, W.D., U. Landmann, Y.-H. Chiu, D.J. Levandier, R.A. Dressler, S. Sok, and M.S. Gordon, *Nanojets, Electrospray and Ion Field Evaporation: Molecular Dynamics Simulations and Laboratory Experiments.* J. Phys. Chem. A, 2008. **112**: p. 9628-9649.

15. Labowsky, M., *A model for solvated ion emission from electrospray droplets.* Rapid Commun. Mass Spectrom., 2010. **24**: p. 3079-3091.

16. Fenn, J.B., *Electrospray Wings for Molecular Elephants (Nobel Lecture).* Angew. Chem. Int. Ed., 2003. **42**: p. 3871-3894.

17. Pan, P. and S.A. McLuckey, *Electrospray Ionization of Protein Mixtures at Low pH.* Anal. Chem., 2003. **75**: p. 1491-1499.

18. Gu, W., P.E. Heil, H. Choi, and K. Kim, *Comprehensive model for fine Coulomb fission of liquid droplets charged to Rayleigh limit.* Appl. Phys. Lett., 2007. **91**: p. 064104.

19. Konermann, L., *A Simple Model for the Disintegration of Highly Charged Solvent Droplets during Electrospray Ionization.* J. Am. Soc. Mass Spectrom., 2009. **20**: p. 496-506.

20. Last, I., Y. Levy, and J. Jortner, *Beyond the Rayleigh instability limit for multicharged finite systems: From fission to Coulomb explosion.* Proc. Natl. Acad. Sci. U.S.A., 2002. **99**: p. 9107-9112.

21. Lyalin, A.G., O.I. Obolensky, and W. Greiner, *Stability of Charged Atomic Clusters.* Rom. Rep. Phys., 2007. **59**: p. 499-513.

22. Dole, M., L.L. Mack, R.L. Hines, R.C. Mobley, L.D. Ferguson, and M.B. Alice, *Molecular beams of macroions.* J. Chem. Phys., 1968. **49**: p. 2240-2249.

23. Iavarone, A.T. and E.R. Williams, *Mechanism of Charging and Supercharging Molecules in Electrospray Ionization.* J. Am. Chem. Soc., 2003. **125**: p. 2319-2327.

24. de la Mora, F.J., *Electrospray Ionization of large multiply charged species proceeds via Dole's charged residue mechanism.* Anal. Chim. Acta, 2000. **406**: p. 93-104.

25. Felitsyn, N., M. Peschke, and P. Kebarle, *Origin and number of charges observed on multiply-protonated native proteins produced by ESI.* Int. J. Mass Spectrom. Ion Proc., 2002. **219**: p. 39-62.

26. Nesatyy, V.J. and M.J.-F. Suter, *On the conformation-dependent neutralization theory and charging of individual proteins and their non-covalent complexes in the gas phase.* J. Mass Spectrom., 2004. **39**: p. 93-97.

27. Kaltashov, I.A. and A. Mohimen, *Estimates of Protein Surface Area in Solution by Electrospray Ionization Mass Spectrometry.* Anal. Chem., 2005. **77**: p. 5370-5379.

28. Heck, A.J.R. and R.H.H. Van den Heuvel, *Investigation of intact protein complexes by mass spectrometry.* Mass Spectrom. Rev., 2004. **23**: p. 368-389.

29. Juraschek, R., T. Dulcks, and M. Karas, *Nanoelectrospray - More than just a Minimized-Flow Electrospray Ionization Source.* J. Am. Soc. Mass Spectrom., 1999. **10**: p. 300-308.

30. Pan, J., K. Xu, X. Yang, W.Y. Choy, and L. Konermann, *Solution-phase chelators for suppressing nonspecific protein-metal interactions in electrospray mass spectrometry.* Anal. Chem., 2009. **81**: p. 5008-5015.

31. Sun, J., E.N. Kitova, N. Sun, and J.S. Klassen, *Method for Identifying Nonspecific Protein-Protein Interactions in Nanoelectrospray Ionization Mass Spectrometry.* Anal. Chem., 2007. **79**: p. 8301-8311.

32. Peschke, M., U.H. Verkerk, and P. Kebarle, *Features of the ESI Mechanism that Affect the Observation of Multiply Charged Noncovalent Protein Complexes and the Determination of the Association Constant by the Titration Method.* J. Am. Soc. Mass Spectrom., 2004. **15**: p. 1424-1434.

33. Iribarne, J.V. and B.A. Thomson, *On the evaporation of small ions from charged droplets.* J. Chem. Phys., 1976. **64**: p. 2287-2294.

34. Thomson, B.A. and J.V. Iribarne, *Field induced ion evaporation from liquid surfaces at atmospheric pressure.* J. Chem. Phys., 1979. **71**: p. 4451.

35. Gamero-Castaño, M. and F. de la Mora, *Kinetics of small ion evaporation from the charge and mass distribution of multiply charged clusters in electrosprays.* J. Mass Spectrom., 2000. **35**: p. 790-803.

36. Tang, L. and P. Kebarle, *Dependence of ion intensity in electrospray mass spectrometry on the concentration of the analytes in the electrosprayed solution.* Anal. Chem., 1993. **65**: p. 3654-3668.

37. Labowsky, M., J.B. Fenn, and J. Fernandez de la Mora, *A continuum model for ion evaporation from a drop: effect of curvature and charge on ion solvation energy.* Anal. Chim. Acta, 2000. **406**: p. 105-118.

38. Loscertales, I.G. and J.F. de la Mora, *Experiments on the kinetics of field evaporation of small ions from droplets.* J. Chem. Phys., 1995. **103**: p. 5041-5060.

39. Wang, G. and R.B. Cole, *Charged residue versus ion evaporation for formation of alkali metal halide clusters ions in ESI.* Anal. Chim. Acta, 2000. **406**: p. 53-65.

40. Spencer, E.A.C., T. Ly, and R.K. Julian, *Formation of the serine octamer: Ion evaporation or charge residue?* Int. J. Mass Spectrom., 2008. **270**: p. 166-172.

41. Nguyen, S. and J.B. Fenn, *Gas-phase ions of solute species from charged droplets of solutions.* Proc. Natl. Acad. Sci. U.S.A., 2007. **104**: p. 1111-1117.

42. Fenn, J.B., J. Rosell, and C.K. Meng, *In Electrospray Ionization, How Much Pull Does an Ion Need to Escape Its Droplet Prison.* J. Am. Soc. Mass Spectrom., 1997. **8**: p. 1147-1157.

43. Samalikova, M. and R. Grandori, *Protein Charge-State Distributions in Electrospray-Ionization Mass Spectrometry Do Not Appear To Be Limited by the Surface Tension of the Solvent.* J. Am. Chem. Soc., 2003. **125**: p. 13352-13353.

44. Smith, J.N., R.C. Flagan, and J.L. Beauchamp, *Droplet Evaporation and Discharge Dynamics in Electrospray Ionization.* J. Phys. Chem. A, 2002. **106**: p. 9957-9967.

45. Gomez, A. and K. Tang, *Charge and fission of droplets in electrostatic sprays.* Phys. Fluids, 1994. **6**: p. 404-414.

46. Duft, D., T. Achtzehn, R. Muller, B.A. Huber, and T. Leisner, *Coulomb fission: Rayleigh jets from levitated microdroplets.* Nature, 2003. **421**: p. 128.

47. Li, D., M. Marquez, and Y. Xia, *Capturing electrified nanodroplets under Rayleigh instability by coupling electrospray with a sol–gel reaction.* Chem. Phys. Lett., 2007. **445**: p. 271-275.

48. Nemes, P., I. Marginean, and A. Vertes, *Spraying Mode Effect on Droplet Formation and Ion Chemistry in Electrosprays.* Anal. Chem., 2007. **79**: p. 3105-3116.

49. Zweir, T.S., *The structure of protonated water clusters.* Science, 2004. **304**: p. 1119-1120.

50. Shin, J.-W., N.I. Hammer, E.G. Diken, M.A. Johnson, R.S. Walters, T.D. Jaeger, M.A. Duncan, R.A. Christie, and K.D. Jordan, *Infrared Signature of Structures Associated with the H+(H2O)n (n = 6 to 27) Clusters.* Science, 2004. **304**: p. 1137-1140.

51. O'Brien, J.T., J.S. Prell, M.F. Bush, and E.R. Williams, *Sulfate Ion Patterns Water at Long Distance.* J. Am. Chem. Soc., 2010. **132**: p. 8248-8249.

52. McQuinn, K., F. Hof, and J.S. McIndoe, *Direct observation of ion evaporation from a triply charged nanodroplet.* Chem. Commun., 2007. **2007**: p. 4099-4101.

53. Znamenskiy, V., I. Marginean, and A. Vertes, *Solvated Ion Evaporation from Charged Water Droplets.* J. Phys. Chem. A, 2003. **107**: p. 7406-7412.

54. Caleman, C. and D. van der Spoel, *Evaporation from water clusters containing singly charged ions.* Phys. Chem. Chem. Phys., 2007. **9**: p. 5105-5111.

55. Consta, S., *Manifestation of Rayleigh Instability in Droplets Containing Multiply Charged Macroions.* J. Phys. Chem. B, 2010. **114**: p. 5263–5268.

56. Consta, S., *Fragmentation reactions of charged aqueous clusters.* J. Mol. Struct. (Theochem), 2002. **591**: p. 131-140.

57. Consta, S., K.R. Mainer, and W. Novak, *Fragmentation mechanisms of aqueous clusters charged with ions.* J. Chem. Phys., 2003. **119**: p. 10125-10132.

58. Konermann, L., *A Minimalist Model for Exploring Conformational Effects on the Electrospray Charge State Distribution of Proteins.* J. Phys. Chem. B, 2007. **111**: p. 6534-6543.

59. Patriksson, A., E. Marklund, and D. van der Spoel, *Protein Structures under Electrospray Conditions.* Biochemistry, 2007. **46**: p. 933-945.

60. Verlet, L., *Computer "Experiments" on Classical Fluids. I. Thermodynamical Properties of Lennard-Jones Molecules.* Phys. Rev., 1967. **159**: p. 98-103.

61. Frenkel, D. and B. Smit, *Understanding Molecular Simulations: From Algorithms To Applications*. 1996, San Diego: Academic Press.

62. Berendsen, H.J.C., J.R. Grigera, and T.P. Straatsma, *The missing term in effective pair potentials.* J. Phys. Chem., 1987. **91**: p. 6269-6271.

63. Haughney, M., M. Ferrario, and I.R. McDonald, *Molecular-Dynamics simulation of liquid methanol.* J. Phys. Chem., 1987. **91**: p. 4934-4940.

64. Chang, T.-M. and L.X. Dang, *On rotational dynamics of an NH4+ ion in water.* J. Chem. Phys., 2003. **118**: p. 8813-8820.

65. Forester, T.R. and W. Smith, *SHAKE, Rattle and Roll: Efficient Constraint Algorithms for Linked Rigid Bodies.* J. Comput. Chem., 1998. **19**: p. 102-111.

66. Nose, S., *A molecular dynamics method for simulations in the canonical ensemble.* Mol. Phys., 1984. **52**: p. 255-268.

67. Hoover, W.G., *Canonical dynamics: Equilibrium phase-space distributions.* Phys. Rev. A, 1985. **31**: p. 1695-1697.

68. Delhommelle, J. and P. Millie, *Inadequacy of the Lorentz-Berthelot combining rules for accurate predictions of equilibrium properties by molecular simulation.* Mol. Phys., 2001. **99**: p. 619-625.

69. Benjamin, I., *Theoretical study of ion solvation at the water liquid–vapor interface.* J. Chem. Phys., 1991. **95**: p. 3698-3709.

70. Jungwirth, P. and D.J. Tobias, *Molecular structure of salt solutions: A new view of the interface with implications for heterogeneous atmospheric chemistry.* J. Phys. Chem. B, 2001. **105**: p. 10468-10472.

71. Wick, C.D. and L.X. Dang, *Recent advances in understanding transfer ions across aqueous interfaces.* Chem. Phys. Lett., 2008. **458**: p. 1-5.

72. Knipping, E.M., M.J. Lakin, K.L. Foster, P. Jungwirth, D.J. Tobias, R.B. Gerber, D. Dabdub, and B.J. Finlayson-Pitts, *Ion-enhanced interfacial chemistry on aqueous NaCl aerosols.* Science, 2000. **288**: p. 301-306.

73. Burnham, C.J., M.K. Petersen, T.J.F. Day, S.S. Iyengar, and G.A. Voth, *The properties of ion-water clusters. II. Solvation structures of Na+, Cl-, and H+ clusters as a function of temperature.* J. Chem. Phys., 2006. **124**: p. 024327.

74. Tian, C.S. and Y.R. Shen, *Structure and Charging of Hydrophobic Material/Water Interfaces Studied by Phase-Sensitive Sum-Frequency Vibrational Spectroscopy.* Proc. Natl. Acad. Sci. U.S.A., 2009. **106**: p. 15148-15153.

75. Petersen, P.B. and R.J. Saykally, *Is the liquid water surface basic or acidic? Macroscopic vs. molecular-scale investigations.* Chem. Phys. Lett., 2008. **458**: p. 255-261.

76. Douady, J., F. Calvo, and F. Spiegelman, *Structure, stability and infrared spectroscopy of* $(H_2O)_nNH^{4+}$ *clusters: A theoretical study at zero and finite temperature.* J. Chem. Phys., 2008. **129**: p. 154305.

77. Chandler, D., *Interfaces and the driving force of hydrophobic assembly.* Nature, 2005. **437**: p. 640-647.

78. Humphrey, W., A. Dalke, and K. Schulten, *VMD - Visual Molecular Dynamics.* J. Mol. Graphics, 1996. **14**: p. 33-38.

79. Kebarle, P. and L. Tang, *From ions in solution to ions in the gas phase: The mechanism of electrospray mass spectrometry.* Anal. Chem., 1993. **65**: p. 972A-986A.

80. Lide, D.R., *CRC Handbook of Chemistry and Physics*. 82nd ed. 2001, Boca Raton, London, New York, Washington: CRC Press.

81. Yuet, P.K. and D. Blankenschtein, *Molecular Dynamics Simulation Study of Water Surfaces: Comparison of Flexible Water Models.* J. Phys. Chem. B, 2010. **114**: p. 13786-13795.

82. Bahadur, R., L.M. Russell, and S. Alavi, *Surface tensions in NaCl-water-air systems from MD simulations.* J. Phys. Chem. B, 2007. **111**: p. 11989-11996.

83. Bahadur, R. and L.M. Russel, *Effect of Surface Tension from MD Simulations on Size-Dependent Deliquescence of NaCI Nanoparticles.* Aerosol Sci. Tech., 2008. **42**: p. 369-376.

84. Chang, T.-M. and L.X. Dang, *Liquid-vapor interface of methanol-water mixtures: A molecular dynamics study.* J. Phys. Chem. B, 2005. **109**: p. 5759-5765.

85. Brodskaya, E.N., *Molecular-dynamic simulation of mixed water-methanol clusters: 1. Local structure.* Colloid J., 2001. **63**: p. 5-9.

86. Guo, J.H., Y. Luo, A. Augustsson, S. Kashtanov, J.E. Rubensson, D.K. Shuh, H. Agren, and J. Nordgren, *Molecular structure of alcohol-water mixtures.* Phys. Rev. Lett., 2003. **91**: p. 157401.

87. Dixit, S., J. Crain, W.C.K. Poon, J.L. Finney, and A.K. Soper, *Molecular segregation observed in a concentrated alcohol -water solution.* Nature, 2002. **416**: p. 829-832.

88. Allison, S.K., J.P. Fox, R. Hargreaves, and S.P. Bates, *Clustering and microimmiscibility in alcohol-water mixtures: Evidence from molecular-dynamics simulations.* Phys. Rev. B, 2005. **71**: p. 024201.

89. Kuprowski, M.C. and L. Konermann, *Signal Response of Co-Existing Protein Conformers in Electrospray Mass Spectrometry.* Anal. Chem., 2007. **79**: p. 2499-2506.

90. Null, A.P., A.I. Nepomuceno, and D.C. Muddiman, *Implications of Hydrophobicity and Free Energy of Solvation for Characterization of Nucleic Acids by Electrospray Ionization Mass Spectrometry.* Anal. Chem., 2003. **75**: p. 1331-1339.

91. Hawlicka, E. and D. Swiatla-Wojcik, *Molecular dynamics studies of NaCl solutions in methanol-water mixtures. An effect of NaCl on hydrogen bonded network.* Chem. Phys., 1998. **232**: p. 361-369.

92. Shen, Y.R. and V. Ostroverkhov, *Sum-frequency vibrational spectroscopy on water interfaces: Polar orientation of water molecules at interfaces.* Chem. Rev., 2006. **106**: p. 1140-1154.

93. Petersen, M.K., S.S. Iyengar, T.J.F. Day, and G.A. Voth, *The hydrated proton at the water liquid/vapor interface.* J. Phys. Chem. B, 2004. **108**: p. 14804-14806.

94. Grimm, R.L. and J.L. Beauchamp, *Evaporation and Discharge Dynamics of Highly Charged Multicomponent Droplets Generated by Electrospray Ionization.* J. Phys. Chem. A, 2010. **114**: p. 1411-1419.

95. Wang, R. and R. Zenobi, *Evolution of the Solvent Polarity in an Electrospray Plume.* J. Am. Soc. Mass Spectrom., 2010. **21**: p. 378-385.

96. Zhou, S. and K.D. Cook, *Probing Solvent Fractionation in Electrospray Droplets with Laser-Induced Fluorescence of a Solvatochromic Dye.* Anal. Chem., 2000. **72**: p. 963-969.

97. Sterling, H.J., M.P. Daly, G.K. Feld, K.L. Thoren, A.F. Kintzer, B.A. Krantz, and E.R. Williams, *Effects of Supercharging Reagents on Noncovalent Complex Structure in Electrospray Ionization from Aqueous Solutions.* J. Am. Soc. Mass Spectrom., 2010. **21**: p. 1762-1774.

98. Lomeli, S.H., I.X. Peng, S. Yin, R.R. Ogorzalek Loo, and J.A. Loo, *New Reagents for Increasing ESI Multiple Charging of Proteins and Protein Complexes.* J. Am. Soc. Mass Spectrom., 2010. **21**: p. 127-131.

99. Dill, K.A. and S. Bromberg, *Molecular Driving Forces*. 2003, New York: Garland.

100. Konermann, L., *Exploring the Relationship Between Funneled Energy Landscapes and Two-State Protein Folding.* Proteins, 2006. **65**: p. 153-163.

101. Snow, C.D., Y.M. Rhee, and V.J. Pande, *Kinetic Definition of Protein Folding Transition State Ensembles and Reaction Coordinates.* Biophys. J., 2006. **91**: p. 14-24.

102. Hanggi, P., P. Talkner, and M. Borkovec, *Reaction-rate theory: fifty years after Kramers.* Rev. Mod. Pys., 1990. **62**: p. 251-342.

103. Bieri, O. and T. Kiefhaber, *Kinetic Models in Protein Folding*, in *Mechanisms of Protein Folding*, R.H. Pain, Editor. 2000, University Press: Oxford.

104. Wilm, M. and M. Mann, *Analytical Properties of the Nanoelectrospray Ion Source.* Anal. Chem., 1996. **68**: p. 1-8.

Chapter 5 – Towards a Mechanistic Understanding of Macromolecular Electrospray Ionization: A Molecular Dynamics Simulation Study

5.1 Introduction

Electrospray ionization (ESI) produces intact gaseous ions from analytes in solution, thereby making them amenable to interrogation by mass spectrometry (MS). ESI-MS can be applied to a wide range of chemical species, from low molecular weight compounds to multi-protein assemblies [1]. The formation of multiply charged ions during ESI allows the detection of high mass analytes on mass spectrometers with limited *m/z* range. Also, ESI provides the opportunity to couple liquid-phase separations with MS analyses. The combination of these attractive features makes ESI-MS a versatile and widely used technique.

During operation of a standard ESI source, analyte solution is passed through a metal capillary to which a high electric potential (usually positive vs. ground) has been applied [2]. Oxidation processes at the metal/liquid interface lead to the buildup of positive charge within the solution, giving rise to formation of a Taylor cone at the capillary outlet [3]. Micrometer-sized solvent droplets containing analyte and excess charge carriers are emitted from the tip of this Taylor cone. Rapid solvent evaporation increases the charge density on the droplets to the point where surface tension and Coulomb repulsion are balanced. The net droplet charge at this so-called Rayleigh limit is given by [4, 5]

$$z_R e = 8\pi\sqrt{\varepsilon_0 \gamma R^3} \tag{5.1}$$

where z_R is the number of elementary charges e, ε_0 is the permittivity of the vacuum, γ is the surface tension, and R is the droplet radius. Jet fission at the Rayleigh limit produces daughter droplets that carry away a small percentage of the parent droplet mass, but a disproportionately large amount of charge [2, 6-10]. In the case of mixed solvent systems, differential evaporation leads to enrichment of the component with the lowest vapor pressure, typically water [11], (Chapter 4). Successive evaporation/fission events ultimately lead to nanometer-sized droplets from which gas-phase analyte ions are produced [2].

The mechanism of the final ESI step, i.e., the formation of gaseous analyte ions from highly charged nanodroplets, remains a matter of debate [12]. According to the charged residue model (CRM), evaporation to dryness releases the analyte which retains some of the droplet's charge [2, 13]. In contrast, the ion evaporation model (IEM) stipulates that charged analytes are ejected from the droplet surface by field emission [2, 14-19]. Formation of gaseous analyte ions via the IEM leaves behind an intact solvent droplet, whereas this is not the case for the CRM. It has been suggested that large globular species such as natively folded proteins follow the CRM, whereas the IEM applies to smaller analytes [2, 16]. However, this distinction on the basis of analyte size is not universally accepted [20-22]. Strong support for the notion that the CRM is operative for folded proteins comes from the observation of protonation states that are close to z_R of correspondingly sized water droplets [23-27]. On the other hand, protein charge states and z_R do not agree as well in the negative ion mode [28]. Also, studies that tested the predicted dependence on surface tension (Equation 5.1) yielded contradicting results [11, 26]. Even if one accepts the validity of the CRM for tightly folded biopolymers, it remains unclear whether this mechanism also applies for proteins that are electrosprayed under unfolded conditions [29, 30]. Recently developed hybrid models involving elements of both the CRM and the IEM have renewed the discussion of ESI mechanism(s) [31, 32], highlighting the fact that the issues raised above are yet to be resolved.

Molecular dynamics (MD) simulations represent an interesting approach for studies on the ESI process. Insights into the mechanisms whereby small solvated ions are released from nanodroplets come from a number of computational investigations [33-39], (Chapter 3, 4). These studies support the view that small charge carriers such as Na^+ and NH_4^+ are ejected from the nanodroplet surface via thermally-activated barrier crossing (Chapter 4), consistent with predictions of the IEM [2, 14-19]. A few MD simulations were also conducted for nanodroplets containing proteins [40-42] and other polymers [43], but the implications of those studies for the mechanism of macromolecular ESI are not clear. Initial attempts from our laboratory to simulate the protein ESI process employed a minimalist approach. Solvent molecules were modeled as spheres, resulting in properties that were quite different from realistic aqueous systems [29].

Building on those previous computational investigations [29, 33-39] [40-43], (Chapter 3, 4), the current work employs MD simulations with the aim of improving the understanding of protein ESI. Solvent water and excess ions are treated using atomistic models [44], (Chapter 4). Polypeptide chains are modeled on the basis of a coarse-grained framework [45, 46] that is inspired by earlier polyampholyte studies [47, 48]. The strategy employed here aims to minimize the complexity of the overall system, while still allowing qualitative comparisons with experimental data.

From an ESI-MS practitioner's perspective, an important figure of merit is the "*ESI efficiency*" of a protein. In the context of the current work, we define this term as propensity of the protein to emerge from the charged nanodroplet as a largely desolvated gas phase ion, regardless of mechanism. Proteins with low ESI efficiencies will tend to remain heavily solvated and/or trapped within their "droplet prison" [21]. Conversely, a high ESI efficiency entails rapid and efficient desolvation, resulting in conditions that are conducive to the acquisition of high quality mass spectra.

Previous experimental studies indicate that the ESI efficiency of biomolecular analytes is governed by physicochemical properties such as (i) hydrophobicity and (ii) conformation [49-55]. The simulations of this work therefore focus on the behavior of polymer chains that exhibit different degrees of hydrophobicity, and that are either folded (compact) or unfolded (extended). It would be fascinating to use MD simulations for describing the entire ESI process, from large droplets to nanometer-sized solvent clusters, and ultimately to desolvated gas-phase macromolecular ions. Unfortunately, the system size as well as the μs-ms time range [56] of these events represent major computational challenges. This work therefore focuses on the behavior of very small nanodroplets that are poised to produce gaseous protein ions, using a short simulation time window on the order of 1 ns. Although this time frame is not quite long enough for observing the formation of fully desolvated gas-phase proteins, interesting mechanistic features can nonetheless be uncovered. Our results suggest that biopolymers that are folded and hydrophilic behave in accordance with the CRM. In contrast, species that are unfolded/hydrophobic exhibit IEM-like features. Our considerations are restricted to positively charged droplets, reflecting the prevalence of positive ion mode in most ESI-MS applications.

5.2 Methods

5.2.1 Overall MD Strategy

MD simulations were conducted in a vacuum environment with no boundary conditions, using C++ code developed in-house (Chapters 2, 3, 4). The droplet temporal evolution was modeled by integrating the classical equations of motion using the Verlet algorithm [57] with a time step of 2 fs. Each droplet contained 1000 water molecules and a model protein in either a folded or unfolded conformation, as well as excess ammonium ions. NH_4^+ was chosen because it represents a common charge carrier under ESI conditions [2]. Nanodroplets were generated from an initial cubic lattice, where individual molecules were placed in a random orientation. The protein was placed at the center of this lattice. Using constant energy MD aided by a center-symmetric external potential this lattice was then coalesced into a compact droplet of approximately spherical geometry, with the protein located close to the core. In the case of unfolded hydrophobic protein chains this strategy proved to be challenging due to the poor solvation behavior of the polymer. Additional charges were therefore placed on the backbone during the initial droplet assembly. These additional charges were removed after completion of the assembly process. Droplet coordinates obtained using this coalescing procedure were then used as initial configurations for the actual MD simulations.

The initial nanodroplets were subjected to Nose-Hoover thermalization [58, 59] at 320 K for 80 ps. The time window for the results discussed below includes this thermalization period (designated as -80 ps to t = 0). Inclusion of these data allows a common starting point to be established where the protein is located in the droplet interior, regardless of the conditions used. At t = 0 the simulations were switched to constant energy MD for roughly one nanosecond at $T \approx 320$ K. Lennard-Jones (LJ) potentials were truncated at 9.5 Å, whereas no cutoffs were used for Coulombic interactions. Mixing of LJ parameters was performed according the Lorentz-Berthlot rules [60]. Particle coordinates were extracted every 0.4 ps for analysis. Images were rendered using VMD [61].

5.2.2 Solvent Model

Water was represented on the basis of the SPC/E model with an O-H bond distance of 1.0 Å and a H-O-H angle of 109.47° [44]. The pairwise interaction between H_2O molecules is given by a combination of LJ and Coulomb potentials [36]. LJ parameters for water are $\sigma_{OO} = 3.166$ Å and $\varepsilon_{OO} = 0.6502$ kJ mol^{-1}, with charges $q_O = -0.8476\,e$ and $q_H = 0.4238\,e$. Ammonium ions were modeled with a N-H bond distance of 1.02 Å, and a H-N-H angle of 109.47°. LJ parameters for NH_4^+ are $\sigma_{NN} = 3.45$ Å and $\varepsilon_{NN} = 0.7782$ kJ mol^{-1}, with charges $q_N = -0.8172\,e$ and $q_H = 0.4543\,e$ [62]. Bond angles and bond lengths of water and ammonium were constrained using the SHAKE algorithm [63, 64].

5.2.3 Protein Model

The coarse-grained protein model used here consists of a chain of 27 beads that represent the backbone, and an additional 26 beads representing side chains (Figure 5.1). Each bead has a mass of 16 amu. The beads fall into three categories, depending on their electric charge. Side chain beads can be positively (+1 *e*) or negatively charged (-1 *e*), or they can be neutral. These three groups mimic the behavior of basic moieties in real proteins (such as Arg, Lys, N-terminus), acidic moieties (Glu, Asp, C-terminus), and nonpolar residues (including Leu, Ile, Val and others) [65]. Backbone beads in our model are neutral as well. It will be seen that positively and negatively charged beads tend to be strongly hydrated. Interactions with water are much less favorable for neutral beads, which are therefore designated as hydrophobic sites. We focus on two particular side chain patterns, both of which result in a net charge of +6 *e* (Table 5.1). The total number of charged residues is much lower for first arrangement of Table 5.1 which encompasses six positive side chains and no negatively charged sites. This will be referred to as *hydrophobic* side chain pattern. The second arrangement is designated as *hydrophilic*, reflecting the higher number of charges (13 positive and 7 negative side chains).

Under realistic conditions it is possible that proteins change their charge state during the ESI process as the result of proton transfer processes. Computational strategies involving mobile protons have been described in the literature [66, 67], (Chapter 2) but the application of these models to solute/solvent systems of the type investigated here remains challenging. In the current work we therefore make the simplifying assumption that the charges on the protein remain constant during the simulation time window.

Two types of protein conformers were investigated in this work, corresponding to the *unfolded* and the *folded* forms of the bead chain. We will first describe the features of the unfolded conformation (Figure 5.1). Covalent linkages between beads are described using a harmonic potential

$$U(r) = \frac{1}{2} k_s (r - r_0)^2 \qquad (5.2)$$

Type	**Side Chain Charge Pattern**	**Net Charge**
Hydrophobic	+ 0 0 0 + 0 0 0 0 + 0 0 0 X 0 + 0 0 0 0 0 + 0 0 0 0 +	+6
Hydrophilic	+ - + 0 + - + 0 + - + 0 + X - + 0 + - + 0 + - + 0 + -	+6

Table 5.1. Side chain charge pattern of the bead-chain protein models used in this study. Side chains carry either a positive elementary charge (+), a negative charge (-), or a zero charge (0). Backbone beads are neutral as well. X indicates the lack of a side chain at backbone bead number 14.

with k_s = 4000 kJ mol^{-1} Å^{-2}. The equilibrium bond length of r_0 = 4.0 Å roughly corresponds to the spacing between adjacent Cα atoms in a polypeptide chain [68]. Bond angles within the protein are unconstrained. Mutual interpenetration of beads was prevented by assigning LJ parameters to each bead [69], with $\sigma = 4.0$ Å and $\varepsilon = 0.6502$ kJ mol^{-1}.

The features outlined above also apply to the folded protein model (Figure 5.1), but in the latter case the backbone is arranged in a 3 × 3 × 3 cubic lattice. Side chains are attached to the 26 backbone entities that are located on the outside of this cube. The innermost backbone bead remains side-chain-free due to geometric constraints, which is why the model contains only 26 side chains for the 27 backbone beads. To prevent unfolding of the compact protein conformers during the simulations, spatially adjacent beads were linked by harmonic potentials (Equation 5.2). These additional interactions ensure a relatively rigid shape for the cubic core, with only relatively minor contortions during the simulation time window.

Nanometer-sized droplets encountered during the final stages of the ESI process are close to the Rayleigh limit [2, 23-27]. The protein/solvent droplets considered in this work have radii on the order of 2 nm. The initial excess charge of the droplets discussed

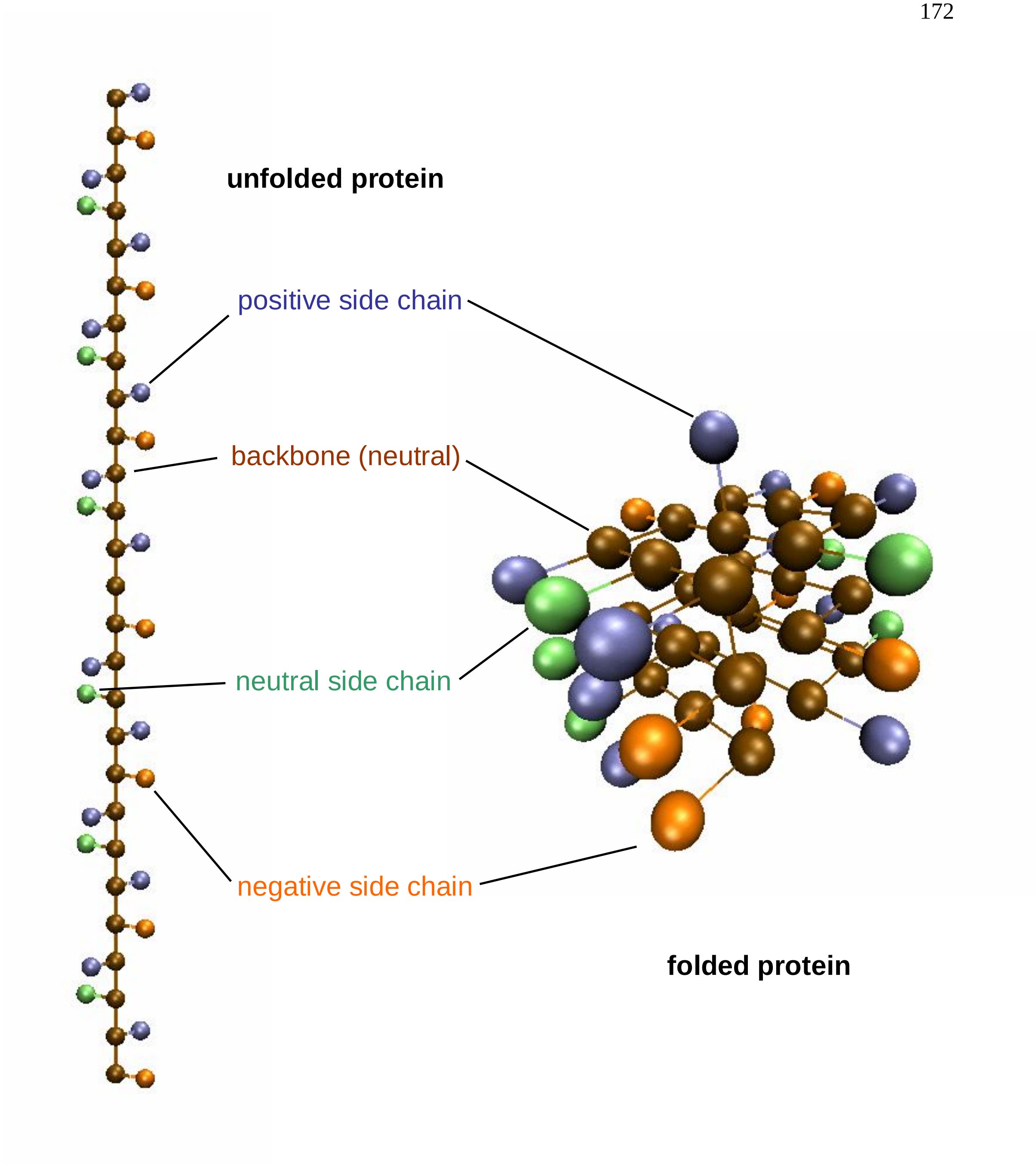

Figure 5.1. Representation of the coarse-grained protein model used for this work. Backbone and side chain elements are modeled as beads. The protein backbone can either be unfolded (shown in a fully stretched conformation), or folded. Color coding: brown, neutral backbone; green, neutral side chain; light blue, positive side chain; orange, negative side chain.

below was chosen to be +10 *e*, which corresponds to ~ 90% of z_R (Equation 5.1), (Chapter 2). These ten elementary charges are composed of + 6 *e* on the protein side chains, plus four ammonium ions.

5.2.4 Protein Mass Spectra

ESI mass spectra of myoglobin (Sigma, St. Louis, MO) were recorded at a protein concentration of 10 μM and in the presence of 50 mM ammonium acetate. The total ion current from 65 three second scans was integrated. Data for the folded protein (holo-myoglobin) were acquired at pH 7. For measurements on the unfolded protein (apo-myoglobin), the solution was acidified to pH 2 with formic acid. The data were acquired on a Q-TOF Ultima mass spectrometer (Waters, Manchester, UK) equipped with a standard Z-spray ESI source.

5.3 Results and Discussion

For modeling the protein behavior under ESI conditions, MD simulations were conducted following the procedures outlined above. Each aqueous nanodroplet initially contained one protein and four excess ammonium ions. Ejection of solvated NH_4^+ from the nanodroplets occurs at a rate of ~1.3 ns^{-1} for all the scenarios considered below. These ion ejection events are well described by the IEM, as discussed in detail elsewhere (Chapter 4). The focus of the current work is on the protein behavior. We will initially consider hydrophobic proteins, and then move on to hydrophilic systems. The side chain patterns for these two cases are depicted in Table 5.1. Folded and unfolded conformations will be studied in each case (Figure 5.1). MD movies depicting entire trajectories for the various scenarios discussed below can be found in the Supporting Information.

5.3.1 Hydrophobic Protein Behavior

A droplet containing a folded/hydrophobic protein is depicted in Figure 5.2 for two different time points. At the onset of the simulation run (*t* = -80 ps, Figure 5.2a) the protein is positioned near the center of the droplet. Structural rearrangement of the system rapidly moves the protein to the droplet surface (depicted for *t* = 284 ps in Figure 5.2b). The protein maintains this position for the remainder of the ~1 ns simulation time window. In this metastable arrangement the six positively charge side chains are oriented towards the droplet interior where they are extensively solvated. Most of the hydrophobic side chains (green) point towards the vapor phase. The droplet maintains a highly dynamic structure throughout the simulation period, with occasional ejection of hydrated

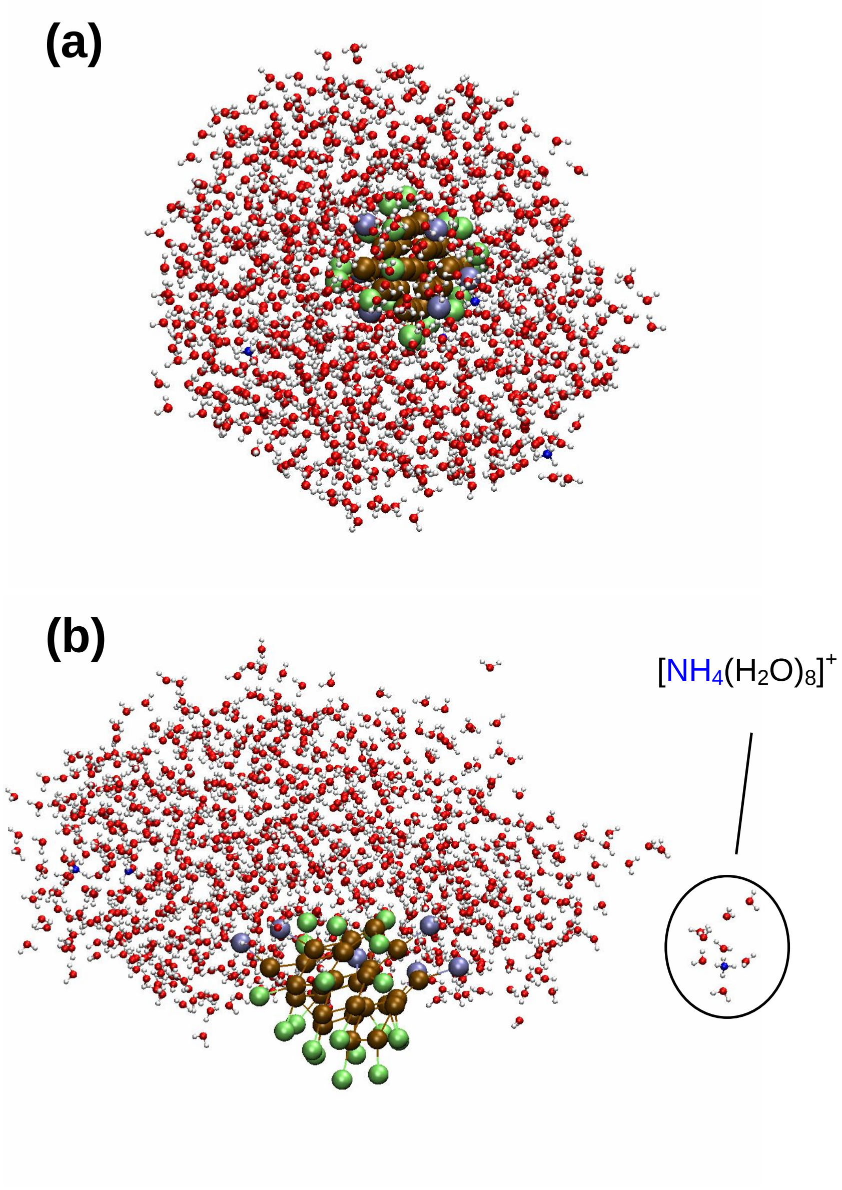

Figure 5.2. Illustrative MD simulation results for a folded/hydrophobic protein at the onset of thermalization (*t* = -80 ps, panel a), and at 284 ps (b). Color code as in Figure 5.1. In addition: white for hydrogen, red for oxygen, dark blue for nitrogen. Note the ejection of a hydrated ammonium ion in (b). The full MD movie can be found in the Supporting Information.

ammonium ions (Figure 5.2b) and evaporation of individual water molecules.

MD runs for unfolded/hydrophobic protein chains display a dramatically different behavior. At -80 ps the polymer chain is close to the droplet center (Figure 5.3a). During the thermalization period, the protein starts to uncoil, and by 0 ps it has pushed itself to the surface. Shortly thereafter, a first charged side chain starts to detach itself from the droplet, illustrated in Figure 5.3b for t = 67 ps. The other charged side chains remain hydrated by water molecules close to the droplet periphery at this time point. By 302 ps a second charged side chain is detached, while another one is on the verge of detachment (Figure 5.3c). This process continues until the entire protein chain has been expelled from the droplet, but remains connected to the surface through hydration of the last two charged side chains (t = 1147 ps, Figure 5.3d). Expelled charge sites retain solvation by small water clusters consisting of around ten H_2O molecules (Figure 5.3d). The system remains in this state for at least 2 ns, which is the longest time point explored in this study (data not shown). Recent MD simulations on the expulsion of sodiated poly-ethylene glycol from water droplets showed a very smilar behavior, with detachment of the polymer chain from the droplet after ~ 18 ns [43].

5.3.2 Hydrophilic Protein Behavior

MD simulations conducted on folded/hydrophilic proteins reveal a strong tendency of the polymer to remain buried deeply within the droplet during the entire simulation window. As an example, Figure 5.4a depicts a snapshot taken at t = 586 ps. In the case of the unfolded/hydrophilic protein the polymer chain moves somewhat closer to

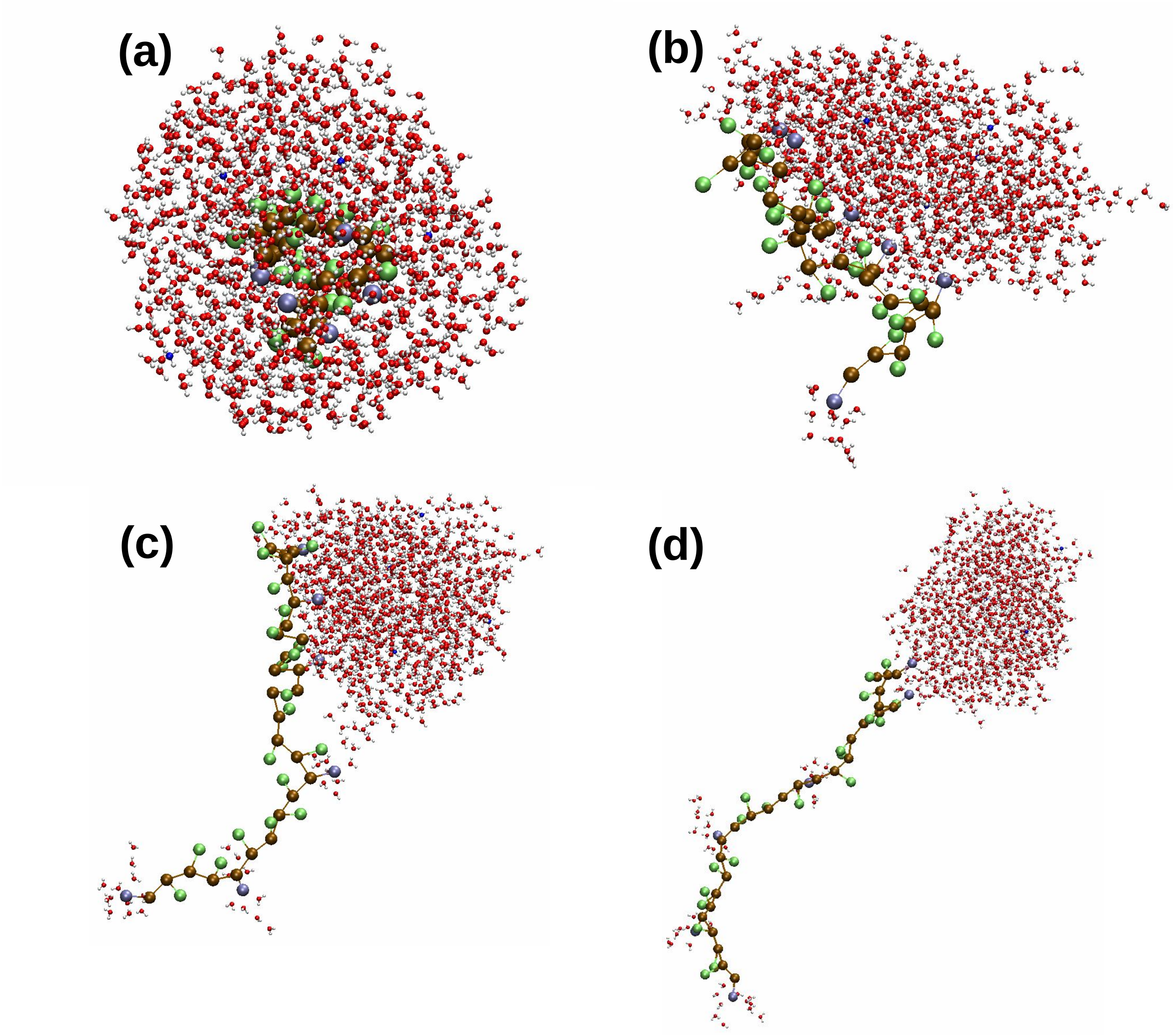

Figure 5.3. ESI process for an unfolded/hydrophobic protein at time points -80 ps (a), 67 ps (b), 302 ps (c), 1147 ps (d). Color coding is identical to Figure 5.2. The full MD movie can be found in the Supporting Information.

the droplet surface, such that several nonpolar side chains can protrude into the vapor phase while charged sites remain extensively hydrated (Figure 5.4b, *t* = 328 ps). Once again, the configurations of Figure 5.4 represent metastable scenarios that display only relatively small changes during the remainder of the simulation window. None of the hydrophilic protein chains showed any tendency to undergo expulsion from the droplet.

5.3.3 ESI Efficiency

In an attempt to quantify the desolvation propensity of the four different protein types we calculated the average center-of-mass (COM) distance between water and protein as a function of time (Figure 5.5). All four profiles obtained in this way originate at COM distances around 4 Å, representing the initial situation where the protein is enclosed by solvent within the droplet at *t* = -80 ps. Folded/hydrophilic protein chains maintain very small COM distances throughout the entire time window. Desolvation is slightly enhanced for the unfolded/hydrophilic scenario which ultimately leads to COM distances on the order of 10 Å. The desolvation propensity is markedly higher for folded/hydrophobic proteins, where the average COM distance rapidly rises to ca. 20 Å and then stays in this range. These values correspond to protein positions at the liquid/vapor interface, keeping in mind that the droplet radius is also ~ 20 Å. The most dramatic behavior is seen for unfolded/hydrophobic chains. In this case the COM distance increases to almost 50 Å within 1 ns, reflecting the prevalence of trajectories where the protein chain gets expelled from the droplet.

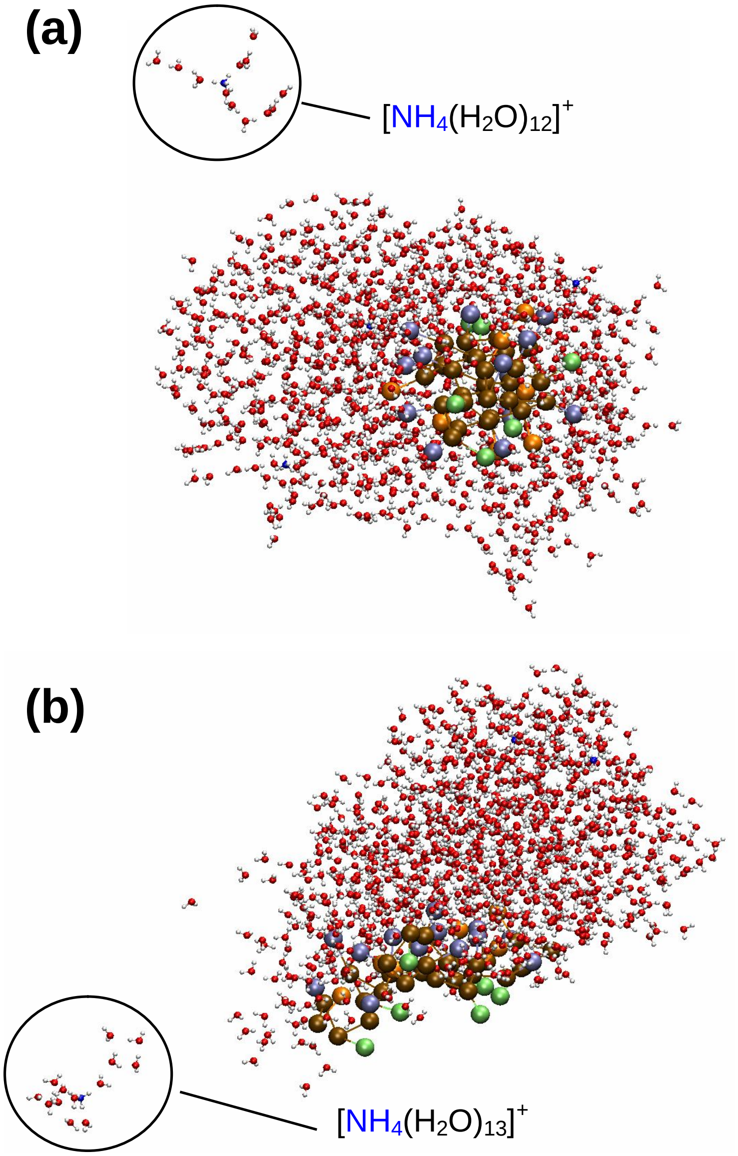

Figure 5.4. Illustrative MD simulation results for a folded/hydrophilic protein at 586 ps (a), and an unfolded/hydrophilic protein at 328 ps (b). Both panels illustrate the ejection of a hydrated ammonium ion. Color coding is identical to Figure 5.2. Full MD movies can be found in the Supporting Information.

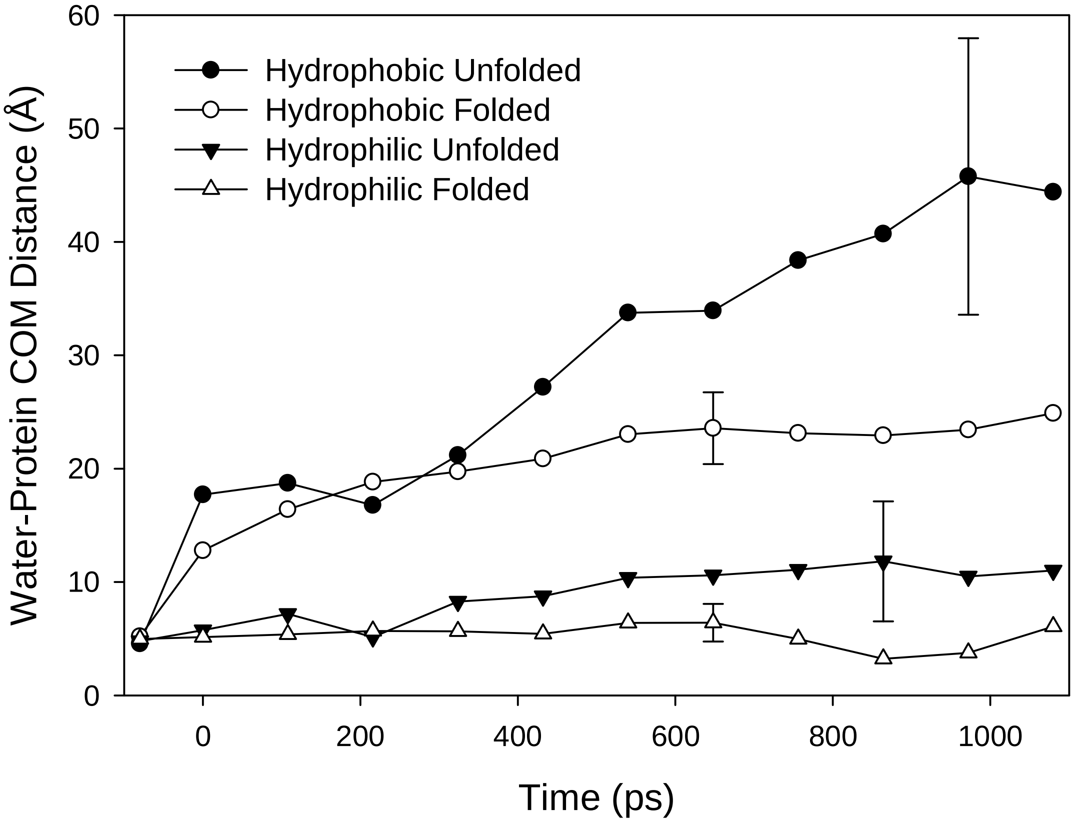

Figure 5.5. Temporal development of the average center-of-mass (COM) distance between protein and solvent. Data are shown for four different protein models as indicated in the figure. Each data point represents an average of 4 simulation runs. Error bars (standard deviations) are shown only for selected data points to prevent cluttering. The large standard deviation of the hydrophobic/unfolded scenario reflects the fact that three of the trials show protein expulsion from the droplet as depicted in Figure 5.3, whereas in one simulation run the chain remains more closely associated with the droplet surface (data not shown).

In the Introduction we defined ESI efficiency as "propensity of the protein to emerge from the charged droplet as a largely desolvated gas phase ion". The limited time window accessible in our simulations precludes the formation of completely "free" gas phase protein ions. Nonetheless, it is clear from Figure 5.5 that unfolded/hydrophobic proteins shed their surrounding droplet environment most readily, which should translate into the highest ESI efficiency. Conversely, folded/hydrophilic proteins are expected to show the lowest ESI efficiencies because they remain most heavily solvated.

The validity of these predictions was assessed in measurements on myoglobin, which represents a commonly used test protein in ESI-MS [70]. Folded myoglobin at pH 7 carries numerous polar and charged side chains on the protein surface, whereas most nonpolar residues are buried without solvent access [71]. In qualitative terms, this structure resembles the folded/hydrophilic scenario of our simulations. Unfolding at pH 2 leads to exposure of many formerly buried nonpolar residues, thereby dramatically enhancing the effective hydrophobicity of the protein [51, 70]. The hydrophobic character of the acid-unfolded protein is further enhanced by protonation of Glu and Asp residues ($\text{-COO}^- + \text{H}^+ \rightarrow \text{-COOH}$), which turns negatively charged sites into neutral moieties [29]. Myoglobin at pH 2 therefore mimics our unfolded/hydrophopic MD protein model.

ESI-MS analysis of myoglobin at pH 7 results in a fairly low signal intensity (Figure 5.6a). A striking enhancement by more than one order of magnitude in total ion count is seen upon acidification of the protein to pH 2 (Figure 5.6b). This intensity enhancement is in qualitative agreement with the predictions of our MD simulations, where unfolded/hydrophobic chains are readily expelled from the droplet, whereas

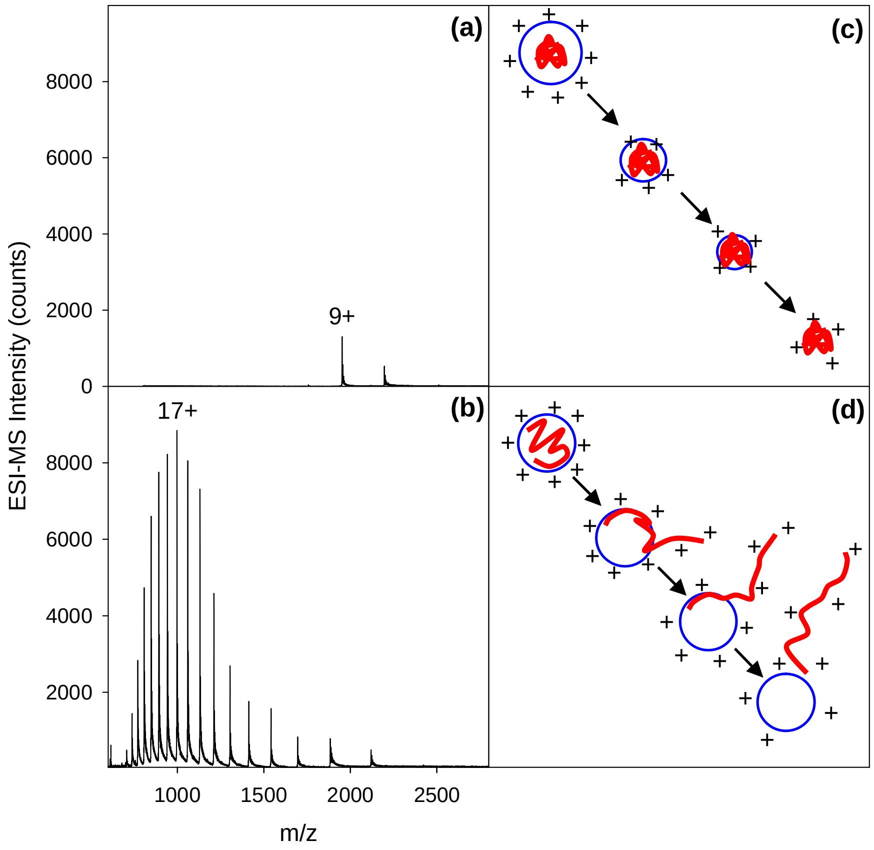

Figure 5.6. Illustration of different protein ESI mechanisms. Panels (a), (b) show ESI mass spectra of folded myoglobin recorded at pH 7 (a), and of the acid-unfolded protein at pH 2 (b). The *y*-axes in (a), (b) are scaled equally to emphasize the intensity difference of the spectra. (c) Schematic cartoon, depicting the formation of a gas-phase protein via the CRM. This mechanism is proposed to be operative for folded polypeptides with a hydrophilic exterior (such as folded myoglobin - panel a). The key factor responsible for the formation of gas-phase protein ions in (c) is slow solvent evaporation to dryness. (d) Hydrophobically-assisted IEM-like mechanism. This scenario applies to the formation of gas-phase ions in the case of unfolded/hydrophobic proteins (such as acid-unfolded myoglobin - panel b). The mechanism in (d) involves rapid ejection of the protein from the surface of an intact droplet.

desolvation of folded/hydrophilic chains is very inefficient (Figure 5.5). Additional MD simulations (not shown) were conducted to prove that the intensity enhancement seen in Figure 5.6 is not related to the different protein charge states observed at the two pH values.

5.4 Conclusions

In this MD study we explored the behavior of aqueous nanodroplets containing ammonium ions and a model protein. The presence of excess charge places these systems close to the Rayleigh limit (Equation 5.1). Possible avenues that would allow the droplets to lower their electrostatic energy include NH_4^+ emission, as well as partial or complete protein ejection. The rates of these processes are governed by an interplay of charge repulsion, solvent-solvent interactions, and solvent-solute interactions. Focusing on the two most extreme scenarios, we will briefly examine the implications of our findings for the mechanism by which gaseous protein ions are formed from ESI droplets.

The most dramatic time-dependent events are observed for unfolded/hydrophobic proteins. In this case the charged polymer chains tend to get expelled from the droplet in a stepwise sequential fashion, one charged residue at a time. This expulsion is largely driven by Coulomb repulsion between cationic side chains and excess charge carriers in the droplet. In addition, the process is facilitated by unfavorable interactions between water and hydrophobic parts of the protein (backbone and nonpolar side chains) [72]. A synergistic interplay between electrostatic forces and hydrophobicity during ion emission has previously been envisioned by others [50, 52]. Our simulations also reveal that efficient expulsion of hydrophobic proteins occurs only for unfolded conformers. In contrast, folded/hydrophobic species adopt metastable positions close to the droplet surface (Figure 5.5).

The expulsion of unfolded/hydrophobic proteins proceeds via tadpole-shaped structures that consist of a water droplet "body" and an extended polymer "tail" (Figure 5.3c, d). Thermal activation will ultimately trigger complete separation of the protein from the droplet [43], thereby giving rise to the formation of a free gas-phase protein ion. Clearly, this sequence of events (Figure 5.3) bears analogies to the IEM [2, 14-19], (Chapter 4), where ions are ejected from the surface of an intact droplet by field emission. However, a central element of many previous IEM studies is the assumption of a single free energy barrier that separates the droplet-bound ion from the free gas-phase state. In other words, the classical IEM envisions ion ejection to be a one-step event [2, 14-19], (Chapter 4). In contrast, this study as well as previous work [43] reveals that the expulsion of unfolded/hydrophobic proteins occurs in a gradual, multistep manner (Figure 5.3a-d). Overall, we conclude that gas-phase ion formation for unfolded/hydrophobic proteins is most appropriately described as a hydrophobically-assisted IEM-like process. A cartoon representation of this mechanism is depicted in Figure 5.6d. We believe that this mechanism is operative for proteins such as acid-unfolded myoglobin (Figure 5.6b).

The situation is completely different for folded/hydrophilic proteins. In this case the polymer chain remains close to the center of the droplet, where solvation of charged side chains by water is maximized. This extensive solvation makes protein ejection from the droplet surface a highly unfavorable process. Instead, release of the macromolelcular analyte into the gas phase will only be possible via the CRM, where slow solvent evaporation eventually leaves behind a dried-out protein. Shrinkage of the droplet during this drying-out process will be accompanied by ejection of charge carriers (e.g. Figure 5.4), such that the protein/solvent system remains close to the Rayleigh limit at all times [32]. Ultimately, this scenario will produce protein ions with charges close to z_R, in agreement with experimental observations [23-27]. Figure 5.6c shows a cartoon, representing the CRM steps that lead to formation of gas phase ions from folded/hydrophilic proteins (such as folded myoglobin, Figure 5.6a).

The release of folded/hydrophilic proteins into the gas phase via the CRM involves extensive solvent evaporation which is a relatively slow (~ μs [2]) process. In contrast, our simulations reveal that IEM-like ejection of unfolded/hydrophobic polymer chains from the droplet occurs several orders of magnitude faster. This increased rate of protein release translates into a much higher ESI efficiency for unfolded/hydrophobic chains, a prediction that is confirmed by the ion intensity differences in the experimental data of Figure 5.6a, b.

In future work, it will be interesting to conduct ESI simulations on larger water droplets containing more realistic protein models than those employed in the current study. It is hoped that it will also be possible to incorporate proton transfer events, with the aim of reproducing changes in protein charge state during ESI (as seen in the experimental data of Figure 5.6a, b [70]). Streamlining the source code and the use of faster processors should help extend the time range of these simulations.

5.5 References

1. Uetrecht, C., I.M. Barbu, G.K. Shoemaker, E. van Duijn, and A.J.R. Heck, *Interrogating viral capsid assembly with ion mobility–mass spectrometry.* Nat. Chem., 2011. **3**: p. 126-132.

2. Kebarle, P. and U.H. Verkerk, *Electrospray: From Ions in Solutions to Ions in the Gas Phase, What We Know Now.* Mass Spectrom. Rev., 2009. **28**: p. 898-917.

3. Van Berkel, G.J. and V. Kertesz, *Electrochemistry/spray Ion Source.* Anal. Chem., 2007. **79**: p. 5511-5520.

4. Kebarle, P. and M. Peschke, *On the Mechanisms by which the charged droplets produced by electrospray lead to gas phase ions.* Anal. Chim. Acta, 2000. **406**: p. 11-35.

5. Rayleigh, L., *On the Equilibrium of Liquid Conducting Masses charged with Electricity.* Phil. Mag., 1882. **14**: p. 184-186.

6. Gu, W., P.E. Heil, H. Choi, and K. Kim, *Comprehensive model for fine Coulomb fission of liquid droplets charged to Rayleigh limit.* Appl. Phys. Lett., 2007. **91**: p. 064104.

7. Gomez, A. and K. Tang, *Charge and fission of droplets in electrostatic sprays.* Phys. Fluids, 1994. **6**: p. 404-414.

8. Duft, D., T. Achtzehn, R. Muller, B.A. Huber, and T. Leisner, *Coulomb fission: Rayleigh jets from levitated microdroplets.* Nature, 2003. **421**: p. 128.

9. Li, D., M. Marquez, and Y. Xia, *Capturing electrified nanodroplets under Rayleigh instability by coupling electrospray with a sol–gel reaction.* Chem. Phys. Lett., 2007. **445**: p. 271-275.

10. Konermann, L., *A Simple Model for the Disintegration of Highly Charged Solvent Droplets during Electrospray Ionization.* J. Am. Soc. Mass Spectrom., 2009. **20**: p. 496-506.

11. Samalikova, M. and R. Grandori, *Protein Charge-State Distributions in Electrospray-Ionization Mass Spectrometry Do Not Appear To Be Limited by the Surface Tension of the Solvent.* J. Am. Chem. Soc., 2003. **125**: p. 13352-13353.

12. Spencer, E.A.C., T. Ly, and R.K. Julian, *Formation of the serine octamer: Ion evaporation or charge residue?* Int. J. Mass Spectrom., 2008. **270**: p. 166-172.

13. Dole, M., L.L. Mack, R.L. Hines, R.C. Mobley, L.D. Ferguson, and M.B. Alice, *Molecular beams of macroions.* J. Chem. Phys., 1968. **49**: p. 2240-2249.

14. Thomson, B.A. and J.V. Iribarne, *Field induced ion evaporation from liquid surfaces at atmospheric pressure.* J. Chem. Phys., 1979. **71**: p. 4451.

15. Iribarne, J.V. and B.A. Thomson, *On the evaporation of small ions from charged droplets.* J. Chem. Phys., 1976. **64**: p. 2287-2294.

16. Gamero-Castaño, M. and F. de la Mora, *Kinetics of small ion evaporation from the charge and mass distribution of multiply charged clusters in electrosprays.* J. Mass Spectrom., 2000. **35**: p. 790-803.

17. Tang, L. and P. Kebarle, *Dependence of ion intensity in electrospray mass spectrometry on the concentration of the analytes in the electrosprayed solution.* Anal. Chem., 1993. **65**: p. 3654-3668.

18. Labowsky, M., *A model for solvated ion emission from electrospray droplets.* Rapid Commun. Mass Spectrom., 2010. **24**: p. 3079-3091.

19. Loscertales, I.G. and J.F. de la Mora, *Experiments on the kinetics of field evaporation of small ions from droplets.* J. Chem. Phys., 1995. **103**: p. 5041-5060.

20. Fenn, J.B., *Ion Formation from Charged Droplets: Roles of Geometry, Energy, and Time.* J. Am. Soc. Mass Spectrom., 1993. **4**: p. 524-535.

21. Fenn, J.B., J. Rosell, and C.K. Meng, *In Electrospray Ionization, How Much Pull Does an Ion Need to Escape Its Droplet Prison.* J. Am. Soc. Mass Spectrom., 1997. **8**: p. 1147-1157.

22. Nguyen, S. and J.B. Fenn, *Gas-phase ions of solute species from charged droplets of solutions.* Proc. Natl. Acad. Sci. U.S.A., 2007. **104**: p. 1111-1117.

23. de la Mora, F.J., *Electrospray Ionization of large multiply charged species proceeds via Dole's charged residue mechanism.* Anal. Chim. Acta, 2000. **406**: p. 93-104.

24. Felitsyn, N., M. Peschke, and P. Kebarle, *Origin and number of charges observed on multiply-protonated native proteins produced by ESI.* Int. J. Mass Spectrom. Ion Proc., 2002. **219**: p. 39-62.

25. Nesatyy, V.J. and M.J.-F. Suter, *On the conformation-dependent neutralization theory and charging of individual proteins and their non-covalent complexes in the gas phase.* J. Mass Spectrom., 2004. **39**: p. 93-97.

26. Iavarone, A.T. and E.R. Williams, *Mechanism of Charging and Supercharging Molecules in Electrospray Ionization.* J. Am. Chem. Soc., 2003. **125**: p. 2319-2327.

27. Kaltashov, I.A. and A. Mohimen, *Estimates of Protein Surface Area in Solution by Electrospray Ionization Mass Spectrometry.* Anal. Chem., 2005. **77**: p. 5370-5379.

28. Heck, A.J.R. and R.H.H. Van den Heuvel, *Investigation of intact protein complexes by mass spectrometry.* Mass Spectrom. Rev., 2004. **23**: p. 368-389.

29. Konermann, L., *A Minimalist Model for Exploring Conformational Effects on the Electrospray Charge State Distribution of Proteins.* J. Phys. Chem. B, 2007. **111**: p. 6534-6543.

30. Testa, L., S. Brocca, and R. Grandori, *Charge-Surface Correlation in Electrospray Ionization of Folded and Unfolded Proteins.* Anal. Chem., 2011. **83**: p. 6459-6463.

31. Wang, G. and R.B. Cole, *Charged residue versus ion evaporation for formation of alkali metal halide clusters ions in ESI.* Anal. Chim. Acta, 2000. **406**: p. 53-65.

32. Hogan, C.J., J.A. Carroll, H.W. Rohrs, P. Biswas, and M.L. Gross, *Combined Charged Residue-Field Emission Model of Macromolecular Electrospray Ionization.* Anal. Chem., 2009. **81**: p. 369-377.

33. Znamenskiy, V., I. Marginean, and A. Vertes, *Solvated Ion Evaporation from Charged Water Droplets.* J. Phys. Chem. A, 2003. **107**: p. 7406-7412.

34. Marginean, I., V. Znamenskiy, and A. Vertes, *Charge Reduction in Electrosprays: Slender Nanojets as Intermediates.* J. Phys. Chem. B, 2006. **110**: p. 6397-6404.

35. Ichiki, K. and S. Consta, *Disintegration Mechanisms of Charged Aqueous Nanodroplets Studied by Simulations and Analytical Models.* J. Phys. Chem. B, 2006. **110**: p. 19168-19175.

36. Consta, S., K.R. Mainer, and W. Novak, *Fragmentation mechanisms of aqueous clusters charged with ions.* J. Chem. Phys., 2003. **119**: p. 10125-10132.

37. Caleman, C. and D. van der Spoel, *Evaporation from water clusters containing singly charged ions.* Phys. Chem. Chem. Phys., 2007. **9**: p. 5105-5111.

38. Caleman, C., J.S. Hub, P.J. van Maaren, and D. van der Spoel, *Atomistic simulation of ion solvation in water explains surface preference of halides.* Proc. Nat. Acad. Sci., 2011. **108**: p. 6838-6842.

39. Iyengar, S.S., T.J.F. Day, and G.A. Voth, *On the amphiphilic behavior of the hydrated proton: an ab initio molecular dynamics study.* Int. J. Mass Spectrom., 2005. **241**: p. 197-204.

40. Steinberg, M.Z., K. Breuker, R. Elber, and R.B. Gerber, *The dynamics of water evaporation from partially solvated cytochrome c in the gas phase.* Phys. Chem. Chem. Phys., 2007. **9**: p. 4690-4697.

41. Consta, S., *Manifestation of Rayleigh Instability in Droplets Containing Multiply Charged Macroions.* J. Phys. Chem. B, 2010. **114**: p. 5263–5268.

42. Patriksson, A., E. Marklund, and D. van der Spoel, *Protein Structures under Electrospray Conditions.* Biochemistry, 2007. **46**: p. 933-945.

43. Consta, S. and J.K. Chung, *Charge-Induced Conformational Changes of PEG-(Na+)n in Vacuum and Aqueous Nanodroplets.* J. Phys. Chem. B, 2011. **(in press)**.

44. Berendsen, H.J.C., J.R. Grigera, and T.P. Straatsma, *The missing term in effective pair potentials.* J. Phys. Chem., 1987. **91**: p. 6269-6271.

45. Bond, P.J., J. Holyoake, A. Ivetac, S. Khalid, and M.S.P. Sansom, *Coarse-grained molecular dynamics simulations of membrane proteins and peptides.* J. Struct. Biol., 2007. **157**: p. 593-605.

46. Srinivas, G., D.E. Discher, and M.L. Klein, *Self-assembly and properties of diblock coplymers by coarse-grain molecular dynamics.* Nat. Mater., 2004. **3**: p. 638-644.

47. Higgs, P.G. and J.-F. Joanny, *Theory of polyampholyte solutions.* J. Chem. Phys., 1991. **94**: p. 1543-1554.

48. Soddemann, T., H. Schiessel, and A. Blumen, *Molecular dynamics simulations of polyampholytes: Instabilities due to excess charges and external fields.* Phys. Rev. E, 1998. **57**: p. 2081-2090.

49. Null, A.P., A.I. Nepomuceno, and D.C. Muddiman, *Implications of Hydrophobicity and Free Energy of Solvation for Characterization of Nucleic Acids by Electrospray Ionization Mass Spectrometry.* Anal. Chem., 2003. **75**: p. 1331-1339.

50. Cech, N.B. and C.G. Enke, *Practical Implication of Some Recent Studies in Electrospray Ionization Fundamentals.* Mass Spectrom. Rev., 2001. **20**: p. 362-387.

51. Kuprowski, M.C. and L. Konermann, *Signal Response of Co-Existing Protein Conformers in Electrospray Mass Spectrometry.* Anal. Chem., 2007. **79**: p. 2499-2506.

52. Fenn, J.B., *Electrospray Wings for Molecular Elephants (Nobel Lecture).* Angew. Chem. Int. Ed., 2003. **42**: p. 3871-3894.

53. Chalcraft, K.R., R. Lee, M. C., and P. Britz-McKibbin, *Virtual Quantification of Metabolites by Capillary Electrophoresis-Electrospray Ionization-Mass Spectrometry: Predicting Ionization Efficiency Without Chemical Standards.* Anal. Chem., 2009. **81**: p. 2506-2515.

54. Oss, M., A. Kruve, K. Herodes, and I. Leito, *Electrospray Ionization Efficiency Scale of Organic Compounds.* Anal. Chem., 2010. **82**: p. 2865-2872.

55. Walker, S.H., L.M. Lilley, M.F. Enamorado, D.L. Comins, and D.C. Muddiman, *Hydrophobic Derivatization of N-linked Glycans for Increased Ion Abundance in Electrospray Ionization Mass Spectrometry.* J. Am. Soc. Mass Spectrom., 2011. **22**: p. 1309-1317.

56. Kebarle, P. and L. Tang, *From ions in solution to ions in the gas phase: The mechanism of electrospray mass spectrometry.* Anal. Chem., 1993. **65**: p. 972A-986A.

57. Verlet, L., *Computer "Experiments" on Classical Fluids. I. Thermodynamical Properties of Lennard-Jones Molecules.* Phys. Rev., 1967. **159**: p. 98-103.

58. Nose, S., *A molecular dynamics method for simulations in the canonical ensemble.* Mol. Phys., 1984. **52**: p. 255-268.

59. Hoover, W.G., *Canonical dynamics: Equilibrium phase-space distributions.* Phys. Rev. A, 1985. **31**: p. 1695-1697.

60. Delhommelle, J. and P. Millie, *Inadequacy of the Lorentz-Berthelot combining rules for accurate predictions of equilibrium properties by molecular simulation.* Mol. Phys., 2001. **99**: p. 619-625.

61. Humphrey, W., A. Dalke, and K. Schulten, *VMD - Visual Molecular Dynamics.* J. Mol. Graphics, 1996. **14**: p. 33-38.

62. Chang, T.-M. and L.X. Dang, *On rotational dynamics of an NH4+ ion in water.* J. Chem. Phys., 2003. **118**: p. 8813-8820.

63. Allen, M.P. and D.J. Tildesley, *Computer Simulation of Liquids*. 1987: Clarendon Press.

64. Forester, T.R. and W. Smith, *SHAKE, Rattle and Roll: Efficient Constraint Algorithms for Linked Rigid Bodies.* J. Comput. Chem., 1998. **19**: p. 102-111.

65. Kyte, J. and R. Doolittle, *A simple method for displaying the hydropathic character of a protein.* J. Mol. Biol., 1982. **157**: p. 105-132.

66. Wang, F., S. Izvekov, and G.A. Voth, *Unusual "amphiphilic" association of hydrated protons in strong acid solution.* J. Am. Chem. Soc., 2008. **130**: p. 3120-3126.

67. Jungwirth, P. and D.J. Tobias, *Specfic ion effects at the air/water interface.* Chem. Rev., 2006. **106**: p. 1259-1281.

68. Creighton, T.E., *Proteins*. 1993, New York: W. H. Freeman & Co.

69. Charlaganov, M. and F.A.M. Leermakers, *Molecular modeling of intermolecular and intramolecular excluded volume interactions for polymers at interfaces.* J. Chem. Phys., 2009. **131**: p. 244115.

70. Dobo, A. and I.A. Kaltashov, *Detection of Multiple Protein Conformational Ensembles in Solution via Deconvolution of Charge-State Distributions in ESI MS.* Anal. Chem., 2001. **73**: p. 4763-4773.

71. Evans, S.V. and G.D. Brayer, *High-resolution Study of the Three-dimensional Structure of Horse Heart Metmyoglobin.* J. Mol. Biol., 1990. **213**: p. 885-897.

72. Chandler, D., *Oil in troubled waters.* Nature, 2007. **445**: p. 831-832.

Chapter 6 – Conclusions

6.1 Summary

In this work we have outlined the use of MD simulations as a complementary method to theory and experimentation, for investigating the physical behaviour of charged nanodroplets phenomena. As was shown, such an approach can be very useful in situations where experiments work pose limits and challenges. The findings presented herein are relevant for the ESI mechanism.

In the first project (Chapter 2), a proton model was developed via a heuristic approach by matching the diffusion coefficient with the experimental value. The model developed does not produce the Grotthus mechanism [1-4] for proton transfer, however, it provides a reasonable framework that might be used for exploring processes involving protonation and deprotonation events. The protons ability to diffuse easily through a cluster of waters was the main driving force for its development. The radial distribution of the protons raised interesting questions as to where the charge carriers reside in a droplet.

Conventional electrostatic theory [5, 6] predicts that charges on a spherical conductor should sit at the surface. Yet in our first project, we noted that the mobile protons were at a distance in between the surface and the interior of the water droplet. This question was further investigated in Chapter 3 where we used sodium ions and equivalent anions to model the problem. Initially we assumed the aberration in the radial distribution for the protons could have been caused by the model we developed. By performing simulations with sodium ions and anions, however, we obtained similar radial distributions. With a simple potential mapping method, we were able to show that even though ions remained solvated within the droplet (similar to our proton findings), the charge had been projected onto the surface via dipole orientation of the waters. This was quite revealing and at the same time reassuring.

In Chapter 4, we investigated the efficiencies of ion ejection from methanol/water mixtures [7, 8]. Several interesting points can be made from this study. The presence of the methyl group greatly reduced the hydrogen bonding network of the methanol and made it more susceptible to higher evaporation rates. As a result of this, a microsegregation of methanol molecules occurred at the periphery of the droplet. The water molecules on the other hand were well isolated in the interior of the droplet due to more extensive hydrogen bonding than in methanol. Ammonium ion ejection and solvent evaporation were enhanced as a result of this different hydrogen bonding behavior.

The final project (Chapter 5) deals with investigating the ESI mechanism using a much larger macromolecular ion than in the previous Chapters 2, 3, 4. The ionic species used is a model protein in two distinct conformations, folded and unfolded. We also incorporated ammonium ions to move the system closer to the Rayleigh limit. Results indicated that hydrophobic conformations of the protein prefer the interface region more than the interior regions of the droplet. The folded and unfolded conformations behave very differently from one another. The compact folded hydrophobic and hydrophilic folded/unfolded conformations of the protein prefer ammonium ion ejection to reduce the charge density of the droplet. In contrast, the hydrophobic unfolded protein prefers expulsion of the polymer chain from the droplet surface as opposed to ammonium ion ejection. Although a fully detached unfolded protein ion was not observed due to the relatively short simulation time (~ 1 ns) this behaviour clearly reveals IEM-like characteristics, serving as a springboard for future investigations into the ESI mechanism of large analytes.

6.2 Future Directions

6.2.1 Continuation of Current Model Protein Simulations

One possible future study would be to continue the current model protein simulations until a full detachment of the unfolded hydrophobic protein occurs, possibly on the order of tens of nanoseconds or more. It would be interesting to see the full detachment of the protein from the water droplet thereby validating the IEM model. As for the hydrophilic versions of the protein, it would be interesting to see how many cycles of evaporation and Coulombic fission (assuming ammonium ions) would be required for the model protein to remain as a charged residue consistent with the CRM mechanism. Simulations at higher temperatures would possibly speed up evaporation and Coulombic fission but a full test of the water and ion models at elevated temperatures would need to be conducted first.

6.2.2 Shorter Model Proteins Modeling Peptides

Another possible future project would be to use a much shorter polymer chain, possibly 10 – 15 beads representing a peptide. It would be interesting to see if these smaller analytes behave similar to the unfolded model protein discussed in Chapter 5. In particular it would be worth exploring whether these peptides would compete with small ions such as NH_4^+ for Coulombic ejection.

6.2.3 Alternate Modeling of Proteins

Another possible project would be to develop a more realistic model for a protein using an all-atom approach. Although an all-atom investigation will be much more time consuming than a coarse grain approach [9], certain interactions might be better captured. Yet, another technique would be to use Monte Carlo simulation of the model protein developed in Chapter 5 and compare the trajectories with those of the MD method. The MC [10] method might provide better sampling of conformational space but would lack time correlation. It could serve as a good method of generating starting configurations of the protein for subsequent MD simulations.

6.2.4 Modeling Droplets with Inert Gas Bombardment

Another possible project would be to model an inert gas such as Argon to bombard a highly charged droplet, thereby mimicking the conditions in the interface of an ESI mass spectrometer. This method could be used to perform two things, an alternative heating mechanism that is immune to evaporative cooling, and also provide projectiles to “knock off” waters from the protein until complete dryness.

6.2.5 Polarizable Water Models

Another possible project would be to replace the SPC/E with a polarizable model and compare the effects of the interaction with the protein and solvated ions. The use of either the use of a Drude oscillator model [11], or fluctuating charges [12], or inducible dipoles [13] might be challenging but very insightful.

6.3 References

1. Marx, D., *Proton transfer 200 years after von Grotthuss: Insights from Ab initio simulations.* ChemPhysChem., 2006. **7**: p. 1848-1870.

2. Zweir, T.S., *The structure of protonated water clusters.* Science, 2004. **304**: p. 1119-1120.

3. Cukierman, S., *Et tu, Grotthuss! and other unfinished stories.* Biochimica et Biophysica Acta, 2006. **1757**: p. 876-885.

4. Swanson, J.M.J., C.M. Maupin, H. Chen, M.K. Petersen, J. Xu, Y. Wu, and G.A. Voth, *Proton solvation and transport in aqueous and biomolecular systems: Insights from computer simulations.* J. Phys. Chem. B, 2007. **111**: p. 4300-4314.

5. Halliday, D., R. Resnick, and K.S. Krane, *Physics.* 4 ed. 1992, New York: Wiley.

6. Rayleigh, L., *On the Equilibrium of Liquid Conducting Masses charged with Electricity.* Phil. Mag., 1882. **14**: p. 184-186.

7. Cech, N.B. and C.G. Enke, *Practical Implication of Some Recent Studies in Electrospray Ionization Fundamentals.* Mass Spectrom. Rev., 2001. **20**: p. 362-387.

8. Kebarle, P. and U.H. Verkerk, *Electrospray: From Ions in Solutions to Ions in the Gas Phase, What We Know Now.* Mass Spectrom. Rev., 2009. **28**: p. 898-917.

9. Han, W., C.-K. Wan, and Y.-D. Wu, *Toward a coarse-grained protein model coupled with a coarse-grained solvent model: Solvation free energies of amino acid side chains.* J. Chem. Theory Comput., 2008. **4**: p. 1891-1901.

10. Hogan, C.J. and P. Biswas, *Monte Carlo Simulation of Macromolecular Ionization by Nanoelectrospray.* J. Am. Soc. Mass Spectrom., 2008. **19**: p. 1098-1107.

11. Lamoureux, G., A.D. MacKerell, and B. Roux, *A simple polarizable model of water based on classical Drude oscillators.* J. Chem. Phys., 2003. **119**: p. 5185-5197.

12. Rick, S.W., S.J. Stuart, and B.J. Berne, *Dynamical fluctuating charge force fields: Application to liquid water.* J. Chem. Phys., 1994. **101**: p. 6141-6156.

13. Chialvo, A.A. and P.T. Cummings, *Engineering a simple polarizable model for the molecular simulation of water applicable over wide ranges of state conditions.* J. Chem. Phys., 1996. **105**: p. 8274-8281.

Elias Ahadi
Department of Chemistry
The University of Western Ontario (UWO)
London, Ontario, N6A 5B7, Canada

EDUCATION:

The University of Western Ontario – London, ON, Canada
Ph.d., Chemistry – September 2011

New Jersey Institute of Technology – Newark, NJ, USA
M.Sc., Materials Science and Engineering – January 2002

Montclair State University – Upper Montclair, NJ, USA
B.Sc., Physics, *cum laude* – August 1999
B.Sc., Chemistry, *cum laude* – May 1998

Honors/Awards/Scholarships from Montclair State University

– Dean's List: Fall (1995, 1996, 1997), Spring (1995, 1997, 1998, 1999), Summer 1999.
– First Year Chemistry Award, 1995.
– Outstanding Student Worker Award, 1997.
– Meritorious Honor in the 1999 Mathematical Contest in Modeling, Sigma Xi Research Certificate, 1999.
– Outstanding Baccalaureate Award in Physics, 1999.
– Edward J. Bloustein Scholarship, Fall 1994 – May 1998.

Awards/Scholarships from The University of Western Ontario

– Western Graduate Research Scholarship (WGRS): Fall (2005, 2008), Winter 2006, Summer (2007, 2008).
– Nominated for Graduate Student Teaching Award in Chemistry 2006-2007.

WORK EXPERIENCE:

September 2005 – August 2009
The University of Western Ontario, Department of Chemistry
Teaching Assistant

- Taught tutorial and laboratory sections for Chem 024a (Fall 2005, 2006), Chem 020a (Fall 2007), Chem 1050a (Fall 2008), Chem 300g (Winter 2006, 2007, 2008, 2009).

April 2004 – August 2004
Wyeth Pharmaceuticals Inc., Bulk Vaccine Manufacturing
Scientific Technical Writer

- Responsible for keeping accurate track of changes made to batch records used for the production of $AlPO_4$ and Prevnar$^{®}$ vaccine.

February 2003 – June 2004
Patent Complete, LLC.
Patent Searcher

- Conduct novelty, validity, infringement and state-of-art patent searches in the fields of chemistry, physics and materials engineering for clients using the USPTO and foreign patent databases.

January 2000 – January 2002	**New Jersey Institute of Technology, Department of Physics** **Teaching Assistant**

- Taught laboratory sections for Phys 121A (Fall 2000), Phys 105A and Phys 103A, (Spring 2000), Phys 111A (Fall 2001), Phys 231A (Fall and Spring 2001)
- Developed and maintained website for the Physics Department.

PUBLICATIONS:

E. Ahadi and L. Konermann, *A 'Hopping' Proton Model for Molecular Dynamics Simulations of Charged Water Nanodroplet*, J. Phys. Chem. B (2009), 113, 7071-7080.

E. Ahadi and L. Konermann, *Surface Charge of Electrosprayed Water Nanodroplets: A Molecular Dynamics Study*, J. Am. Chem. Soc., (2010), 132, 11270-11277.

E. Ahadi and L. Konermann, *Ejection of Solvated Ions from Electrosprayed Methanol/Water Nanodroplets Studied by Molecular Dynamics Simulations*, J. Am. Chem. Soc., (2011), 133, 9354-9363.

CONFERENCE PROCEEDINGS:

Elias Ahadi and Lars Konermann, **A 'Hopping' Proton Model for Molecular Dynamics Simulations of Highly Charged Water Nanodroplet,** 4th One Day Workshop, Western Institute for Nanomaterials Science (WINS), The University of Western Ontario, London, ON, Canada, May 16, 2008.

Elias Ahadi and Lars Konermann, **A 'Hopping' Proton Model for Molecular Dynamics Simulations of Highly Charged Water Nanodroplet**, 56th meeting of the American Society of Mass Spectrometry (ASMS), Denver, CO, USA, June 1 – 5, 2008.

Elias Ahadi and Lars Konermann, **Proton Distribution in ESI Nanodroplets: Is the "Surface Charge" Really Tenable?** 57th meeting of the American Society of Mass Spectrometry (ASMS), Philadelphia, PA, USA, May 31 – June 5, 2009.

Elias Ahadi and Lars Konermann, **Surface Charge of Electrosprayed Water Nanodroplets: A Molecular Dynamics Study,** 58th meeting of the American Society of Mass Spectrometry (ASMS), Salt Lake City, UT, USA, May 23 – 27, 2010.

Elias Ahadi and Lars Konermann, **Mechanism of Protein Electrospray Ionization Explored by Molecular Dynamics Simulations,** 59th meeting of the American Society of Mass Spectrometry (ASMS), Denver, CO, USA, June 5 – 10, 2011.